Aciniform Spider Silk Proteins: Investigating Solution-State Assembly and the Potential of Silk Nanoparticles as a Drug Delivery Vehicle

by

Stefan A. Warkentin

Submitted in partial fulfilment of the requirements
for the degree of Master of Science

at

Dalhousie University
Halifax, Nova Scotia
December 2019

Dedications

Dedicated to my mother, father, grandmother, and sisters

Table of Contents

List of Tables

List of Figures

Abstract

Spider and silkworm silks form a wide variety of biomaterials with desirable mechanical properties and biocompatibility. The process of fibrillogenesis from silk solution is not fully understood, but may be dependent on micellar assemblies formed in the gland. In this study the micelle formation and surface adsorption of a recombinant aciniform repeat unit (W_1) were investigated, as this may give clues to the fibrillogenic pathway. It was found that micelle-like assemblies formed by W_1 are very low in yield, however the protein self-assembles at the liquid-air interface. Aciniform proteins with multiple repeats showed visco-elastic properties at the surface layer while W_1 did not. The alignment and conformational changes of aciniform proteins at the liquid-air interface may be relatable to those which occur during fibrillogenesis. Disruption to helix 5 of the W_1 protein may be involved in early conformational transitions during the process of fibrillogenesis. The R36W residue of a W_1 variant, which is on the protein surface beneath helix-5, was found to make the variant less stable than the wild-type. This may be due to disruption to helix 5 caused by the substitution, which may expose a hydrophobic surface that encourages interprotein interactions. Silkworm and dragline spider silk are well established as potential drug delivery vehicles, however aciniform silks have not yet been investigated for that purpose. Nanoparticles of W_1 were formed by a desolvation process and characterised in terms of size and conformation, yielding a novel biomaterial for aciniform silk. Aciniform nanoparticles may have different drug-compatibilities and desirable uptake and release properties compared to other silk nanoparticles, though this remains to be investigated.

List of Abbreviations Used

1,8-ANS: 1-anilinonaphthalene-8-sulfonic acid

aa: amino acid

Ac: aciniform

AcSp1: aciniform spidroin 1

ADF: *Araneus diadematus* fibroin

ASG: aggregate spider glue

***A. trifasciata*:** *Agriope trifasciata*

AU: arbitrary units

CD: circular dichroism

CMC: critical micellar concentration

DLS: dynamic light scattering

DPC: dodecylphosphocholine

DTXL-TNP: docetaxel-targeted polymeric nanoparticle

eADF4(C16): engineered *Araneus diadematus* fibroin

***E. coli*:** *Escherichia coli*

EMiM[acetate]: 1-ethyl-3-methyl-imidazolium acetate

EPR: nhance permeability and retention effect

Eq.: equation

Flag: flagelliform

FRET: Förster resonance energy transfer

HSQC: heteronuclear single quantum coherence

kDa: kilodalton

LB: lysogeny broth

Ma: major ampullate

MaSp1: major ampullate spidroin 1

MaSp2: major ampullate spidroin 2

Mi: minor ampullate

NMR: nuclear magnetic resonance

NNLS: non-negative least squares

NOE: nuclear overhauser effect

PEG: poly-ethylene glycol

PPII: poly-proline II

PSMA: prostate-specific membrane antigen

PVA: poly-vinyl alcohol

SEM: scanning electron microscopy

Sp: spidroin

TFA: trifluoroacetic acid

TFE: trifluoroethanol

T_m: melting temperature

VEGF: vascular endothelial growth factor

wt: wild-type

Acknowledgements

Dr. Jan K. Rainey

for his support, advice and guidance as my supervisor

Dr. Steve Bearne and Dr. Roy Duncan

for their advice as supervisory and examining committee members

Dr. Christian Blouin

for his advice as an examining committee member

Dr. Lingling Xu

for training and providing essential plasmids for this work

Rainey Lab Members

for their support and advice

NSERC and The Department of Biochemistry & Molecular Biology

for funding this research

The Scientific Imaging Suite (Dalhousie)

for use of SEM equipment

The Clean Technologies Research Institute (Dalhousie)

for use of SEM-FIB Facility

Chapter 1: Introduction

1.1 Silk Protein Structures

1.1.1 Types of Silk Proteins

A variety of animals produce silks, including spiders, worms, flies, wasps and crickets [1]. These protein-based materials are typically used by the organism for protective or prey-capture applications, with longstanding human use of silkworm silks for textiles. Of these various types of silk, silkworm and spider silks are the best studied and will be discussed here. Silkworm fibroins are the primary proteins that make up the silk fibres used to form cocoons, and consist of two proteins linked by a disulphide bond: a long heavy chain and a much shorter light chain [2]. A glycoprotein P25 is also associated non-covalently with the fibroins [3]. In the cocoon setting, silkworm fibroins are well coated with a small protein sericin, which can improve the chemical properties of the silk cocoon [4].

In contrast to the single type of silk produced by silkworms, spiders can produce up to 7 different types of silk proteins (spidroins), dependent on species [5]. Each of these silks is formed in and spun from a specialized gland (Figure 1) [6]. These silks possess different mechanical properties and structures, allowing them to serve different biological functions [5].

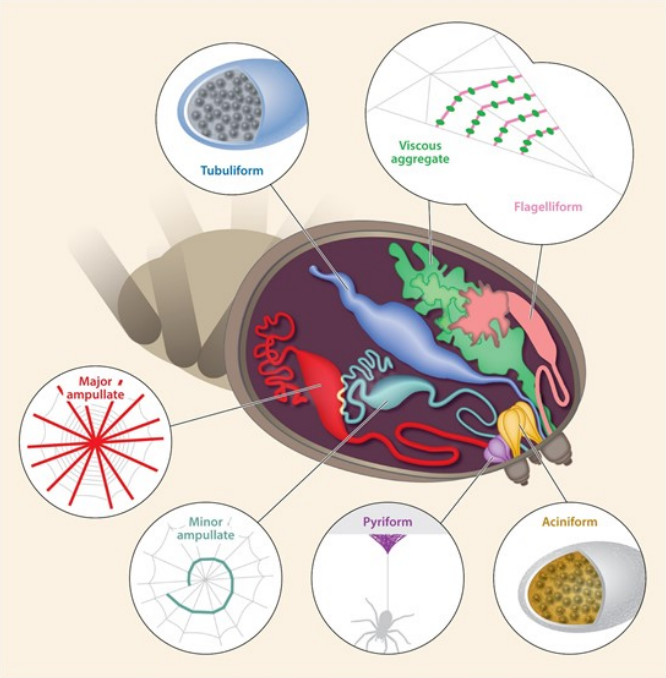

Figure 1: Anatomy of spider silk glands producing 7 different types of silk proteins. Reproduced from Blamires et al. [6]

Most gene sequence information pertaining to silk proteins comes from analysis of several species of orb-weaving spiders. With tens of thousands of species of spiders [7], this does not account for inter-species variation. Major ampullate (Ma) silk – termed dragline silk – is employed as the outer frame and radial strands of the spider's web, and as the lifeline for the spider [5]. Ma silk fibres are composed of two proteins: MaSp1 [8] and MaSp2 [9] in *Nephila clavipes* or ADF-3 and ADF-4 in *Araneus diadematus* [10]. Pyriform (Py) silk forms attachments between the web frame, composed of Ma silk, and different surfaces as a glue-like substance [5]. This silk forms an attachment disc consisting of small fibres in a highly branched, mesh-like structure to which a dragline fibre is attached [11]. Py silk contains two proteins: PySp1 [11] and PySp2 [12]. Minor ampullate (Mi) silk is employed as the auxiliary spiral, providing structural support for the web [5]. Flagelliform (Flag) silk is used in the web to form the capture spiral onto which aggregate silk is deposited to form an adhesive coating [5]. Two aggregate spidroins have been identified: ASG1 and ASG2 (aggregate spider glue) [13]. Outside of the web, aciniform spidroin 1 (AcSp1) is used for prey wrapping and in lining the egg case [14] , while cylinidriform (Cy)/tubiliform (Tu) silk is used to form the egg case [15, 16].

1.1.2 Primary Structure

Silk proteins are large proteins, typically of several hundred kDa, consisting of many repetitive sequence motifs linked end-to-end, which at several thousand amino acids (aa), comprise the majority of the protein. The repetitive sequences are flanked by shorter non-repetitive N and C terminal domains of 50 to 200 AA. The sequence motifs of the repetitive region are typically held to be responsible for the mechanical properties of the fibre or other biomaterial formed by a particular silk protein, as described below and summarised in Table 1.

Table 1: Sequence motifs present in the repetitive regions of various silk proteins

	Repetitive Motifs
Silkworm Fibroin	GX, GAGAGA, GAGAGY, GAGAGS, GAGYGA, GAAS
MaSp1	GGX, A_n
MaSp2	GGX, GPX, QQ, A_n
Mi	GX, GGX, GGGX, A_n
Flag	GGX, GPGGX
Cy	GX, A_n, S_n, $(SA)_n$, $(SQ)_n$
PySp1	AAARAQAQAE and AAARAWAWAEARAKAE or QQXXXX, proline rich
PySp2	long and complex, proline rich
Ag	long and complex
AcSp1	long and complex

The repetitive sequence of the silkworm fibroin heavy chain (391 kDa) consists primarily of glycine based motifs (GX) in which X may be any amino acid, but with X mainly being alanine, tyrosine and valine. These GX motifs also form several hexapeptide motifs, with GAGAGS and GAGAGY being the most common, alongside small numbers of GAGAGA and GAGYGA as well as GAAS motifs. 12 repetitive sequences of up to ~600-aa are separated by a 43-aa well-conserved and non-repetitive spacer [2]. The non-repetitive N-terminal domain (151-aa) contains a secretion signal [17], while the non-repetitive C-terminal domain (58-aa) contains the cysteine responsible for disulphide linkage to the light chain [18]. The light chain contains no repetitive elements, and is less enriched in glycine and alanine than the heavy chain, with asparagine being most common at 14.8% [19].

The N-terminal domains (~180-aa) of ampullate, flagelliform and cylindriform silks are conserved [20] and consist of an initial secretion signal and a 5 α-helix bundle [21]. A conserved TTGXXN motif of unknown function is found in a number of N-terminal domains between helices 4 and 5 [22]. The non-repetitive C-terminal domains (~100-aa) are likewise well conserved [20], with those of MaSp1 and MaSp2 showing mixed α-helix/β-sheet structure [23], and that of cylindriform forming a 5 α-helix bundle [21].

Both major and minor ampullate silks are dominated by glycine and poly-alanine based repeats. The MaSp1 repeat domain consists of poly-alanine and GGX motifs, in which X is tyrosine, alanine or glutamine. Four very similar repeat types are present which differ in the number and pattern of the GGX motifs, all ending in poly-alanine. MaSp2 proteins have much more complex repeats containing GGX (with X being alanine or sometimes glutamate), GPX (X:

mostly glycine and serine), and QQ motifs. Four types of repeats combine either all or some of these motifs. Typically, a single QQ is flanked by GPX with a GGX at the start and poly-alanine at the end [24]. Silk from *Argiope bruennichi* also contains GGF and SGR motifs [25]. MiSp silks consist of 3 repetitive regions separated by two non-repetitive spacers. Repetitive motifs are short alternating stretches of GX, GGX, GGGX and poly-alanine, with X being predominantly alanine and tyrosine [26].

Flagelliform silks also contain glycine-rich motifs, but lack the poly-alanine motifs of the ampullate silks [27]. Each repeat consists of many GPGGX motifs followed by a smaller number of GGX motifs and a spacer, where X is predominantly serine or tyrosine [27]. Cylindriform silk also consists of several short motifs (Table 1), although these are different in nature than the glycine-based motifs of ampullate and flagelliform silks. The motifs found in cylindriform spidroin are A_n, S_n, $(SA)_n$, $(SQ)_n$ and GX, where *n* is less than 3 and most commonly 1. These repeats are high in serine and threonine [15, 16]. Pyriform repeats are very low in glycine compared to the other spidroins, with longer, more complex repeats that are higher in alanine, but not poly-alanine [11]. For PySp1 from *Latrodectus hesperus,* the repetitive region consists of two alternating motifs: AAARAWAWAEARAKAE and AAARAQAQAE. Three stretches of these alternating motifs are separated by 3 conserved hydrophilic spacers of 78 amino acids. The N-terminal domain is short, at only 8 amino acids, and the C-terminal domain is much longer and contains a number of AAA sequences as seen in the repetitive region [11]. In contrast, PySp2 contains less than half the amount of alanine of PySp1, instead containing much more serine and threonine [12]. The PySp2 repetitive region consists of alternating long motifs of 190 and 40 amino acids. In the shorter motif, nearly every other residue is proline [12]. The complete PySp1 gene from *Argiope argentata* has been sequenced, showing 21 repeats of 234 amino acids connected by linkers to the non-repetitive N and C terminals [28]. The N-terminal linker contains repeats of XSXXQQQYEAXQQQ, and the C-terminal linker SSS repeats. The repeat units contain QQXXXX and a high proline content in the last 50 amino acids [28]. Several glutamine and proline residues are well conserved across species for PySp1 [28]. Compared to other spider silks, pyriform silk is much more hydrophilic and proline-rich [11, 12].

Aciniform and aggregate silk differ from other spider silks in that they are composed of long repeats lacking in repetition of short internal motifs. AcSp1 repeats are the longest, with 14 copies of 200-aa for *Agriope trifasciata*, separated by short non-repetitive linkers and non-

repetitive N and C terminals [14]. Aggregate repeats of 89-99 amino acids are repeated at least three times, with predicted β-sheet, β-turn and random coil conformation. A long non-repetitive linker separates the repetitive region from a non-repetitive C-terminal domain with predicted α-helical structure. The N-terminal domain is not yet characterised [13].

1.1.3 Secondary and Tertiary Structure

The relative content of each type of structuring affects the mechanical properties of the silk material and is ultimately dependent on the amino acid sequence of the repetitive region. Overall, well aligned β-sheets confer strength and rigidity to silk materials, while amorphous and α-helical regions confer extensibility and toughness. Strength refers to the force required to break a fibre, while extensibility is the distance relative to the original length that a fibre may be pulled. Toughness is the energy which can be absorbed, and results from the relative amounts of strength and extensibility [29].

Silkworm fibroin in a crystalline state can exist as two different forms, termed Silk I and Silk II. Silk I is formed by spinning dope that has been gently dried without mechanical shear forces required for fibre formation, and is primarily random coil [30]. Silk I can be seen as being between the soluble and fibrous conformations and so may give information about the transition of silk from soluble protein to insoluble fibre [30]. Solid state NMR of silkworm fibroin indicates that Silk I adopts type II β-turn structures which may be the progenitors of β-sheet segments, with intra- and inter-molecular hydrogen bonds [31]. Silk II is the conformational state of the silk fibre and other materials such as films and is a state that is high in β-sheet with some amount of random coil. Silk II structures are generally composed of parallel and overlapping crystalline β-sheets, alternating with amorphous regions [32, 33].

For spidroins, ampullate and cylindriform silk have a higher percentage of well-aligned β-sheet which contributes to their higher strength compared to other spidroins [34]. Aciniform silks have lower alignment of β-sheets and a larger amount of α-helices which confers less strength but greater extensibility, resulting in greater toughness than other spidroins [34]. Flagelliform silks are predominately amorphous, providing the highest extensibility of the spider silks at the cost of low strength [34].

In major ampullate silk, the mobility of the protein backbone and sidechains, supercontraction, and extensibility of fibres exposed to water is proportional to proline content,

which in turn is proportional to the amount of MaSp2 relative to MaSp1 [35]. Supercontraction is an irreversible contraction and conformational change of the fibre along its length due to wetting, with water molecules incorporated into the structure of the fibre [36]. More generally, it is the random coil and helical content of MaSp2 which provides flexibility and mobility to the fibre [35].

Solution-state silk conformations are well characterised in terms of secondary structure, and some 3D structures are available. It should be noted that the solution structures of silk proteins are dependent on solution conditions [37-40], so structural details must be considered in context. An excellent example is the N-terminal domain of the *Bombyx mori* fibroin heavy chain which depends substantially on the solution pH, forming a random coil structure at pH 7 which reversibly converts to a β-sheet structure at pH 6 [38]. In-situ measurements of the full MaSp1 and MaSp2 show poly-proline II (PPII) and random coil structuring with a small amount of α-helix [41]. PPII helices are more flexible and extended than α-helices, and devoid of inter-residue H-bonding, and are generally though not necessarily formed by proline rich sequences [42]. Minor ampullate silk is similarly mostly random coil, but with a larger amount of α-helix [43]. The GGX motifs of ampullate silks likely form 3_{10}-helices, which are similar to an α-helix though more extended and with a distinct i→i+3 instead of i→i+4 H-bonding pattern, and the GA or poly-alanine motifs form crystalline β-sheets [44]. 3_{10}-helical segments often form type III β-turns consisting of 3-aa, and may contribute to β-sheet formation in the silk fibre [45].

The terminal domains of spidroins are typically α-helical. The N-terminal domain of MaSp1 forms a 5 α-helix bundle which undergoes pH sensitive dimerization [23], while the C-terminal domain of ADF-3 forms a 4 α-helix bundle which dimerizes by a disulphide linkage [46]. The C-terminal domain of AcSp1 also forms a 5 α-helix bundle which dimerizes [47]. The terminal domains of cylindriform silk also form α-helical bundles [21].

Regarding repetitive sequences, cylindriform and aciniform silks are well structured and also predominantly α-helical. Cylindriform forms α-helical bundles [21] and also shows an increase in β-sheet content induced by acidification [40]. The AcSp1 repeat domains consist of 7 α-helical bundle for *N. antipodiana* [48] and a 5 α-helical bundle for *A. trifasciata* [49], both with β-turn structures. The structure of AcSp1 repeats is discussed in detail in section 1.3. In contrast, pyriform and flagelliform silk are less α-helical. Pyriform silk is mostly random coil, but with a some α-helix, β-sheet and likely some PPII [50]. Flagelliform likely forms non-

typical helical structures based on sequence predictions that GPGXX type motifs form β-turns resulting in β-spirals when repeated [27].

1.2 Silk Biomaterials

1.2.1 Types, Properties and Applications of Silk Biomaterials

Silk fibres have excellent mechanical properties which rival or surpass synthetic materials. For spider silk fibres, dragline silk has the highest strength, aciniform the highest toughness, and flagelliform the highest extensibility [51]. The strength of dragline silk is comparable that of Kevlar, a synthetic material, but is coupled with much greater extensibility and toughness [52]. Flagelliform silk has extensibility similar to that of Nylon, but with much greater strength leading to nearly twice the toughness [52]. Aciniform silk falls between the two extremes, combining strength and extensibility to produce the highest toughness of the spider silks [51].

The biocompatibility [53-55] of silk proteins makes them desirable for medical applications. This desirability is further augmented by the fact that silk proteins can form a variety of materials such as fibres, films, sponges with variable pore size, and hydrogels which can be used to form scaffoldings for cell attachment and growth and implanted tissue supports [56-58]. Nanospheres can be used as drug delivery vehicles, which is discussed in detail in Section 1.5.2. Outside of medical applications, silk can be used as a textile [59], printed to form microfluidic surfaces and films with controlled optical properties [59, 60], an optical biosensor [61], air filter [62], or reaction tube for enzymes [63]. Silk proteins are thus highly versatile materials with desirable mechanical and biocompatible properties.

1.2.2 Theories of *in vivo* Fibre Spinning

In the major ampullate gland (Figure 2b), silk proteins are secreted into a long tail which is connected to the sac, with the sac storing the spinning dope until use [64]. Two main secretions are produced, with a highly concentrated solution of spidroin droplets being formed in the A-zone which is the tail and part of the sac, while the B-zone of the sac produces glycoproteins which coat the silk fibres [64]. To spin the fibre, the silk is pushed through a narrowing duct in which the proteins are aligned to form a preliminary fibre, and then through a

second narrow duct in which water removal and other processing occurs before fibre extrusion [64]. In the silkworm gland, fibroins are produced in the posterior silk gland (PSG) and stored in the middle silk gland (MSG), with preliminary fibre formation occurring in the narrowing anterior silk gland (ASG) [65] (Figure 2).

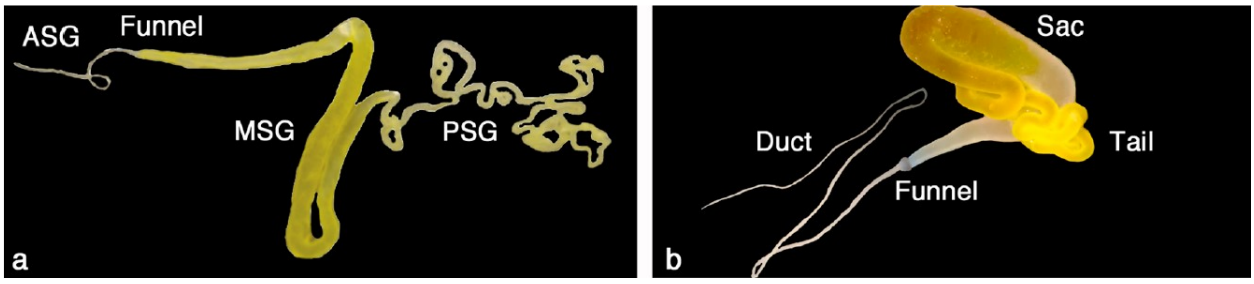

Figure 2: Anatomy of silkworm (a) and spider dragline (b) silk glands. ASG, MSG and PSG are the anterior, middle and posterior silk grands respectively. Reproduced from Andersson et al. [65]

Fibre spinning occurs by a combination of physical and chemical changes to a solution of silk proteins which has undergone phase-separation into a liquid crystalline or micellar state. In the liquid crystalline state, the proteins are arranged in a nematic state, with proteins aligned perpendicular to the direction of flow at the wall of the duct and curving inwards towards a parallel alignment at the centre of the duct [66]. As the solution of silk proteins moves down the duct, elongation and alignment of the proteins occurs parallel with the direction of flow, with the long and gradually narrowing duct allowing for rearrangement and alignment of proteins to occur [66, 67].

An alternative theory to liquid crystalline spinning is the micellar theory. In the micellar state, amphiphilic silk proteins arrange into spheres with hydrophobic and hydrophilic segments segregated at the interior and exterior, respectively [68]. Micelles are described in detail in section 1.4.1. Micelles formed by silk proteins may coalesce to form globules of micelles in the duct, which are compressed together and elongated as they are pushed further down the duct [69]. Micellar assemblies have been observed in native major ampullate spinning dope [70], although this does not necessarily mean that they persist down the spinning duct. In either case, silk protein monomers form a micellar or liquid crystalline liquid-liquid phase separation as they move down the duct, with increasing parallel alignment.

Moving down the spinning duct, there is a decrease in pH from 8.2 to ~6.2 for *B. mori* silkworm [71] and pH 7.6 to 5.7 in the major ampullate gland of *Nephila clavipes* [72] mediated by H^+ pumps. This acidification is associated with the micelle-like oligomerization of the N-terminus of the silk fibroin heavy chain [38] and dimerization of the N-terminus of Ma silk [23], suggesting that these domains encourage pH-dependent assembly of the native protein. The exchange of chaotropic (disorder promoting) with kosmotropic (order/aggregation promoting) salts as the spinning dope progresses down the spinning duct also encourages protein assembly [73]; consistent with this, the recombinant dragline silk-based protein eADF4(C16) transitions from nanofibrils to microspheres at increasing concentrations of potassium phosphate *in vitro* [74], which shows that salt concentration can control the nature of silk protein assembly. As well, eADF4 reversibly forms microspheres with increased potassium phosphate concentration, which convert to fibres when shear force is applied [75]. This phenomenon is pH-dependent, with eADF3 micelles able to form fibres at pH 6, but not pH 8 [75].

Mechanically, the silk solution is subject to both physical shear and elongational forces as it moves down the duct during the spinning process. Shear forces occur due to interactions of the solution with the wall of the spinning duct, causing heterogeneous flow rates across the solution due to the slower flow at the wall. Elongational forces occur due to an accelerated flow rate as the duct narrows, causing the extension of protein monomers in case of the liquid crystal theory, or elongation of micelles in case of the micellar theory [76]. The result is that proteins or micelles elongate and slide against one another, resulting in an increase in parallel alignment, and mechanically pulling apart the tertiary structure resulting in conformational changes that lead to the liquid-solid phase transition of fibre formation [75]. The precise mechanism of the conformational transition is not well understood. The liquid crystal and micelle theories of fibre spinning are compared in Figure 3 below.

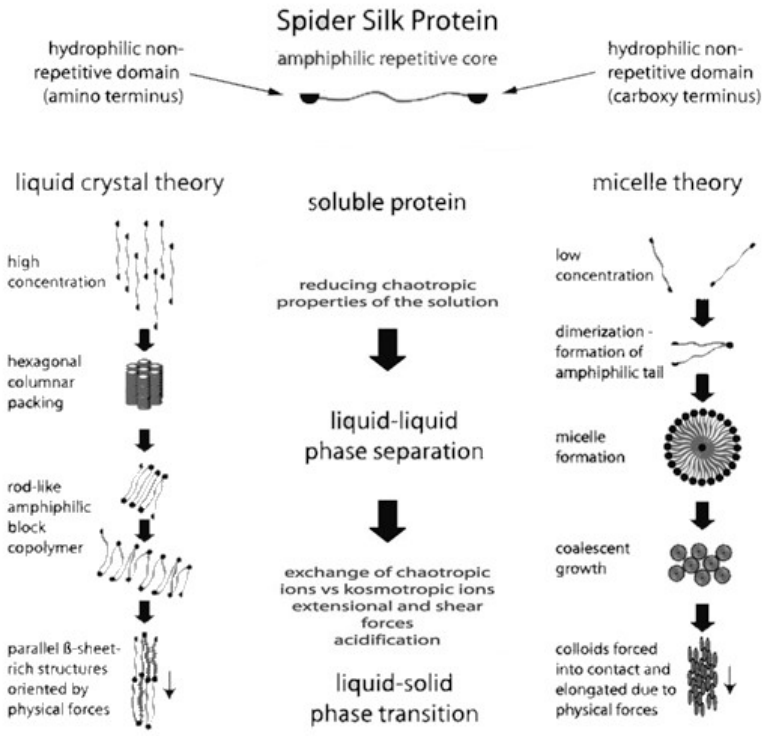

Figure 3: Comparison of liquid crystalline and micellar models of *in vivo* silk spinning within the major ampullate gland. Reproduced from Scheibel et al. [73]

Consistent with the micellar theory, the alignment of surfactant micelles can be observably induced by shear flow and this parallel alignment of elongated micelles can be stabilised by hydrophobic interactions between aromatic molecules of adjacent micelles [77]. The same stabilization can occur between protein micelles by alignment of hydrophobic residues and protein surfaces, ultimately leading to the alignment of β-sheets in fibres. Changes of geometry due to micelle elongation can cause conformational changes to the peptide of a lipid-peptide conjugate at the micelle surface, and the same may be true for the regions of silk proteins at the micelle surface [78]. Elongated micelles may also be formed and grow by the addition of spherical micelles end to end, as observed for micelles formed by an alkyl-linked peptide [79]. Similarly, silk fibroin can assemble into micelles followed by fusion of micelles to form nanofilaments with Silk I conformation during film drying in the absence of shear force [80].

These behaviours of peptide- and protein-based micelles support the mechanism that elongation and alignment of silk micelles due to shear and elongational flow results in increased inter-micelle interactions between β-sheets. The formation of these β-sheets is likely to be

induced by any or all of the factors detailed above, namely changes to pH, salt composition and mechanical forces, and fusion of micelles aligned end to end could lead to a liquid crystalline state and continuous fibre. This model of silk spinning is derived from observations of the major ampullate gland, however the anatomy of the aciniform gland is much different (Figure 1) and the spinning process less characterised. Namely, micelle formation (or lack thereof), the potential for a pH gradient and modulation of salt concentration have not been characterized for the aciniform silk gland.

1.2.3 Conformational Transitions Associated with Biomaterial Formation

Moving down the spinning duct, as introduced above, there is an overall transition towards β-sheet structure [37, 43] for silk proteins correlated with acidification and changes in salt content and shear forces. Minor ampullate silk retains more of its α-helical and random coil structure in the fibrous form [43] than does major ampullate silk, though both undergo conversion from mostly random coil to mostly β-sheet, with alignment of these β-sheets parallel to the fibre axis [37]. Silkworm fibroin undergoes an α-helix to β-sheet transition during fibre formation, which appears to occur as a two-step process [81]. Cylindriform, aciniform and pyriform silks are highly α-helical, and cylindriform converts to mostly aligned β-sheet in the fibre similar to ampullate silks [43]. In contrast, aciniform and pyriform silks only partially convert to β-sheet, retaining a relatively high degree of α-helical content, with relatively less alignment of β-sheet parallel to the fibre axis [37, 43]. Flagelliform silk is an exception, as fibre formation does not result in a transition to β-sheet or alignment within the fibre, instead leading to a heterogenous fibre held together by hydrogen bonding networks [43].

Despite the mechanisms discussed above (Section 1.2.2), it is important to note that many of these conformational transitions, although not fibre formation, may be induced through changes to pH and salt in the complete absence of shear force. The N-terminus of the silk fibroin heavy chain from *B. mori*, as an example, shows a drastic conformational change to β-sheet in response to only mild acidification from pH 7 to pH 6 *in vitro* [38], which matches the *in vivo* change in pH moving down the spinning duct [71]. The cylindriform silk protein is highly α-helical [21], but shows an increase in β-sheet content in response to acidification [40]. Major ampullate silk also shows a transition from random coil to β-sheet that is induced by acidification from pH 7.2 to 6.4 [39].

Silk protein micelles have been theorized to form with the hydrophobic regions of the repetitive sequence on the interior and the hydrophilic terminal domains on the exterior [69]. pH dependent oligomerization of the terminal domains may play a role in the micellization process and in parallel protein alignment. Oligomerization of the silk fibroin N-terminal is induced by acidification and is concurrent with the transition to β-sheet [38]. This oligomerization is likely due to the overlap of β-sheets between monomers of the N-terminal domain resulting in an interconnected network, which is similar to how β-sheets may overlap in the silk fiber [38]. Dimerization of the Ma silk N-terminal domains is also induced by acidification, though they remain α-helical [23]. Oligomerization of silk protein terminal domains may help to stabilize silk micelles through interactions at the micelle surface. In the case of the liquid crystal model of fibre spinning, oligomerization of the terminal domains may help to promote parallel alignment of adjacent silk proteins by locking their termini together at either end.

Overall, chemical changes in the spinning duct are responsible for changes to the protein conformation and initial parallel alignment of the proteins. Acidification over a small range of ~7.5 to ~6.0 pH induces a large conformational transition towards β-sheet in general [38-40] as well as oligomerization of at least some silk terminal domains [23, 38]. The decrease in pH moving down the spinning duct [71, 72] may therefore contribute to conformational changes which prime the protein for fiber formation, and encourage micellization or parallel alignment of silk proteins. Shear and elongational forces applied to the primed silk solution are then responsible for further parallel alignment and mechanical deformation of the tertiary structure, locking the β-strands and sheets of adjacent proteins into place and yielding fibres.

1.3 Recombinant Aciniform Silk Proteins

1.3.1 Structure of Recombinant AcSp1

The silk protein Aciniform Spidroin 1 (AcSp1) from *A. trifasciata* has been recombinantly expressed in *E. coli* as 1 to 4 repeat units termed W_n for Wrapping silk with *n* number of repeats [82]. The W_1 unit consists of the 19 kDa, 200-aa repetitive sequence of AcSp1 from *A. trifasciata,* which is directly linked end-to-end in the larger constructs, with the N-terminal serine of the N-terminal repeat unit of each construct removed for cloning purposes [82]. The structure [49, 83] and dynamics [84] of a single repeat unit W_1 have been determined

using NMR (nuclear magnetic resonance) spectroscopy. W_1 consists of a core domain of 5 α-helices flanked by a short 12-aa disordered N-terminal domain and a longer 51-aa disordered C-terminal domain [49] (Figure 4). It should be noted that these disordered terminal domains are part of the repetitive domain, rather than being the non-repetitive (and structured) terminal domains that flank the repetitive domain of the native protein [82]. In W_2 and larger constructs, these segments remain disordered, forming a linker between helical domains of adjacent W repeat units [49].

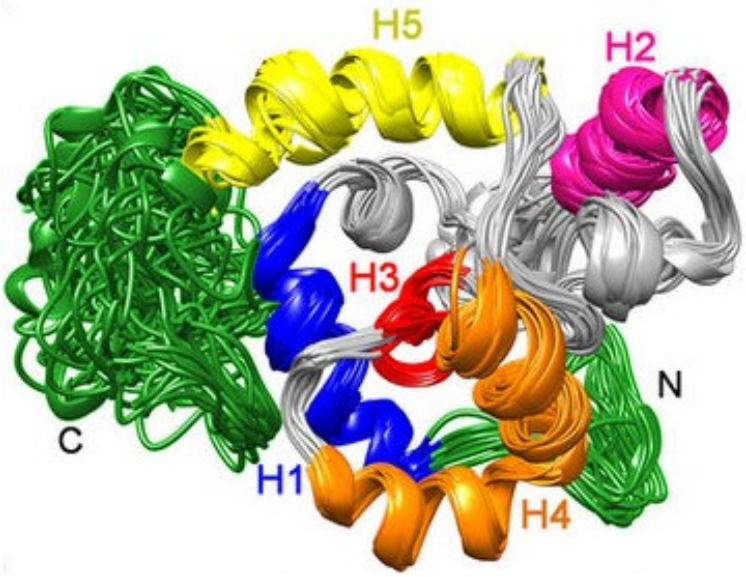

Figure 4: Overlay of the 20 lowest energy structures of the recombinant AcSp1 repeat unit determined using NMR spectroscopy. α-helices labelled H1 to H5, N and C terminal domains labelled N and C respectively. Reproduced from Tremblay et al. [49]

The ^{1}H-^{15}N HSQC (heteronuclear single quantum coherence) experiment can be used to correlate the chemical shifts of the hydrogen and nitrogen atoms in the amide bond for each amino acid in a protein, resulting in cross-peaks for each amino acid with a chemical shift position dependent on its local chemical environment [85]. The nuclear Overhauser effect (NOE) is a dipole-dipole interaction-based phenomenon between nearby atoms with dependence on both the distance between the nuclei and on motion [86]. In the case of the ^{1}H-^{15}N heteronuclear NOE for amides, the distance is fixed by covalent constraints, allowing measurement of the degree of motion (dynamics) of the protein backbone by measuring the enhancement occurring due to the NOE between the nitrogen and hydrogen atoms of each amide

bond of each residue [87]. In the W_2 construct, very few changes to the helical domain are observed with respect to W_1, with only minor chemical shift changes of assigned residues and minor differences to ^{1}H-^{15}N heteronuclear NOE enhancement factors and backbone dynamics [49]. Minimal changes are introduced to the disordered regions that form the link between the helical domains of the two repeat units [49]. Overall there are minimal interactions between the individual repeats and no change in secondary structure with an increasing number of repeats observable by CD (circular dichroism) spectroscopy [82], implying that the repeat units behave independently from one another with little interaction. This is, in turn, consistent with a "beads-on-a-string" model with the structured helical domains forming the beads and the intrinsically disordered linkers forming the strings.

The α-helical core domain shows consistent rigidity along the peptide backbone, while the disordered tails have greater molecular motion, as seen by per-residue measurement of T_2 relaxation times [84]. T_2 relaxation measures the rate of return to equilibrium of excited nuclei in the transverse plane, which occurs more slowly with increased molecular motion [88]. Helix 5 and the region directly below it in the globular domain are significantly easier to disrupt, unfolding earlier than the other regions of the protein as the concentration of chemical denaturant is increased [49, 89]. The same regions are also more prone to hydrogen-deuterium exchange than other helices, which indicates that interactions between helix 5 and the underlying residues are more easily disrupted than those of the other helices [49], and that this region of the protein is more dynamic [84]. These features support a hypothesis that destabilization of helix 5 and associated regions initiate the conformational disruption and transition from mostly α-helix to mixed α-helix and β-sheet [82] that is prerequisite for aciniform silk-based biomaterial formation.

As another clue to this conformational transition, several hydrophobic residues (phenylalanine and tyrosine) have relatively high solvent exposure rather than being buried in the protein fold. Six of these are in the C-terminal disordered region, with one directly C-terminal to helix 5, two in the well-buried helix 3 in the protein core, one in helix 2, and one in the N-terminal disordered region [49]. As it is generally energetically favourable for hydrophobic residues to be shielded from aqueous solution within a protein structure [90], these exposed hydrophobic residues may play a role in encouraging or stabilizing conformational transitions towards silk biomaterials. Overall, the protein does not show any distinctly separated

hydrophobic or hydrophilic surfaces that would indicate amphipathy (Figure 5) [49] in contrast to other silk proteins [24, 69], raising questions about the potential driving force and likelihood of an AcSp1 liquid-liquid phase transition and self-assembly as discussed in Section 1.2.2.

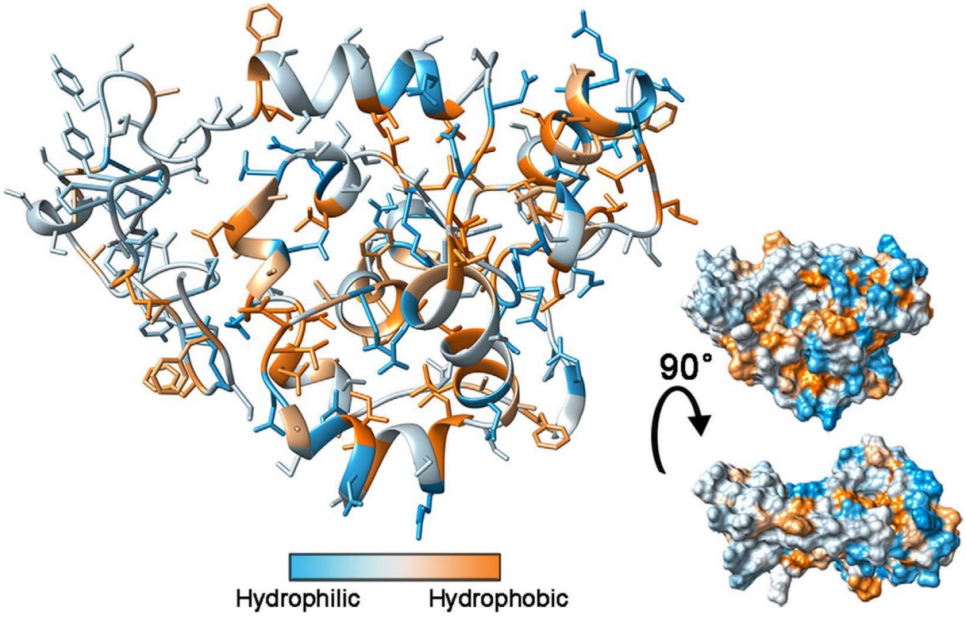

Figure 5: Hydropathy of the AcSp1 repeat unit (W_1). Reproduced from Tremblay et al. [49]

The W_1 protein is highly stable under a variety of solution conditions. There is no significant change to the secondary structure between phosphate and acetate buffers, and from pH 5 to 7 in phosphate buffer, in contrast to the β-sheet conversion seen for some other spider silk proteins over the same pH range [39, 40], as discussed in Section 1.2.3. Hence, it is not clear what solution conditions are required for conformational changes to the repetitive sequence to occur, or if the protein does not undergo such conformational changes until it transitions to an insoluble fibrous state. The protein also shows reversible thermal denaturation with a melting temperature (T_m) of ~71 ºC, with little precipitation even after incubation at 90 ºC for 15 min [91].

1.3.2 Tryptophan Substitutions to Recombinant AcSp1

The *A. trifasciata* W unit does not contain any tryptophan residues [82], allowing for the use of substituted tryptophan residues as probes that may be measured without any background interference. Tryptophan residues can be used as sensitive conformational probes both by intrinsic fluorescence [92] and by ^{19}F NMR of fluorinated tryptophan [93]. Four tryptophan

substitutions were made to the W_1 protein, targeting areas of interest within the protein structure [89]: residue F90 within helix 3 at the well folded core of the globular domain, R36 directly beneath helix 5, F146 directly C-terminal to helix 5, and Y169 in the disordered C-terminus (Figure 6). These mutation sites were generally chosen to replace aromatic residues with aromatic tryptophan to decrease the risk of large perturbations of the protein conformation, except for R36 which replaces the long aliphatic chain of cationic arginine with the similarly bulky tryptophan ring. These tryptophan substitutions allow for tracking of solvent exposure at regions in the protein that are likely to undergo conformational changes along the pathway to fibre formation by fluorescence, as is discussed in detail in Section 1.6.1. All tryptophan variants gave overlapping CD spectra with the wild-type spectrum, indicating that substitution of tryptophan at these sites did not significantly affect the secondary structure of the protein, and all are capable of fibre formation [89]. The structures of the variants were not determined experimentally; however, the wild-type structure was recalculated after mutating the residue *in silico* and removing its NOE restraints, with the resultant structures of the variants being very similar the wild-type W unit in terms of secondary and tertiary structure [89].

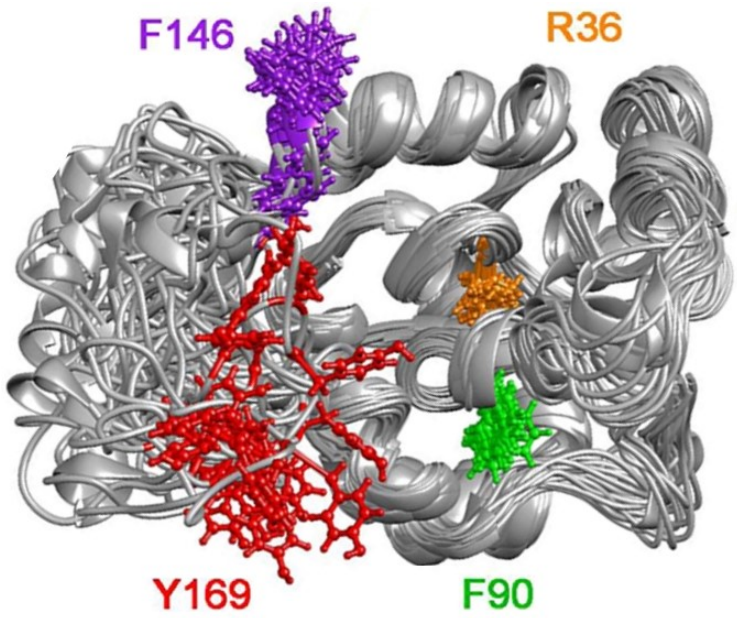

Figure 6: Tryptophan substitution sites within the recombinant AcSp1 repeat unit. Reproduced from Sarker et al. [89]

Though the secondary structure of each variant appears well conserved, chemical shift perturbations are apparent by ^{1}H-^{15}N HSQC [89] which likely reflects localized changes to

packing, tertiary structuring, and environment induced by the introduction of a fluorinated aromatic moiety. The Y169W substitution shows very few cross-peak displacements, as expected due to its location in the disordered C-terminal tail region. The F146W substitution induced minor cross-peak displacements to helix 4 and the region below helix 5, as well most of the residues in helix 5 were not detectable due to peak broadening, a phenomenon which can occur when the hydrogen of the amide bond exchanges with hydrogens of the solvent, or if dynamic motion occurs, at a timescale similar to the measurement time. The peak broadening of helix 5 may be an indication of increased hydrogen exchange due to increased solvent exposure or increased dynamic motion of the backbone [94]. As F146 is directly C-terminal to helix 5, perturbation of this helix is expected. The R36W substitution beneath helix 5 caused significant disruption to cross-peaks in its local region and to helices 3 and 4. Due to the replacement of a charged arginine with a hydrophobic tryptophan and the orientation of R36 towards the helical core [49], these perturbations are reasonable. Interestingly there was no perturbation of helix 5 residues despite significant perturbation to the region beneath it [89]. The F90W substitution caused the most chemical shift perturbations, affecting helices 2, 3, and 4, which is reasonable due to its location at the core of the globular domain [89].

When labeled with 5-fluorotryptophan and characterized by ^{19}F NMR, each mutant exhibited a distinct ^{19}F chemical shift [89]. Denaturation of the W_1 variants was tracked by ^{19}F NMR, showing no change for the chemical shift for the Y169W residue, consistent with its location in a region that is already disordered. The F146W residue, with some helical structure and pointing away from the surface of the protein, showed a slight chemical shift perturbation at ~3 M urea. The largest change in chemical shift occurred for the F90W residue at ~3 M urea. Interestingly, the R36W residue showed an earlier transition, beginning at ~1.5 M urea and ending at ~2.5 M [89]. Denaturation of the wild-type W unit tracked by CD spectroscopy showed that significant changes to secondary structure begin at ~2 M urea, with the majority of the unfolding process occurring above 2.5 M [49]. The F146W residue did not show a significant chemical shift until ~2.75 M [89], supporting that the secondary structure of helix 5 is not disrupted until after the transition of the R36W residue. This suggests that the earlier transition of the R36W chemical shift is due to disruption of the tertiary structure, plausibly due to loosening of helix 5 from the surface of the protein and perturbations or increased dynamics of the underlying region. The F90W residue undergoes a large chemical shift change past 3 M

urea, consistent with the behaviour expected upon denaturation for a well-buried residue within the stable helical protein core [89].

The broad ^{19}F linewidth of R36W compared to the exposed Y169W and F146W is consistent with R36W being well buried in the protein, reflected by the *in silico* mutant structure having ~4% solvent accessible surface area [89]. However, R36W also shows a much larger solvent-induced-shift than the other mutant residues upon change from 9:1 H_2O:D_2O to 1:9 H_2O:D_2O, with induced chemical shift perturbation is close to that of free 5-fluoroindole [89]. This result indicates that the residue is solvent accessible, which may be due to two cavities seen in the *in silico* structure [89] and increased dynamics of the region [49], but also may be arise from interactions with the cationic side chain of R50 [89]. In general, the behaviour ^{19}F chemical shifts are complex and highly sensitive to the local chemical environment around the fluorine atom [93], making interpretation difficult.

1.3.3 Biomaterial Formation by Recombinant AcSp1

Recombinant AcSp1 with at least two repeat units (W_2) readily forms fibres from a solution of as low as 0.04 mg/mL protein concentration with shear stress induced by pulling from the solution with a pipette tip [82]. W_1 cannot form fibres [82], with a plausible reason being that each protein, in this instance, has only one repeat to interact with adjacent proteins, meaning that entanglement of multiple proteins that is required to form an interlocking network cannot take place. W_4 fibres produced by this method have reasonable mechanical properties, with a tensile strength of ~115 MPa, extensibility of ~37% and toughness of ~34 $J \cdot cm^{-3}$ [82]. For comparison, the naturally spun AcSp1 silk has a tensile strength of 687 MPa, extensibility of 86% and toughness of 376 $J\ cm^{-3}$ [14].

To improve fibre quality and reproducibility, more advanced artificial wet-spinning methods have been developed [95]. In the first such method, lyophilized silk protein is dissolved in a solvent such as hexafluoro-2-propanol (HFIP) to form a spinning dope to a final concentration of 8% w/v. The secondary structure of the protein in the spinning dope [95] is well preserved with respect to that of aqueous conditions [82]. The spinning dope is then passed through a syringe needle into a bath of 95% ethanol and collected onto a rotating cylinder, with rates controlled by a spinning apparatus. These fibres without further treatment are termed *as-spun* (AS). After collection of AS fibres, stretching can be applied within H_2O to 4 times the

original AS length. W_3 AS fibres in HFIP formed by wet spinning into 95% ethanol yielded diameters of ~23 μm, reduced to 9 μm after stretching by 4x, with the post-spin stretching process more than doubling tensile strength and toughness [95]. Fibres formed from a trifluoroacetic acid and trifluoroethanol (TFA/TFE) dope had roughly the same diameters, but exhibited greatly improved toughness and extensibility after stretching compared to HFIP based fibres, alongside higher strength [96]. The observed change in diameter upon post-spin stretching indicates that stretching causes an irreversible compaction of fibres, plausibly due to the stretching and straightening out of protein chains improving the overlap and alignment between the β-sheets within the fibre. Comparing the wet-spinning and hand-drawing techniques for the HFIP based fibres described above shows that hand-drawn W_3 fibres have much smaller diameters (1.8 ± 0.1μm) and slightly less strength (79 ± 28 vs. 92 ± 8 MPa), but have much greater extensibility (21 ± 10 vs. 2.6 ± 0.6 %) and toughness (14 ± 8 vs. 1.3 ± 0.3 $MJ \cdot m^{-3}$) [95].

Hand-spun fibres are more similar in diameter to the natural silk than the wet-spun fibres, as is the spinning method. However, the mechanical properties of hand-draw fibres have greater variability owing presumably to the inherent human error in draw rate which would affect shear force. In the case of wet-spinning, the protein solution is pushed through a syringe needle into an alcohol solution in which it is insoluble [95]. In the case of hand-drawing, the surface of a solution containing silk protein is pulled outward into a narrowing cone with no alcohol involved [82]. In both cases, shear forces are applied, but the size and chemical nature of the interface between the protein solution and newly forming fibre are different.

Providing insight into the fibre formation mechanism, hand-pulled fibres with the end left in solution were fixed and observed by scanning electron microscopy (SEM) showing many nanofibrils branching from the end of the fibre which was still in solution. Coating these nanofibrils and the slide were many spherical particles [82], which would be consistent – although not conclusive proof – of the micelle theory of fibre assembly applying to aciniform silks. Additionally, HFIP and TFA/TFE spinning dopes contained micro- and nano-spheres respectively [96]. The smaller size and lesser hetreodispersity of nanoparticles in TFA/TFE and their formation of interconnected networks rather than the individual clusters formed in HFIP [96] may be related to the difference in the properties of fibres formed from the two dopes. This supports a model of fibre spinning in which nanoparticles combine into nanofibrils, and nanofibrils into the final fibre, along with conformational changes initiated by the disruption to

helix 5. The formation of recombinant AcSp1 fibres involves a transition from ~40% α-helix to 32% α-helix and 28% β-sheet [82], with α-helices and β-sheets aligned roughly parallel to the fibre axis [2]. Other forms of recombinant aciniform silk biomaterials, such as films and spheres, have not yet been investigated structurally.

1.3.4 Micellization Behaviour of Recombinant AcSp1

The W_1 protein is capable of forming micelle-like nanoparticles in phosphate buffer (pH 7.5), falling into two separate populations of 50 and 220 nm average diameters as observed by dynamic light scattering (DLS) [91]. For comparison, the hydrodynamic diameter of the W_1 monomer is 4.3 nm [49]. The larger population reaches particle sizes of up to ~450 nm, and although samples were passed through a 450 nm filter, their incubation for 12 h before measurement did not result in the reformation of any larger particles consistent in size with particles that would have been removed by the filtration step. As well, the intensity weighted function shows a normal decay to zero intensity rather than a truncation at 450 nm, and this is corroborated by scanning electron microscopy (SEM) of unfiltered samples [91]. Nanoparticle formation by W_2 or constructs with more repeat units has not been formally investigated, though during measurement of the hydrodynamic radii of W_2 and W_3 by DLS, only the monomeric species was detected [49]. However, it is possible that a small nanoparticle population may have been present that was not detected, depending on signal-to-noise, digital filtering, or fitting method.

Micelle-like behaviour of W_1 has been probed by the hydrophobic fluorophores 1-anilinonaphthalene-8-sulfonic acid (1,8-ANS) and pyrene, both of which change fluorescence emission behaviour based on the hydrophobicity of their local environments [91]. 1,8-ANS shows little emission in an aqueous environment, but much higher intensity and a shorter emission wavelength in a hydrophobic environment [97]. Pyrene shows an increased emission intensity in more hydrophobic environments, but also exhibits a characteristic change in the ratio of the first and third vibronic peaks (I_1 and I_3) of its emission manifold [98, 99]. Namely, the emission intensity at I_1 relative to I_3 (I_1/I_3) decreases from a value of 2 in water to a value of 0.75 in hexane, concomitant with a hydrophobicity increase [98]. Fluorescence is described in detail in Section 1.6.1. Protein-fluorophore interactions may contribute to a change in the hydrophobicity of the fluorophore environment, including binding of the fluorophore to

hydrophobic protein surfaces and encapsulation of the fluorophore into the hydrophobic interior of a protein nanoparticle or micelle. The micelle interior is a more hydrophobic environment than the micelle surface due to higher solvent exclusion, and so above the critical micellar concentration (CMC) – the threshold concentration at which micelles begin to form [100] - there should be a progressive decrease in the I_1/I_3 intensity ratio as the population of micelles increases due more pyrene molecules being partitioned into hydrophobic micelle interiors. The concentration at which the I_1/I_3 ratio begins to decrease occurs when enough micelles have been formed to result in a measurable change of pyrene emission and, therefore, provides an approximate measurement of the CMC. The theory of micelle formation is detailed in section 1.4.1.

To estimate the CMC of W_1, pyrene fluorescence was measured after an incubation with the protein for 24 h at 4 ºC and 1 h at room temperature in order to allow pyrene diffusion into micelles, followed by serial dilutions maintaining a constant pyrene concentration. Incubating at 4 ºC helps to prevent precipitation of the protein. The resulting relationship between I_1/I_3 and W_1 concentration is roughly sigmoidal, reaching a ratio of 1.1 at ~150 μM [91], indicating that the large majority of pyrene is in a hydrophobic environment. For comparison, the I_1/I_3 ratio of pyrene in SDS reaches as low as ~0.75 [98]. The sigmoidal behaviour observed is similar to that seen in CMC measurements of other surfactants using pyrene [101] and reflects a transition in the hydrophobicity experienced by pyrene molecules due to the dissolution of micelles, whereas without micelle formation a linear trend may be expected due to binding to the protein surface. The start of the sigmoidal curve observed for W_1 occurred at ~20 μM, leading to an inference of a CMC of ~20 μM [91].

The emission maximum of 1,8-ANS also showed a large blue-shift past ~20 μM, but the change in intensity between 18 and 71 μM was comparable to that between 0 and 18 μM. However, the difference of emission intensity between the 88 μM and the 71 μM samples was ~3.3x larger than the difference between the 71 and 18 μM samples. The 88 μM spectrum also showed a shouldering effect, indicating a second population of 1,8-ANS molecules in a more hydrophobic environment. The 88 μM sample was not diluted, and so the mechanical mixing to produce the 71 μM sample may have been responsible for disruption of complexes. It may be the case that the blue-shift at lower concentrations was due to surface binding of 1,8-ANS to the protein, the two of which are at comparable concentrations. It is not clear what effect binding of

1,8-ANS or pyrene to the surface of W_1 may have on the assembly of W_1 nanoparticles, whether disfavouring or favouring their formation.

1.4 Solution-State Assembly of Proteins

1.4.1 Theories of Micellization and Phase Separation

Micelles [102] are formed through the self-assembly of amphipathic molecules such that their hydrophobic regions are shielded from aqueous solution as the micelle interior, and their hydrophilic regions are exposed to solution as the micelle surface [68]. This process is affected by energetically favourable packing of hydrophobic regions in the solvent-excluded micelle interior and unfavourable repulsion of charged hydrophilic regions, if present, at the hydrated micelle surface [68].

The radius of a micelle is necessarily dependent on the total length of the hydrophobic region of the molecule that forms its core. Though micelles are generally spherical, elongated *wormlike* micelles may form at a higher concentration than spherical micellization with a secondary CMC [103], which in the case of peptides and proteins can be associated with a conformational change [78]. This cylindrical shape allows the micelle to grow in size while maintaining the limit that the radius cannot be longer than the length of the hydrophobic region. The formation of micelles can be defined through a mass-action model using an equilibrium between monomeric and micellar species [104]:

$$mP \leftrightarrow P_m \quad (1)$$

where P is the protein, or other monomer, P_m is the micellar form, and m is the aggregation number. The equilibrium constant (K_m) for this mechanism is then [104]:

$$K_m = [P_m]/[P]^m \quad (2)$$

which can also be presented with respect to mole fractions [104]:

$$K_m = X_m/mX^m \quad (3)$$

where X_m and X are the mole fractions of protein in the micelle and monomer forms, respectively. This is related to the free energy of micellization per monomer (ΔG_m^0) described by [104]:

$$\Delta G_m^0 = -RTlnK_m = -RTln\left[\frac{X_m}{mX^m}\right] \quad (4)$$

or

$$m\frac{\Delta G_m^0}{RT} = mlnX - lnX_m + lnm \quad (5)$$

where *R* is the ideal gas constant and *T* is the absolute temperature. The free energy may also be expressed in terms of the CMC [105]:

$$m\frac{\Delta G_m^0}{RT} = \ln\left[\frac{m^2(2m-1)}{m-2}\right] + (m-1)ln\left[\frac{m(2m-1)}{(m-1)(2m+2)}\right] + (m-1)\ln[CMC] \quad (6).$$

Charged surfactants are surrounded by a counter ion shell, the thermodynamic contribution of which can be described using [106]:

$$mP + (m\text{-}p)C \leftrightarrow P_m \quad (7)$$

where p is the charge of the ionic micelle and C is the counter ion. Then, the equilibrium constant is described by [107]:

$$K_m = \frac{X_m[P_0]^{1-m}}{m(1-X_m)^m([P_0]\left(1-X_m\left(1-\frac{p}{m}\right)\right)+X)^{m-p}} \quad (8).$$

Essentially, the formation of micelles can be described by the number of surfactants per micelle, surfactant concentration, and micelle surface charge based on the equations above. Ultimately, an experimentally measured CMC and free energy and be used to calculate the average aggregation number, based on Eq. 6. A phase separation can be thought of as a case where the aggregation number approaches infinity, reflecting a single contiguous aggregated state involving all molecules with infinite potential size. Factors not addressed by these formulae include the potential for temperature dependencies of both the aggregation number and CMC. Deviations from this theoretical description of energetics can also result due to non-spherical morphologies, large polydispersity of micelle size, and protein conformational changes due to micellization [108]. The complex assemblies found in the major ampullate gland [70] can not be fully described by these formulae, but onset of assembly at a CMC is applicable.

1.4.2 Assembly at Liquid-Air Interfaces

Surfactants must first diffuse to the surface to adsorb, and so initially the assembly rate is diffusion-controlled and dependent on the concentration of surfactant in solution, assuming no barrier to adsorption once at the surface [109]. To account for different surface properties and surfactant properties, many specialized adsorption isotherms are available [110]. A common and simple model of the liquid-air adsorption/desorption equilibrium is the Langmuir isotherm described by [109]:

$$\frac{d\Gamma}{dt} = k_a c\Gamma_\infty \left(1 - \frac{\Gamma}{\Gamma_\infty}\right) - k_d * \frac{\Gamma}{\Gamma_\infty} \quad (9)$$

where k_a is the adsorption rate constant, k_d is the desorption rate constant, and Γ_∞ is the maximum surface concentration. This results in the equilibrium described by [109]:

$$\Gamma = \Gamma_\infty \left(\frac{K_L c}{1 - K_L c}\right) \quad (10)$$

where the equilibrium constant $K_L = k_a * k_d$

If surface desorption is negligible, then the initial adsorption is diffusion-controlled and the surface concentration can be described as a function of the diffusion coefficient (D) by [111]:

$$\Gamma = 2c\sqrt{\left(\frac{Dt}{\pi}\right)} \quad (11)$$

where Γ is the surface concentration, c is the solution concentration, and t is time.

The Gibbs adsorption equation may be applied for the case of low solution concentrations such that the surface is not saturated, relating the surface pressure to the solution concentration [109, 112] as follows:

$$dP = nRT(\Gamma d\ln c) \quad (12)$$

where Γ is the surface concentration at saturation, P is the surface pressure, *T* is the absolute temperature, *R* is the ideal gas constant, and n is 1 or 2 for non-ionic and ionic surfactants respectively.

In a purely diffusion-controlled adsorption process, the only barrier to adsorption is the ability of a surfactant molecule to reach the interface. This, however, is an idealised model. More realistically, there may be a thermodynamic barrier to adsorption once a molecule reaches the interface. Such barriers include steric hindrance due to other molecules already adsorbed or, as may occur in the case of proteins, conformational rearrangement [109]. In these cases, overcoming this barrier becomes the rate-limiting step. As more surfactants assemble at the surface, steric hindrance and lack of free surface area decrease the role of diffusion and surface assembly is dominated by rearrangements at the surface.

A caveat to the Langmuir isotherm is that it does not account for interactions between surfactant monomers or rearrangement at the surface and so it is not accurate for complex surfactants such as proteins [113].

Specifically, surface adsorption of proteins involves more variables than the typical surfactant model due to their large and complex nature, involving charge distribution, buried

hydrophobic surfaces, interactions between domains, and inter-protein interactions [114, 115]. Intermolecular adhesion between proteins is the main contribution to protein surface pressure, with small contributions from electrostatic interactions and molecular motion [116]. Additionally, proteins that adsorb to the interface generally undergo surface denaturation, resulting in conformational changes after adsorption [114, 117, 118]. This gives three stages to protein assembly at the liquid-air interface: (1) accumulation at the surface by adsorption with concurrent conformational change, (2) film formation by inter-protein interactions and alignments, and (3) film maturation by further conformational adjustments and alignment. The extent to which proteins affect surface tension is largely related to their relative ease of changing conformation at the surface in order to adsorb by exposing hydrophobic surfaces to the liquid-air interface. This means that highly flexible proteins have greater surfactant effect due to their propensity to change conformation [116]. These structural rearrangements expose hydrophobic protein residues to the air interface and compete with native protein folding, which stabilizes hydrophobic residues within the protein [119].

Due to the ability of silk proteins to undergo large conformational changes toward β-sheet in response to mild changes in solution condition (as detailed in Section 1.2.3; [38, 40, 78]), it is reasonable to expect that they can readily change conformation in order to adsorb to the liquid-air interface and therefore have good surfactant potential . Silkworm fibroin and Ma spidroins show surface assembly and conformational change once at the surface, resulting in a visco-elastic gel-like surface layer in contrast to proteins such as lysozyme which do not form biomaterials [118-120]. Tracking surface concentration and surface pressure of several proteins shows that there is a delay between their accumulation at the surface and the change in surface pressure, which shows that formation of the surface film begins at a minimum surface concentration dependent on the protein and is likely delayed by the kinetics of conformational change and formation of inter-protein networks [116]. Film formation can occur heterogeneously, with protein islands formed at the surface initially followed by interconnection between these islands [121].

1.5 Protein Nanoparticles as Drug Delivery Vehicles

1.5.1 Applications of Nanoparticles to Chemotherapeutic Delivery

Nanoparticles can be formed from a variety of materials, most commonly liposomes, proteins, peptides, silica, gold, dendrimers, and polymers [122]. These can be hard non-degradable materials such as gold and iron oxide coated with the molecule(s) of interests, or soft materials such as liposomes and proteins which encapsulate and release their cargo [122]. Though drug delivery [123] is the focus here, nanoparticles have other applications such as tissue imaging [124].

Drug delivery vehicles allow for the controlled release and cellular targeting of the drug molecules they carry [123]. This is of interest for cancer treatment due to the high toxicity of chemotherapeutics to healthy cells [123]. Drug delivery vehicles therefore have the potential to lessen the negative side-effects of existing chemotherapeutics by enabling selective uptake of these drugs by cancerous cells. There are currently numerous nanoparticle medicines which have been approved for clinic use or are undergoing clinic trials [125].

The design of effective nanoparticle systems must take into account a number of factors [126]. Most importantly, the nanoparticles must preferentially accumulate at the target site. This accumulation can occur by passive or active targeting [127]. Passive targeting relies on the *enhanced permeability and retention effect* (EPR), discovered in 1986 [128], by which nanoparticles enter tumours more easily than other tissues due to a greater vascular permeability [129] and have difficulty leaving due to poorly developed lymphatic systems [130]. In competition to passive targeting, nanoparticles entering the bloodstream can be sequestered by macrophages and other phagocytes, resulting in off-target accumulation [131]. A major contribution to sequestering is the coating of nanoparticle surfaces by proteins within the bloodstream forming a protein corona [132], which results in opsonization for phagocytosis and masking of active targeting features on the nanoparticle surface [126]. A common method to reduce the formation of a protein corona is ligation of PEG (poly-ethylene glycol) molecules to the nanoparticle surface, decreasing blood clearance rates and improving biocompatibility by altering the surface chemistry [133].

Nanoparticles can be administered as an aerosol rather than intravenously in the case of lung cancers [134], delivered transdermally for skin cancers [135], or delivered orally [136].

Nanoparticles can also be actively targeted to cancerous cells by modifying the particle surface such that it has an affinity to some molecular feature of the target [127]. As an example, the first actively targeted nanoparticle tested clinically, BIND-014, is coated with molecules of 2-(3-((*S*)-5-amino-1-carboxypentyl)ureido) pentanedioic acid (ACUPA), which binds specifically to the surface protein PSMA (prostate-specific membrane antigen) expressed by some prostate cancers [137]. Once localized at the target site, nanoparticles may release their cargo into the interstitial fluid or enter cells by endocytosis, being sequestered in cellular endosomes and subsequently lysosomes [138]. The acidic nature of endosomes and lysosomes can be exploited by pH sensitive nanoparticles, triggering drug release once inside the cell. This may be due to a change in the charge of the nanoparticle which affects drug binding, disassociation or degradation of the nanoparticles at acidic pH [139, 140]. Nanoparticles in the cell can be further targeted to the nucleus, improving the effectiveness of their drug cargo [141].

Nanoparticles must release their drug cargo at the target site in order to serve their purpose, and so need to remain stable in the blood for long enough to accumulate at the target site. As such, the kinetics and selectivity of drug release is important to the effectiveness of nanoparticles. Properties affecting the targeting of nanoparticles include size and morphology, surface charge and hydrophobicity [127]. In one study, gold nanoparticles showed size-dependent tissue distribution in mice, with smaller particles (15 nm) showing greater overall tissue distribution, particularly in the lungs and kidneys, while larger nanoparticles (100-200 nm) mostly accumulated in the liver and also showed improved pancreatic localization [142]. Morphologically, non-spherical nanoparticles tumble in the bloodstream resulting in increased lateral diffusion towards the endothelium wall where adhesion can occur as the first step towards extravasation into the target tissue [143]. In one study, gold nanoparticles with no charge or zwitterionic nanoparticles with net neutral charge show much greater blood plasma retention compared to charged particles, with positively charged particles having more than twice the clearance rate of negative particles [144]. Increased plasma retention was also correlated with increased accumulation in tumours [144]. Heterogeneity of tumour biology, even within the same patient, affects nanoparticle-tumour compatibility [145]. As well, drug-nanoparticle compatibility affects the properties of drug uptake and release by nanoparticles [146]. Drug delivery by nanoparticles is affected by complex features of tissue and tumour biology, cellular and intra-cellular targeting strategies, drug release kinetics and selectivity, nanoparticle

composition, and drug compatibility. Therefore, the investigation of new nanoparticle materials is important for the development of new nanomedicines.

1.5.2 Silk Protein Particles for Drug Delivery

Silk-based materials are attractive as drug delivery vehicles due to their good biocompatibility, with regard to hypoallergenicity [53]; biodegradability [54]; and, hemocompatibility [55]. Hypoallergenicity refers to a low immune response, biodegradability to degradation and removal from the body, and hemocompatibility to low coagulation, hemolysis and clearance from the blood. Fabrication of silk materials also does not require toxic chemicals or solvents, as discussed in section 1.5.3, which is important for chemically-sensitive cargo such as proteins. Silk fibroin proteins from silkworm and spider silk-derived proteins are capable of forming nanoparticles with drug carrying capacity [147, 148]. To date, no approved silk nanoparticle medicines are available nor are clinical trials underway; however, silk nanoparticles have been formed by a wide variety of methods and have a demonstrated capacity for drug uptake, release, cellular uptake and effective drug delivery *in vitro*, as discussed here. Although the focus here is on nanoparticles, other silk biomaterials such as hydrogels, fibres and films can be applied to drug delivery [149]. As well, other non-silk protein nanoparticles have been investigated for medical applications [150].

Silk fibroin nanoparticles are generally based upon the natural protein regenerated from silkworm cocoons, and account for the majority of silk-based nanoparticles studies to date. Active and passive targeting features have been applied to silk fibroin as well, with demonstrated drug delivery *in vitro*. In one example, nanoparticles were coated with folic acid to actively target the folate receptor and were capable of pH-induced release of doxorubicin in cancer cells, presumably due to a disruption of the electrostatic interactions between the drug and nanoparticles by protonation of the silk proteins [151]. Another study produced fibroin nanoparticles which provided pH-dependent release of doxorubicin in the lysosomes of breast cancer cells [152]. Nanoparticles which were PEGylated to improve stability [153] could deliver drugs to breast cancer cells as could nanoparticles produced by a microdot printing technique, where droplets of silk solution are deposited and dried [154]. In another study, silk fibroin nanoparticles were shown to deliver vascular endothelial growth factor (VEGF) to carcinoma cells, with slow release over several days [155]. Microfluidic technology has also been applied

to silk nanoparticle production, allowing more precise control over mixing rates and ratios [156]. Silk fibroin nanoparticles can deliver drug molecules by a variety of routes, including transdermally [135], through oral delivery to mice [136], and to a human cell line in an *in vitro* lung model system as an inhalable powder [134]. Although the focus here is on silk nanoparticles, hybrid materials such as silk-chitosan blends [154], silk coated liposomes [157], and magnetic silk nanoparticles [158] have also been produced.

Spider silk proteins derived from dragline silk have also been investigated as nanoparticle materials, using recombinant proteins such as eADF4(C16) [159], for which particles can incorporate and release protein cargo *in vitro* [160]. eADF4(C16) can also be ligated to cell penetrating peptides such as Tat and poly-arginine to improve cellular uptake and nuclear targeting [161]. Spider silk proteins have also been engineered to modify their drug and cell interactions. For example, substitution of eADF4(C16) glutamate residues to lysine reverses the charge from anionic to cationic, greatly improving cellular uptake of nanoparticles through an unresolved mechanism [161] and enabling uptake of anionic nucleic acid drugs[162]. Silk ligated to a ligand for the Her2 receptor overexpressed on some cancer cells forms nanoparticles with improved delivery of doxorubicin through active targeting [163]. One engineered dragline silk protein based off MaSp1 incorporates poly-l-lysine domains and tumour targeting peptides, forming nano complexes with increased binding affinity to their pDNA cargo [164].

1.5.3 Methods of Producing Protein Nanoparticles

The principle behind nanoparticle formation is to precipitate a solution of soluble protein in a controlled and reproducible way, resulting in a defined particle size and morphology. As such, there are as many methods of protein nanoparticle production as there are methods of protein precipitation, Desolvation and salting out are the most common such methods, likely due to their simplicity. A representative selection of production methods are described here.

Desolvation in this context refers to removal of aqueous solvent from the protein by combining the protein solution with a solvent which is miscible with water, but in which the protein is not soluble. This results in the precipitation of the protein at some critical solvent-water ratio. A typical strategy is to dilute the protein solution with solvent or add the protein solution dropwise to the solvent solution. In the case of silk fibroin, this may be applied by injecting fibroin into an acetone solution with recovery by dialysis yielding particles of ~42 nm

[135], while adding silk dropwise to acetone with centrifugation and resuspension by sonication yielded particles of ~100 nm [152, 153]. Fibroin particles formed with DMSO yielded particles of ~177 nm for *B. mori* silk and ~157 nm for *Antheraea mylitta* [155]. In one study, microfluidic technology was used to control the mixing process, yielding particles from 110-310 nm with acetone or isopropanol depending on the mixing conditions [156].

Salting out of silk proteins predominantly makes use of highly concentrated potassium phosphate. Depending on the volume ratio of salt to silk solutions and protein concentration, silk fibroin gave particles between 486 nm and 2 μm [165], clearly leading to much larger particles than those produced by desolvation. The engineered dragline silk protein eADF4(C16) forms particles of ~332 nm with a 10:1 volume ratio of salt to protein (1 mg/ml) solutions [166], or 1-2 μm using a 1:1 ratio (2.4 mg/mL) [162]. Other engineered dragline silk proteins MS1 and MS2 form particles from 667-1167 nm and 490-950 nm respectively, depending on production parameters [167].

Microdot printing can form silk fibroin particles through deposition of independent droplets from a micro capillary onto a colleting surface and air drying. Dried particles are then collected and soaked with methanol to convert the protein to a silk II conformation. Particles can then be lyophilised. In one study, this method resulted in silk fibroin particles of ~98 nm and ~45 nm at 0.1% and 10% fibroin concentration, respectively [154].

Spray-drying and spray-freeze-drying methods force the silk solution through a small opening under pressure with aspiration at high temperature for spray-drying and into liquid nitrogen for freeze-drying. This method can form silk fibroin particles up to 5 μm with high porosity, suitable for application as an inhaled powder [134]. Electrospraying can be used to form silk nanoparticles by forcing silk solution through a syringe by high voltage with direct collection into liquid nitrogen and lyophilization. This method can produce dry nanoparticle of 98 to 108 nm depending on parameters, with narrow size distribution [168].

Particles can also be produced from the sonication of dried silk films. In one study a combination of silk fibroin and PVA (poly-vinyl alcohol) was dried to form films which were then sonicated resulting in particles capable of loading small molecules. Particle sizes had wide distributions ranging from 100 nm to 5 μm depending on the initial silk-PVA concentrations and sonication amplitude [169].

A cryo-granulation technique was developed to form particles by injection of silk solution into a freezing solution of solvent. In one example, silk gellated by acetone or PEG-400 was injected into cold hexane under pressure, forming frozen droplets of large 200-900 μm size particles with 0.1-10 μm sized pores [170]. Electrospray methods use a voltage to generate a spray of silk containing droplets from the end of a nozzle, resulting in silk fibroin particles less than 100 nm [168] and 984 nm to 1270 nm fibroin-PVA hybrid particles[171].

In summary, a variety of particle production schemes with optimizable parameters are available which allow production of nano- and micro-scale drug delivery platforms. Different production methods produce particles with varying size and porosity. Desolvation, electrospray, and microdot printing are best suited for small nanoparticles less than 200 nm. Salting out can produce larger nanoparticles and small microparticles, while spray-drying, film sonication, and cryo-granulation can produce larger microparticles with high porosity.

1.5.4 Factors Affecting Physical Properties of Nanoparticles

Nanoparticle properties can be modified by altering the protein composition. In one example, the engineered dragline silk protein MS2 was modified by a glutamate substitution, resulting in larger particles with increased aggregation and surface charge. [146] Similarly, the engineered dragline silk protein eADF4(C16) was modified by glutamate to lysine substitutions, forming eADF4(κ16) which yielded slightly larger particles with positive rather than negative charge [161]. Hybrid particles of eADF4(C16) and eADF4(κ16) were significantly larger with a broader distribution [161]. In another case, hybrid particle of MS1 and MS2 showed smaller size and better stability [172]. Protein crosslinking prior to nanoparticle formation can change the properties of silk particles, greatly increasing their size and porosity as shown for silk fibroin [134]. Interestingly, variation in protein purification method may alter the composition of the protein solution enough to change particle formation. For an engineered dragline silk MS2(9x), protein purified by an acidic extraction method formed nanoparticles 35% larger and more porous than those formed by protein purified using a thermal extraction method [173]. The incorporation of drug molecules into nanoparticles can occur con-currently with particle formation, affecting particle properties such as surface charge [166] and likely size or other physical characteristics.

The main method of controlling nanoparticle properties is by modifying the precipitating solution and mixing method. For desolvation and salt precipitation, the solvent or salt concentration has a signification effect on the outcome. In one study, silk fibroin particles formed by desolvation had a significantly smaller size and polydispersity with a solvent ratio of 3:1 or 5:1 than with 1:1 for both acetone and isopropanol, with one exception [156]. Similarly, eADF4(C16) particles formed in 2 M potassium phosphate were much smaller when mixed with protein solution at a 10:1 ratio [166] than at a 1:1 ratio [162]. A higher solvent ratio also resulted in a higher surface charge, and increasing the mixing rate resulted in larger particles and higher poly-dispersity in most cases [156]. Mixing rates are typically not well controlled, with most preparations making use of pipetting, which can contribute to variability. One study analysed the effect of potassium phosphate concentration, pH, and protein concentration on nanoparticle size and morphology [167]. It was observed for MS1 and MS2 that increased salt concentration resulted in smaller, more defined particles. Changing the pH from 4 to 10 caused little change for MS2 particles, however for MS1 only a pH of 10 yielded defined spherical particles [167]. For silk fibroin, pH 4 yielded aggregated particles, while pH 5 and 6 yielded defined and larger spherical particles [165]. There was a large increase in particle size by several hundred nanometres by with increased protein concentration from 0.5-5 mg/mL for MS2 and MS1 [167], and from 0.25-20 mg/mL for silk fibroin [165]. In contrast, the desolvation of silk fibroin by acetone gave ~42 nm particles with 30 mg/mL [135] and ~98 nm with 5 mg/mL [152] protein concentrations, though the solvent concentrations varied between the two studies. In general, it appears that protein concentration has a more significant effect for methods based on salting out than those based on desolvation.

In one study, the morphology of particles could be controlled in a surprisingly direct way. Particles were produced by sonicating dried silk-PVA blend films. Films that were stretched yielded elongated particles compared to spherical particle from unstretched films [169]. PVA has also been used to control the size distribution of silk fibroin particles formed by desolvation [174]. Silk-ethanol solutions were mixed with PVA solutions and lyophilized, yielding nanoparticles with much more spherical morphology and much less aggregation than those without PVA [174]. The authors theorized that the PVA forms a porous matrix when flash frozen, constraining the silk nanoparticles.

For lyophilization procedures, the choice of cryoprotectant can be important. In one study trehalose resulted in grossly aggregated silk fibroin particles compared to mannitol [134]. Trehalose is a disaccharide and mannitol is a sugar alcohol. Both may stabilize the protein nanoparticles by hydrogen bonding via their hydroxyl groups. It is not clear why mannitol worked better as a cryoprotectant in this example or whether the effectiveness of various cryoprotectants depends on the protein composition of the nanoparticles.

In the case of electrosprayed silks, the voltage used may can affect particle sizes. A higher voltage can result in smaller sized particles due to smaller droplets formed from the needle [168, 171]; however, excessive voltage can result in larger particles due to instability of the flow [168]. The distance from the needle to deposition surface can affect the particle morphology, where this distance being too close results in aggregated particles as the droplets are not as well dispersed [175].

Particle stability can be controlled by modifying serveral aspects of the production process. For example, silk fibroin particles formed at pH 7 were less chemically stable (resistant to denaturants) than those formed at pH 9. This was correlated with a greater silk II composition at lower pH [165]. As an alternative approach, PEGylation of silk fibroin nanoparticles has been shown to prevent time-dependent aggregation in phosphate-buffered saline (PBS) [55].

1.5.5 Factors Affecting Drug Uptake and Release by Nanoparticles

Drug incorporation can occur concurrently with particle formation by incorporating the drug into the protein solution (pre-loading), or after particle formation by diffusion and adhesion (post-loading). For pre-loaded particles, it is likely that drug molecules which are insoluble in the particle-inducing solution would have higher loading efficiency due to co-precipitation. Dragline silk-based MS1 spheres had greater loading of the chemotherapeutic etoposide when pre-loaded while MS2 particles had greater loading of etoposide when post-loaded. However, both MS1 and MS2 particles had greater drug release when pre-loaded than when post-loaded [167]. This suggests that incorporating the drug molecule during particle formation altered the particle structure in a way that increased drug release, possibly by incorporation in-between the silk proteins resulting in looser packing.

Components with cationic or anionic charge and hydrophobicity in drug molecules can interact with the charged and hydrophobic features of nanoparticles, affecting drug uptake and

release, so mutations to the protein sequence can be used to optimise drug loading and delivery properties. Modified MS2 particles with a glutamate substitution (EMS2) showed greater loading and less release of etoposide, and greater loading and greater release of mitoxantrone compared to MS2 particles [146]. Interestingly, the pre-loading of etoposide by EMS2 showed much greater loading efficiency than post-loading, but the reverse was true for the loading of mitoxantrone [146]. In another example, anionic eADF4(C16) nanoparticles have high drug encapsulation efficiency for cationic drugs, and poor efficiency for anionic drugs [166]. However, when converted by lysine substitutions to cationic eADF4(κ16), particles were able to load anionic nucleic acids [162].

Release of drug molecules depends on the properties of the solution in which the particles are suspended, such as salt content and pH. In one study, eADF4(C16) particles were loaded with crystal violet or acridine orange. Crystal violet showed greater release in the presence of potassium chloride than sodium chloride, with the reverse relationship for acridine orange, while both show improved release at intermediate concentrations of potassium phosphate [162]. Dragline silk-based MS1 and MS2 particles showed significantly increased drug release rates at lower pH. Interestingly, the MS2 spheres pre-loaded with mitoxantrone showed significantly less pH sensitivity than post-loaded particles, while MS1 and MS2 particles pre- or post-loaded with etoposide showed similar pH sensitivity. [167]

1.6 Theory of Experimental Techniques

1.6.1 Fluorescence

Photon absorption can excite electrons of a molecule from the ground electronic state to a higher, energy excited state if the photon energy matches the energy difference between those two quantized states [176, 177]. Excited electrons rapidly lose energy through vibrational relaxation and internal conversion mechanisms to the lowest singlet excited energy level prior to a slower process of emission. Emission returns the excited electron to the ground state through the release of a photon which is longer in wavelength than the absorbed photon due to the aforementioned loss of energy. This difference in wavelength is termed the Stokes shift [177]. The relaxation process can be described by radiaptive (emission) and non-radiative decay mechanisms using Eq. 13 [177].

$$\frac{dN}{dt} = -(\Gamma + k)N \quad (13)$$

where N is the fraction of excited fluorophore, t is time, Γ is the radiative decay rate and k is the non-radiative decay rate. This decay process may also be described in terms of a fluorescence lifetime, τ using Eq. 14 [177]:

$$\tau = \frac{1}{\Gamma+k} \quad (14)$$

The number of electrons relaxed by each decay mechanism is the integral of decay rate over a given time period, so the quantum yield can be described using Eq. 15 [177]:

$$\Phi_F = \frac{\Gamma}{\Gamma+k} \quad (15)$$

where Φ_F is the fluorescence quantum yield. The intensity of fluorescence emission is related to the extinction coefficient and quantum yield of a particular molecule using Eq. 16 [178]:

$$F = 2.3 I_0 \varepsilon_{(\lambda ex)} c l \Phi_F \quad (16)$$

where F is the fluorescence intensity, I_0 is intensity of incident light, $\varepsilon_{(\lambda ex)}$ is the extinction coefficient at the wavelength λ_{ex}, c is the fluorophore concentration, *l* is the sample path length.

Intermolecular interactions can result in fluorescence quenching by providing additional sources of non-radioactive decay either by forming a complex with the fluorophore or by random collision, processes termed static and collisional quenching, respectively [177]. These differ in that static quenching reduces the number of fluorescing molecules, and collisional quenching competes with emission by increasing the rate of non-radiative decay which also decreases the fluorescence lifetime [177]. The effect upon fluorescence may be expressed for static quenching using Eq. 17:

$$\frac{F_0}{F} = 1 + K_a[Q] \quad (17)$$

and for collisional quenching using Eq. 18:

$$\frac{F_0}{F} = 1 + k_0 \tau_0 [Q] \quad (18)$$

respectively, where F_0 and F are the fluorescence intensity without and with quenching, k_0 is the rate of collision, τ_0 is the lifetime in the absence of quenching, K_a is the binding constant for the quenching complex, and [Q] is the concentration of the quencher.

Aromatic residues of proteins can fluoresce due to excitation of electrons in their π-orbital systems [179]. Of the three aromatic amino acids phenylalanine, tyrosine, and tryptophan, the latter can be selectively excited above 295 nm [180]. Tryptophan fluorescence is

also particularly sensitive to the polarity of its environment [179] due to the large dipole moment of the excited state [181].

Sensitivity to solvent polarity is mediated by interactions between the tryptophan dipole and solvent dipole, which provides an additional source of energetic stabilization to the excited state [179, 182]. As a result, the emission wavelength is longer in more polar – and stabilizing – solvents due to a correspondingly decreased energy difference between excited and ground states. Tryptophan emission maxima range from ~309 nm in a highly shielded, and therefore hydrophobic, protein interior, to ~355 nm in water [92, 183]. Since conformational changes of proteins may change the solvent exposure of tryptophan and other residues, changes to the emission maximum can be reflective of changes to the protein conformation [92].

The fluorophore pyrene has a more complex emission spectrum than tryptophan, with five main maxima (termed emission bands) which are I_1: 372.5 nm, I_2: 379 nm, I_3: 383 nm, I_4: 388.5 nm, and I_5: 393 nm [99]. The intensity ratio I_1/I_3 decreases characteristically along with the solvent polarity of its surroundings [99]. This ratio, thus, provides a sensitive probe of the degree of shielding of the pyrene molecule under a given condition. Partitioning of pyrene into a micelle or its surface binding to proteins can therefore be tracked with the I_1/I_3 ratio [98, 99].

The emission spectrum of tryptophan [180] overlaps with the excitation spectrum of pyrene [98]. This allows for Förster resonance energy transfer (FRET) from excited tryptophan molecules - acting as donors - to pyrene acceptor molecules [184]. FRET occurs due to the transfer of energy between donor and acceptor fluorophores as a non-radiative decay process when the two molecules are within a characteristic distance of one another (typically up to ~10 nm). The transfer efficiency is very sensitive to distance and can be used to characterize binding events and conformational changes [185]. The rate of FRET is described by Eq. 19 [184, 185]:

$$k_T = \frac{1}{\tau_D} * \left(\frac{R_0}{R}\right)^6 \tag{19}$$

where k_T is rate constant of donor to acceptor transfer, τ_D is the fluorescence lifetime of the donor in the absence of acceptor, R_0 is the intermolecular donor-acceptor distance at which transfer is 50% (termed the Förster distance), and R is the actual donor-acceptor intermolecular distance. The intermolecular distance can be calculated from measurements of the FRET efficiency (E) by fluorescence life times or intensities using Eq. 20 [184, 185]:

$$E = 1 - \frac{\tau_{DA}}{\tau_D} = 1 - \frac{I_{DA}}{I_D} = \frac{1}{1+\left(\frac{R}{R_0}\right)^6} \tag{20}$$

where τ_D and I_D are the donor lifetime and intensity without acceptor, respectively, and τ_{DA} and I_{DA} are the donor lifetime and intensity with acceptor, respectively.

1.6.2 Circular Dichroism

Chiral molecules interact with light in an asymmetric manner resulting in the differential absorbance of left and right circularly polarized light. Circular dichroism (CD) is specifically defined as the resulting difference between the extinction coefficients for left and right circularly polarized light of a chromophore. This difference in absorbance may be described as degrees of ellipticity using Eq. 21 [186]:

$$\Theta_\lambda = 32.98(A_L - A_R) \quad (21)$$

where Θ_λ is the ellipticity at a particular wavelength and A_L and A_R are the absorbance of left and right circularly polarized light, respectively, at that wavelength. This is generally normalized by molecular concentration (c) and path length (l) to molar ellipticity using Eq. 22:

$$[\Theta] = \frac{100\Theta}{lc} \quad (22)$$

In many instances, a further normalization factor of number of residues (n) is applied, giving mean residue ellipticity by Eq. 23.

$$[\Theta] = \frac{100\Theta}{lcn} \quad (23)$$

The peptide bond is optically active and its circular dichroism in the UV region of ~180 to 250 nm is sensitive to polypeptide secondary structure [186, 187]. This allows far-UV CD spectroscopy to be applied to obtain information about protein conformation and conformational changes. The CD spectrum of a protein arises from the sum of contributions from all optically active secondary structures. α-Helical structures possess a large positive band at ~190 nm and two negative bands at ~208 and 222 nm; anti-parallel β-sheets a positive band at ~195 nm and a single negative band at ~ 217 nm [188]. Other structural units, such as β-turns, poly-Pro-II helices, and random coil, have characteristic spectral shapes as shown in Figure 7.

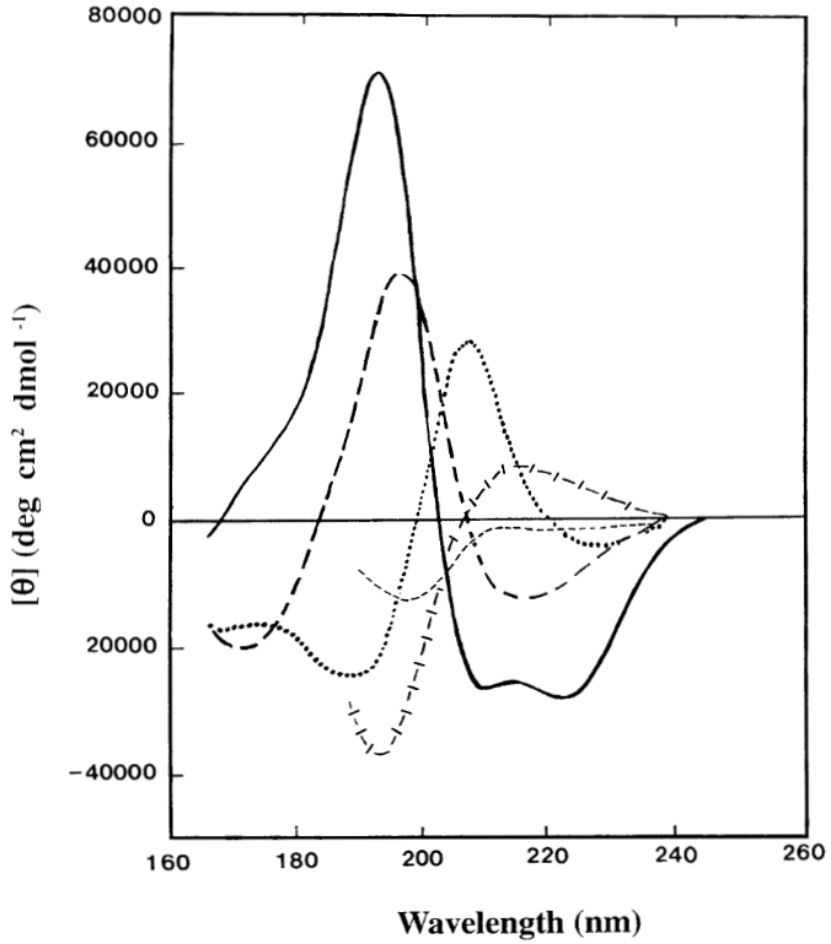

Figure 7: Characteristic CD-spectra of protein secondary structures. α-helix (solid line), anti-parallel β-sheet (long dashed line), type I β-turn (dotted line), poly-Pro II helix (cross dashed line) and random coil (short dashed line). Reproduced from Kelly et al. [188]

1.6.3 Dynamic Light Scattering

Light scattering by colloidal particles in solution was first reported by Tyndall [189]. Scattering of light by particles smaller than the wavelength is described by Rayleigh scattering [190, 191] and by particles larger than the wavelength by Mie scattering [192]. Dynamic light scattering (DLS) techniques involve shining a laser light through a sample solution and measuring the subsequent fluctuations in light scattering intensity at an angle from the incident beam as a function of time [193]. Scattered photons and the interference between them result in light intensity observed by the detector changing over time due to particle diffusion. The diffusion and collision of particles by Brownian motion refers to the random motion of a suspended particle in its medium due to the thermal kinetics of the medium rather than a directional current or applied force [194, 195]. This motion results in time-dependent fluctuation of scattered light intensity at the detector, which can be analyzed to determine diffusion coefficient(s), particle size(s), and degree of polydispersity in a given sample [193]. For more in depth reference, a review of the development of DLS techniques is available [196].

Brownian motion may be described by the Stokes-Einstein equation (Eq. 25) [197]:

$$D_T = \frac{k_B T}{6\pi\eta r} \tag{25}$$

where D_T is the translational diffusion coefficient, k_B is the Boltzmann constant, T is the absolute temperature, η is the solution viscosity, and r is the hydrodynamic radius of the diffusing molecule, under the assumption of a spherical shape. The motion of particles relative to one another is described by the normalized electric field correlation function $g_1(\tau)$ (Eq. 26) [196, 198]:

$$g_1(\tau) = \frac{\langle E(t)E(t+\tau)\rangle}{\langle E(t)E(t)\rangle} \tag{26}$$

where E(t) is the intensity at time t and E(t+τ) the intensity after a delay time τ. The relative motions of particles results in scattering intensity fluctuations described by the measured intensity correlation function $g_2(\tau)$ (Eq. 27) [196, 198]:

$$g_2(\tau) = \frac{\langle I(t)I(t+\tau)\rangle}{\langle I(t)\rangle^2} \tag{27}$$

Brownian motion of the scattering species results in exponential decay of the correlation function and is described using Eq. 28:

$$g_1(\tau) = e^{-\Gamma\tau} \tag{28}$$

where Γ is the decay constant described below. Realistically, the observed correlation function arises from a sum of multiple decays representing each size of particle in a polydisperse sample, described by Eq. 29:

$$\Gamma = -D_T q^2 \tag{29}$$

where q is the Bragg wave vector, described by Eq. 30 [199]:

$$q = \frac{4\pi n}{\lambda}\sin(0.5\theta) \tag{30}$$

where n is the refractive index of the solvent, λ is the wavelength of the scattering light, and θ is the angle from the incident light to the detector.

The scattering intensity correlation is related to the relative molecular motion by Eq. 31 [196, 200]:

$$g_2(\tau) = B + \beta|g_1(\tau)|^2 \tag{31}$$

where B is the baseline intensity and β is the coherence factor, a constant related to the detector of the instrument. Combing Eq. 28, 29 and 31 gives Eq. 32:

$$g_2(\tau) = B + \beta e^{-2D_T q^2 \tau} \tag{32}$$

Based on these equations, light scattering is affected by the solvent viscosity and refractive index; the wavelength of the laser; and, the angle of detection. Several models are available to fit the decay of the correlation function and calculate the size distribution of the scattering particles. The cumulants method [201] is commonly applied to samples of particles which have a monomodal Gaussian distribution. Cumulants analysis makes use of a Taylor expansion to fit several parameters, described by Eq. 33:

$$\ln(g_2(\tau) - B) = \ln\beta + 2\left(-\bar{\Gamma}\tau + \frac{k_2}{2!}\tau^2 - \frac{k_3}{3!}\tau^3 + \frac{k_4}{4!}\tau^4 \ldots\right) \tag{33}$$

where $\bar{\Gamma}$ fits the mean, k_2 the variance (width), k_3 the skew (lopsidedness) of the distribution, and k_4 the kurtosis (number of outliers). Other methods must be employed for samples which deviate from a Gaussian distribution due to multiple scattering species or large polydispersity.

One common method for DLS fitting is the non-negative least squares (NNLS) method [196, 202], which takes the Laplace transform of the integral of equation 28 with respect to the decay constant Γ. This results in the following fitting equation (Eq. 34):

$$X^2 = \sum_{j=1}^{N}\left[g_1(\tau_j) - \sum_{i=1}^{M} b_i e^{(-\Gamma_i \tau_j)}\right]^2 \tag{34}$$

where N and M are the number of data points and decay constants, respectively, and b_i are coefficients set to fit the equation to the data. Because NNLS fits all data points equally, the fit

is easily skewed by outliers, errors and noise. Another common model CONTIN is similar to NNLS, but includes regularization constraints which are adjustable depending on the expected nature of the size distribution [203]. The CONTIN fit is described by Eq. 35:

$$X^2 = \sum_{j=1}^{N} \frac{1}{\sigma_i^2} \left[g_1(\tau_j) - \int G(\Gamma) e^{(-\Gamma\tau)} \right]^2 + \alpha^2 \|LG(\Gamma)\|^2 \quad (35)$$

where α is the regularization parameter, L is the regularizer operator, and σ is the variance. Essentially, the regularization in CONTIN rejects data that is outlying to the expected fitting model as set by the regularization parameter based on an F-test, and so it is less sensitive to noise and outliers [203, 204]. However, the selection of the parameters is somewhat arbitrary and without an estimate of the expected size distribution CONTIN parameters are generally set to generate the simplest fit to the data. This results in narrow distributions and possible blending together of multiple real size distributions which are closely spaced [203, 204].

1.6.4 Surface Tension

Surface tension and surface assembly of surfactants was described in detail in Section 1.4.2. Surface tension measurements were conducted using the Wilhelmy plate technique [205, 206]. A wettable plate is suspended into the solution by a rigid support connected to a tensiometer. The pressure exerted on the plate by the solution counteracts the force of gravity resulting in a decrease of the pressure reading. An increase in surface tension results in greater upward pressure from the solution on the plate and decreased pressure reading [205, 206].

1.6.5 Scanning Electron Microscopy

To produce an image by scanning electron microscopy an electron beam is passed over the surface of the sample at an angle. Scattering of incident electrons from the sample surface is dependent on the surface topology [207, 208]. The scattering signals are correlated to the positions of the incident electron beam on the sample and typically processed by digital image correlation in modern instruments [209]. Non-conductive samples are typically coated with metal particles to increase electron density and reduce build up of charge on the sample [207, 210].

1.7 Research Intentions

Spider silks have different mechanical and chemical properties [51], meaning that different silks may be preferable for different applications. Aciniform silks have greater toughness compared to other silk proteins and are not as well studied as dragline or silkworm silks. Additionally, the conditions within the aciniform gland are not known, and models of the silk spinning process are based on dragline silk which is produced in a gland with a much different morphology than the aciniform gland (Figure 1) [6]. Therefore, it is of interest to study the pathway of aciniform fibrillogenesis. First, this requires the stable storage of the soluble silk protein at a high concentration. Understanding and improving this storage state may in turn, help to elaborate early stages of the spinning process of this silk protein which may be applied to improve artificial silk spinning methods.

Surface adsorption and assembly of proteins at the liquid-air interface is generally associated with a conformational transition toward β-sheet, exposing hydrophobic protein surfaces to the air surface, as described in Section 1.4.2. For silk proteins, this can result in the formation of a viscoelastic surface film, with the adsorbed proteins remaining in a soluble state [118-120]. As well, recombinant AcSp1 can be hand-drawn from the surface of silk solutions [82]. Therefore, the conformation of silk proteins adsorbed at the hydrophobic liquid-air interface may reflect how the proteins interact with the hydrophobic surfaces of other silk proteins when aligned in the spinning duct. Conformational transitions and alignment of silk proteins in a surface film may reflect those that occur during the early stages of fibre formation, and may help to understand the fibrillogenic pathway. The adsorption of W_1 to the liquid-air interface is investigated in this study, forming the basis of Chapter 2.

There is some evidence that W_1 forms micelle-like nanoparticles in solution [91] and, because it cannot form fibres [82], W_1 could be used more easily to investigate the protein conformation and arrangement in the micellar state under conditions leading up to fibre formation, with its inability to form fibres potentially locking the self-assembled proteins in a pre-fibril state. In this study, the micelle-like self assembly of recombinant AcSp1 W_1 protein (Section 1.3.1) is investigated as detailed in Chapter 3.

Protein nanoparticles may have different drug compatibility, and kinetics of drug uptake and release, depending on the choice of protein or mutations made to the protein, as described in Section 1.5.5. Aciniform silk-based nanoparticles have not yet been investigated and, therefore,

have unknown compatibility and potential advantages over other silk protein nanoparticles, or suitability for particular applications. In this study a methodology was developed to produce W_1 nanoparticles, as detailed in Chapter 3. The size and morphology of particles, as well as the conformation of the proteins within the particles were investigated in order to establish the potential of aciniform silk as a drug delivery vehicle.

Chapter 2: Solution-State Assembly of Recombinant Aciniform Proteins

2.1 Overview

Solution-state assembly refers to the reversible formation of micelle-like nanoparticles and adsorption at the liquid-air interface by the W_1 protein. There is evidence that W_1 assembles into micelle-like nanoparticles with an estimated CMC of ~20 μM [91], and these assemblies of W_1 were investigated further in this study. Other silk proteins show adsorption at the liquid-air interface associated with conformational changes [118-120], but adsorption of aciniform silk has not yet been investigated.

Studying the micelle forming behaviour of W_1 may help to understand the role of micellar assemblies that possibly form within the aciniform gland in terms of both storage and fibrillogenesis of aciniform silk proteins at high concentrations. If micelle formation is a part of the fibrillogenesis pathway then conformational changes of the W_1 protein due to micellization, and the orientation of proteins within micelles, may help to understand the conformational changes and the process of protein alignment that occurs during fibrillogenesis.

The alignment of AcSp1 proteins at the liquid-air interface may also be similar to the parallel alignment of the silk proteins as they move down the spinning duct [75]. Adsorption of silk fibroin and dragline silk proteins results in an increase in β-sheet, and the formation of a visco-elastic surface layer[118, 120]. Therefore, studying the arrangement and conformation of silk proteins at the liquid-air interface may give clues as to the structure of aligned β-sheets in the spinning duct.

Several methods were utilized to study solution-state assembly of W_1. Tryptophan substituted variants of W_1 were used to probe the relative solvent exposure at several sites within the protein, which may change if a particular surface of the protein is buried within the micelle interior, or if conformational changes occur that change the solvent exposure of that tryptophan residue. DLS and pyrene fluorescence were used to detect the presence of W_1 micelles, and fluorescence quenching of the R36W tryptophan residue in the presence of pyrene was used to probe the location of surface binding of pyrene to W_1. Surface assembly of W_1 was tracked by the decrease in surface tension induced by the adsorption of proteins at the liquid-air interface.

2.2 Materials and Methods

2.2.1 Recombinant Expression and Purification of W_1 Proteins

W_1 proteins were recombinantly expressed and purified as previously described [82]. Briefly, the construct protein sequence below (Figure 8) had been previously expressed from pEHU plasmids (Novagen, Darmstadt, Germany), with the N-terminal serine of the W_1 sequence removed for cloning purposes.

MGHHHHHHGSDSEVNQEAKPEVKPEVKPETHINLKVSDGSSEIFFKIKKTTPLRRL
MEAFAKRQGKEMDSLRFLYDGIRIQADQTPEDLDMEDNDIIEAHREQIGGAGPQGG
FGATGGASAGLISRVANALANTSTLRTVLRTGVSQQIASSVVQRAAQSLASTLGVDGNN
LARFAVQAVSRLPAGSDTSAYAQAFSSALFNAGVLNASNIDTLGSRVLSALLNGVSSAA
QGLGINVDSGSVQSDISSSSSFLSTSSSSASYSQASASSTSGAGYTGPSGPSTGPSGYPGPL
GGGAPFGQSGFGG

Figure 8: The sequence of recombinantly expressed W_1 proteins. The His_6-SUMO tag is in boldface and the tryptophan substitution sites are highlighted for R36W, F90W, F146W, and Y169W

Each W_1 construct was expressed in BL21 (DE3) *Escherichia coli* in lysogeny broth (LB) medium with ampicillin selection (50 µg/mL) at 37 °C to an OD_{600} of 0.8 to 1.2. Expression was then induced by addition of 0.8 mM IPTG with incubation at ~20 °C overnight. Cells were harvested by centrifugation at 5000×g at 4 °C for 15 min. Pelleted cells were resuspended in lysis buffer (10 mM Tris-HCl, 300 mM NaCl, 20 mM imidazole, pH 8.0) and lysed using a French Pressure Cell (American Instrument Company). The lysate was centrifuged at 25,000xg for 60 min at 4 °C to remove cellular debris.

Each W_1 protein was purified by column chromatography on a Ni-NTA Sepharose resin (Qiagen, Germany). His_6-SUMO tagged W_1 bound to the column was then washed with buffer (10 mM Tris-HCl, 300 mM NaCl, 50 mM imidazole, pH 8.0) and then eluted from the column (10 mM Tris-HCl, 300 mM NaCl, 250 mM imidazole, pH 8.0). Eluted His_6-SUMO-W_1 was dialysed against 10 mM Tris-HCl (pH 8.0) with concurrent removal of the His_6-SUMO tag by SUMO protease (produced in our lab) at a protease-protein ratio of 1:100 at 4 °C overnight. The

dialysed protein was then purified using reverse affinity column chromatograph. Specifically, using Ni-NTA resin, cleaved His_6-SUMO, uncleaved W_1 protein, and SUMO protease remain bound, with the column flow through containing purified W_1. W_1 concentrations were measured by absorbance at 210 nm with an estimated [83] extinction coefficient of 270858 $M^{-1} \cdot cm^{-1}$.

2.2.2 Fluorescence

All emission spectroscopy measurements were performed in triplicate, with each replicate being the average of 3 scans. Experiments were carried out using a Cary Eclipse spectrofluorometer (Varian, Palo Alto, CA, US) using a 1-cm quartz cuvette (Varian, Palo Alto, CA, US).

To examine the dependence of tryptophan fluorescence R36W, F146W and Y169W variants of W_1 on the concentration of W_1, emission was measured over 310 to 370 nm (slit width: 2.5 nm) with excitation at 298 nm (slit width 5 nm), an averaging time of 1 s, with a 0.5-nm interval at 25 °C. Samples were prepared at 50 μM W_1 in 50 mM potassium phosphate buffer (pH 7.5) and diluted in series to 40, 30, 20, and 10 μM by pipetting. W_1 at 50 μM in sodium acetate buffer (pH 5.0) was measured using the same parameters. As a control for a fully solvent exposed tryptophan, a heptapeptide (PGPWQGG), derived from the protein apelin-55 [211], was measured at 100 μM in 50 mM potassium phosphate buffer (pH 7.5) with excitation at 295 nm, slit widths of 5 nm, averaging time of 0.5 s with a 1-nm interval.

Temperature denaturation and precipitation were measured in 50 mM potassium phosphate buffer (pH 7.5) at 50 μM W_1 with emission over 310 to 370 nm (slit width: 2.5 nm) with excitation at 298 nm (slit width 5 nm), an averaging time of 0.5 s, with a 1-nm interval. Samples were initially measured at 25 °C, re-measured at 90 °C for Y169W and F146W, or 65 °C for R36W, and then re-measured again after cooling to 25 °C. Samples were allowed to incubate for 10 min after each temperature change prior to spectroscopic measurement.

Pyrene fluorescence was measured with an excitation wavelength of 332 nm (slit width 5 nm for R36W and 10 nm for wt), and an emission wavelength range from 360 to 400 nm (slit width: 2.5 nm), averaging time of 1 s and 0.5-nm intervals at 25 °C. Samples were prepared by drying pyrene dissolved in acetone at the bottom of the cuvette and then adding a solution of 80 μM W_1 in 50 mM potassium phosphate buffer (pH 7.5) with a 30-min incubation, to a pyrene concentration of 0.1 μM. Samples were then diluted in series with buffer containing 0.1 μM

pyrene by gentle pipetting. The I_1 to I_3 ratio was calculated using the emission intensities at 372.5 and 383.5 nm, respectively.

FRET between tryptophan and pyrene was measured by observing quenching of tryptophan fluorescence. Specifically, fluorescence was measured with excitation at 298 nm (slit width: 5) and emission from 310 to 370 nm (slit width 2.5), averaging time of 1 s and 0.5-nm intervals at 25 °C. Samples were prepared by drying pyrene in acetone at the bottom of the cuvette before adding W_1 at 80 µM in 50 mM potassium phosphate buffer (pH 7.5), to an expected pyrene concentration of 10 µM, with a 30-min incubation. Fluorescence intensities were compared at 353.5 nm using equation 20. The R_0 distance for the tryptophan-pyrene pair is 2.8 nm [212].

2.2.3 Dynamic Light Scattering

DLS measurements were conducted using a BI-200SM instrument and analysed using the BI-ISTW software (Brookhaven Instruments, NY, USA), at 25 °C and an angle of 120° in a quartz cell (1 cm, Hellma Analytics, Markham, ON, CA) with a laser wavelength of 637 nm.

For measurements of the kinetics of micelle formation by W_1, a solution of 50 µM W_1 in 50 mM potassium phosphate buffer (pH 7.5) was filtered through a 0.02 µm syringe filter directly into the cell and measured within 30 min after filtration and again after 24 h at 4 ºC with ~1 h at 23 ºC. Samples were measured with an angle of 120º at 23 ºC using the BI-ISTW software reference values for the viscosity (0.924 cP) and refractive index (1.331) for water at 23 ºC . Data were fit by NNLS due to the expectation that the population of nanoparticles is very low compared to the monomer and may be viewed by the CONTIN fit as noise.

2.2.4 Surface Tension

A 1x2 cm piece of Whatmann No. 2 filter paper was suspended from a tensiometer into a dish containing ddH_2O and the pressure was set to zero after equilibration. The solution of water was replaced by the same volume of 50 mM potassium phosphate buffer (pH 7.5) and equilibrated until a stable pressure reading was observed. To add W_1 to the solution, the same volume of protein stock solution to be added was first removed to maintain constant volume and solution height relative to the plate. Protein solution was added by pipetting at the bottom of the dish while pipetting back 1 mL of buffer removed from dish at the same position to ensure rapid

mixing, to a concentration of 2.25 μM. The measurement of pressure with time was started just prior to mixing and the zero time point was set just after mixing, as by large pressure fluctuations. Data were normalized between 0 and 1 by Eq. 24 due to differences in the minimum and maximum pressure readings between samples:

$$\frac{Y-Y_{min}}{Y_{max}-Y_{min}} \quad (36)$$

and were then fit to the integral of the Langmuir isotherm (Eq. 9), which is given by Eq. 37, assuming a negligible value of k_d for a negligible rate of desorption.

$$\Gamma = \frac{tk_ac}{1+tk_ac+tk_d} \quad (37)$$

2.3 Micellization Experimental Results

2.3.1 Conformation and Micellization of Tryptophan Substituted AcSp1

The process of micellization involves the reorganization of protein monomers by adhesion of hydrophobic protein surfaces to form a solvent-excluded micelle interior, with hydrophilic protein surfaces exposed to the solvent at the micelle exterior [213]. Micellization, as a protein-protein interaction and sequestration event, may involve some degree of conformational change to the protein.

Based on the CMC of ~20 μM for wt W_1 inferred previously by pyrene and 1,8-ANS fluorescence [91], it would be expected that conformational transitions occurring due to micellization of W_1 would be observed at concentrations above 20 μM. Intrinsic tryptophan fluorescence of the Y169W, F146W, and R36W substituted W_1 proteins did not show a change in emission maxima between 10 and 50 μM at pH 7.5 (Figure 9) and no shouldering effect was observed (Figure 10). There are no tryptophan residues in the wild-type W_1. This indicates either that these residues are not buried within any micellar-like structures that are formed or that such structures are not formed in significant quantity with respect to the monomer concentration remaining in solution above the CMC. As would be expected from their positions within the W_1 structure (Figure 4), the Y169W and F146W variants have the longest emission maxima at 356.2 and 354.4 nm, respectively, reflecting the relatively high solvent exposure expected on the basis of their positions (Figure 9) [89]. For comparison, the emission maximum for the fully exposed tryptophan of the heptapeptide control (PGPWQGG) is at 358.7 ± 0.2 nm (Table 2).

The emission maximum of the residue R36W at 353.6 nm is comparable to that of the Y169W and F146W sites, which implies a similar solvent exposure. This contrasts with the exposure expected on the basis of prediction of only 4% solvent accessible surface area for the R36W residue, compared to 71% and 93% for F146W and Y169W, respectively [89]. No change in emission maxima was observed at pH 5.0 compared to pH 7.5 (Table 2 and Figure 11) for any of the W_1 variants, implying that no perturbations that are occurring due to acidification affect the environment of the tryptophan residues.

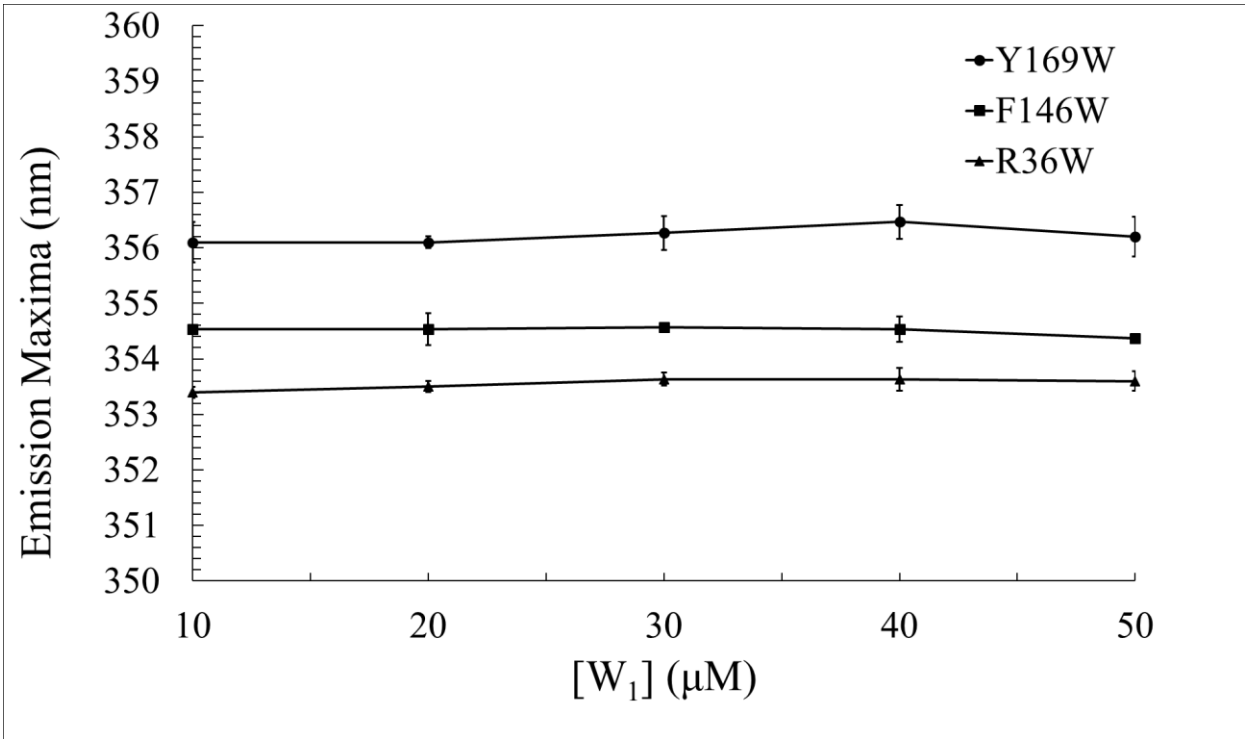

Figure 9: Intrinsic tryptophan fluorescence (λ_{ex} = 298 nm) of W_1 variants in 50 mM potassium phosphate buffer (pH 7.5) at different concentrations of W_1

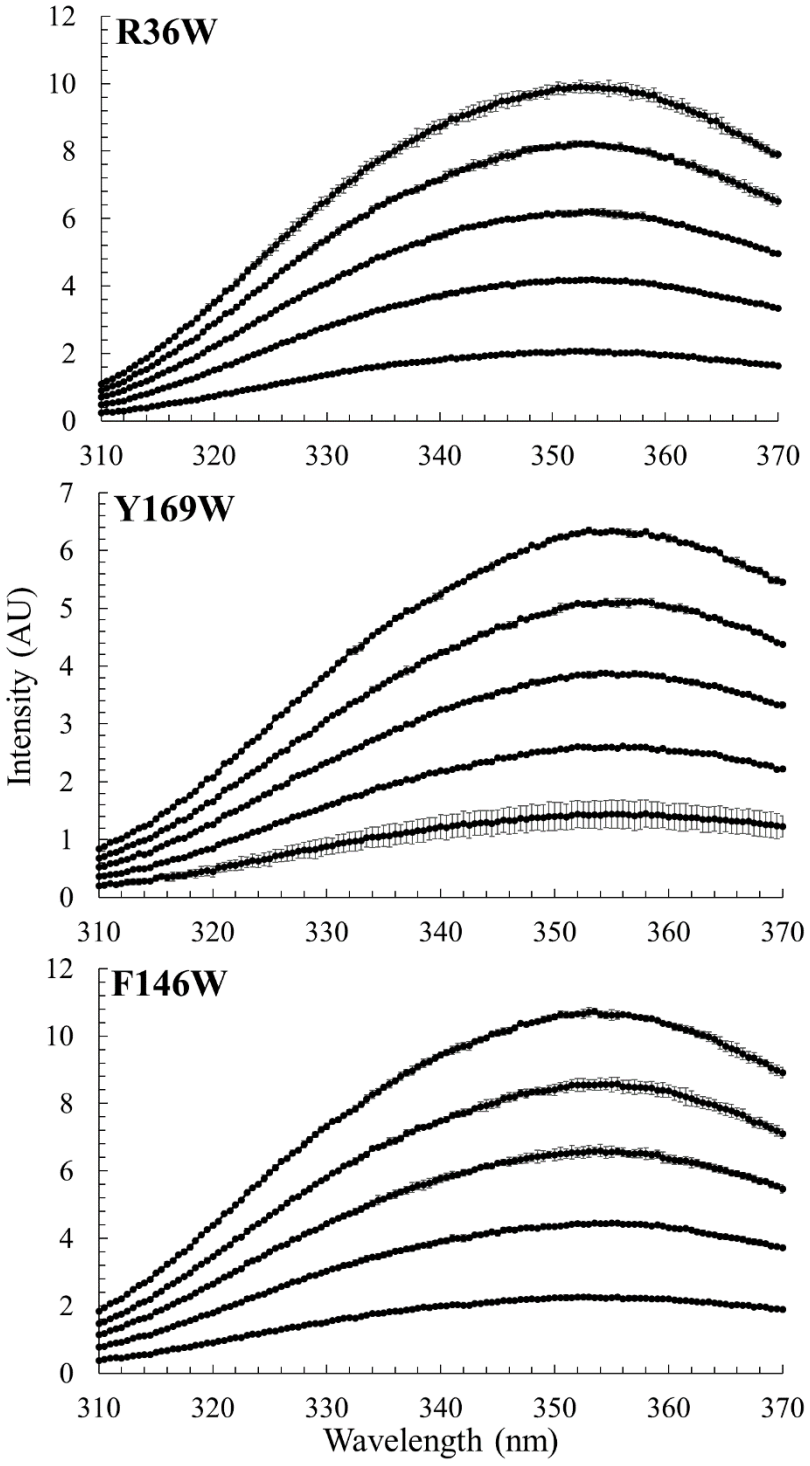

Figure 10: Intrinsic tryptophan fluorescence (λ_{ex} = 298 nm) of W_1 variants in 50 mM potassium phosphate buffer (pH 7.5) for dilutions of W_1 from 50 to 10 μM in order of top to bottom. Intensities are given in arbitrary units (AU)

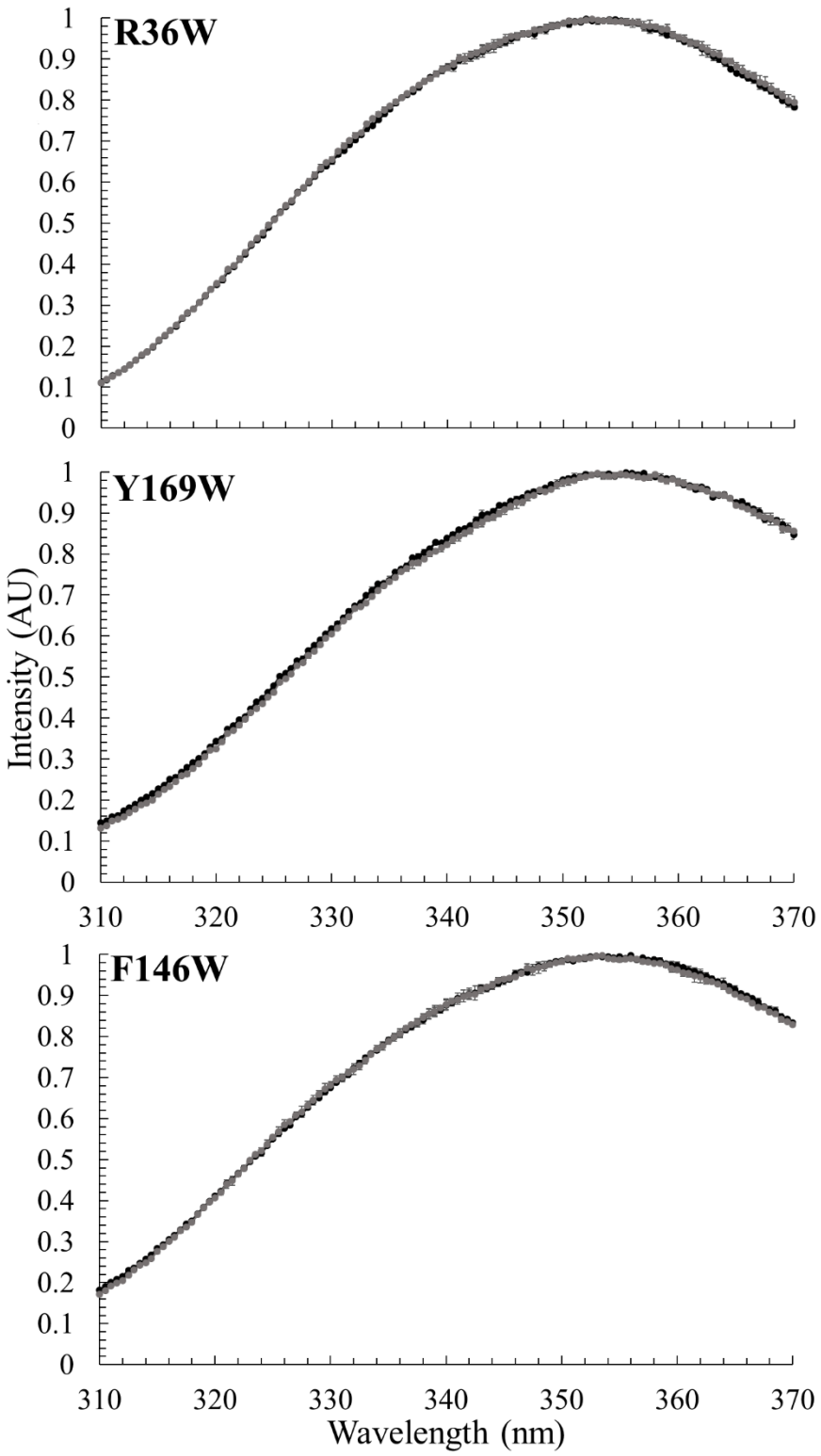

Figure 11: Intrinsic tryptophan fluorescence (λ_{ex} = 298 nm) of W_1 variants at 50 µM in 50 mM potassium phosphate buffer (pH 7.5, grey) and 20 mM sodium acetate buffer (pH 5.0, black). Intensities are given in arbitrary units (AU)

Table 2: Intrinsic tryptophan fluorescence (λ_{ex} = 298 nm) of W_1 variants and the heptapeptide control in 50 mM potassium phosphate (pH 7.5) and W_1 variants in 20 mM sodium acetate (pH 5.0) buffer. NA: not available

	Emission Maxima (nm)			
pH	**R36W**	**F146W**	**Y169W**	**Heptapeptide (PGPWQGG)**
7.5	353.6 ± 0.2	354.4 ± 0.1	356.2 ± 0.4	358.7 ± 0.2
5.0	353.6 ± 0.2	354.6 ± 0.1	356.0 ± 0.2	NA

The wild-type W_1 protein showed reversible thermal denaturation up to approximately 90 ºC in a previous study [91]. The F146W and Y169W variants, correspondingly, showed reversible denaturation at 90 ºC, with practically no change of their emission maxima (Figurre 12B and C) upon heating and after cooling. Qualitatively, there was no visible precipitation observed after incubation at 90 ºC. In contrast, the R36W variant showed clearly visible precipitation at 65 ºC, giving a hazy solution. The emission maximum of R36W showed a blue-shift upon heating, consistent with precipitation and concomitant sequestration away from the aqueous environment (Figure 12A). Interestingly, 65 ºC corresponds to the initiation of thermal denaturation by the wild-type W_1 as observed using circular dichroism spectropolarimetry [91], while chemical denaturation begins with disruption to helix 5 [89]. Assuming that thermal denaturation of W_1 also begins with helix 5, the early precipitation of the R36W variant may be due to exposure of the hydrophobic tryptophan residue located beneath helix 5.

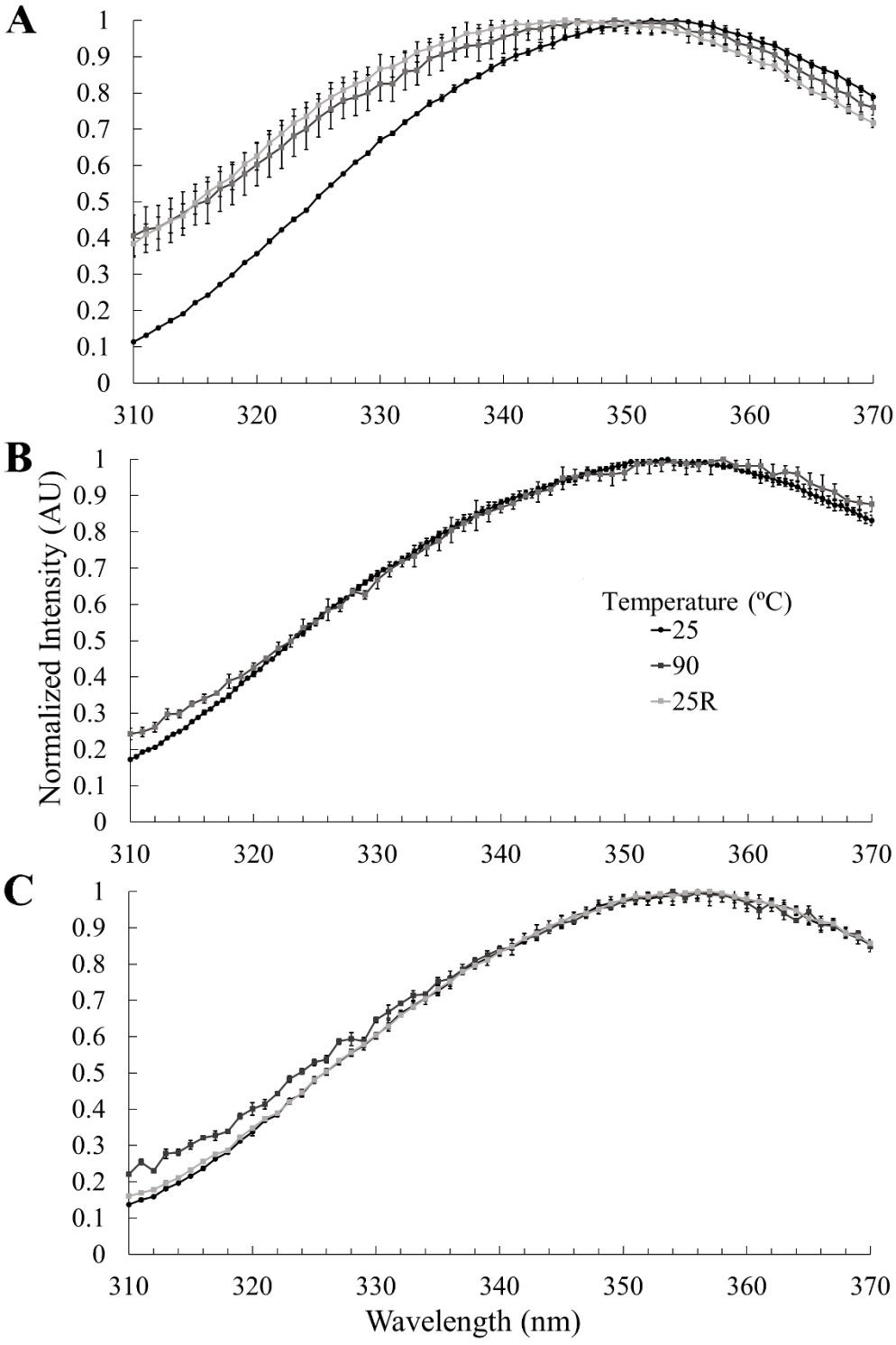

Figure 12: Intrinsic tryptophan fluorescence (λ_{ex} = 298 nm) of W_1 variants in 50 mM potassium phosphate buffer (pH 7.5) measured sequentially at 25 ºC, 90 ºC, and after cooling to 25 ºC (25R (return)), with 5 min incubation. R36W (A); F146W (B); Y169W (C). Intensities given in arbitrary units (AU)

Micellization of the R36W and wild-type W_1 variants was probed by pyrene fluorescence by following the same methodology as employed previously [91] to determine if the apparent increased hydrophobicity of the region below helix 5 implied by the red-shifted tryptophan emission maximum of the R36W variant is related to micelle-forming behaviour. A shorter incubation time of 30 min at room temperature was needed to avoid the precipitation of the less stable R36W variant that occurred with overnight incubation, while still allowing pyrene to dissolve into the solution. The contrasts with the previous experiment which used and incubation of 24 h at 4 °C and 1 h at room temperature [91]. However, the incubation time employed was 30 min at room temperature rather than 24 h at 4 °C and 1 h at room temperature. At ~80 μM, the I_1/I_3 ratios were ~1.57 and ~1.54 for the wild-type and R36W variants, respectively (Figure 14). This compares to ~1.15 for the wild-type with a 24 h incubation, after dilution to ~80 μM [91]. Without protein, the ratio was ~1.80 and ~1.85 for the wild-type and R36W variant relative to ~1.58 observed in the previous study [91]. The lower ratios for the previous study may be due to a difference in the wavelength selected for the I_3 peak, and a different spectral shape with the 5 characteristic vibrionic peaks of pyrene not being visibly defined as they were in this study (Figure 13). The source of this difference in the spectral shape is not clear. Both the R36W and the wild-type W_1 showed a roughly linear decrease in I_1/I_3 ratio with no sigmoidal region that would indicate a dissolution of micelles [101]. The linear decrease would be consistent with binding of pyrene to the surface of the protein.

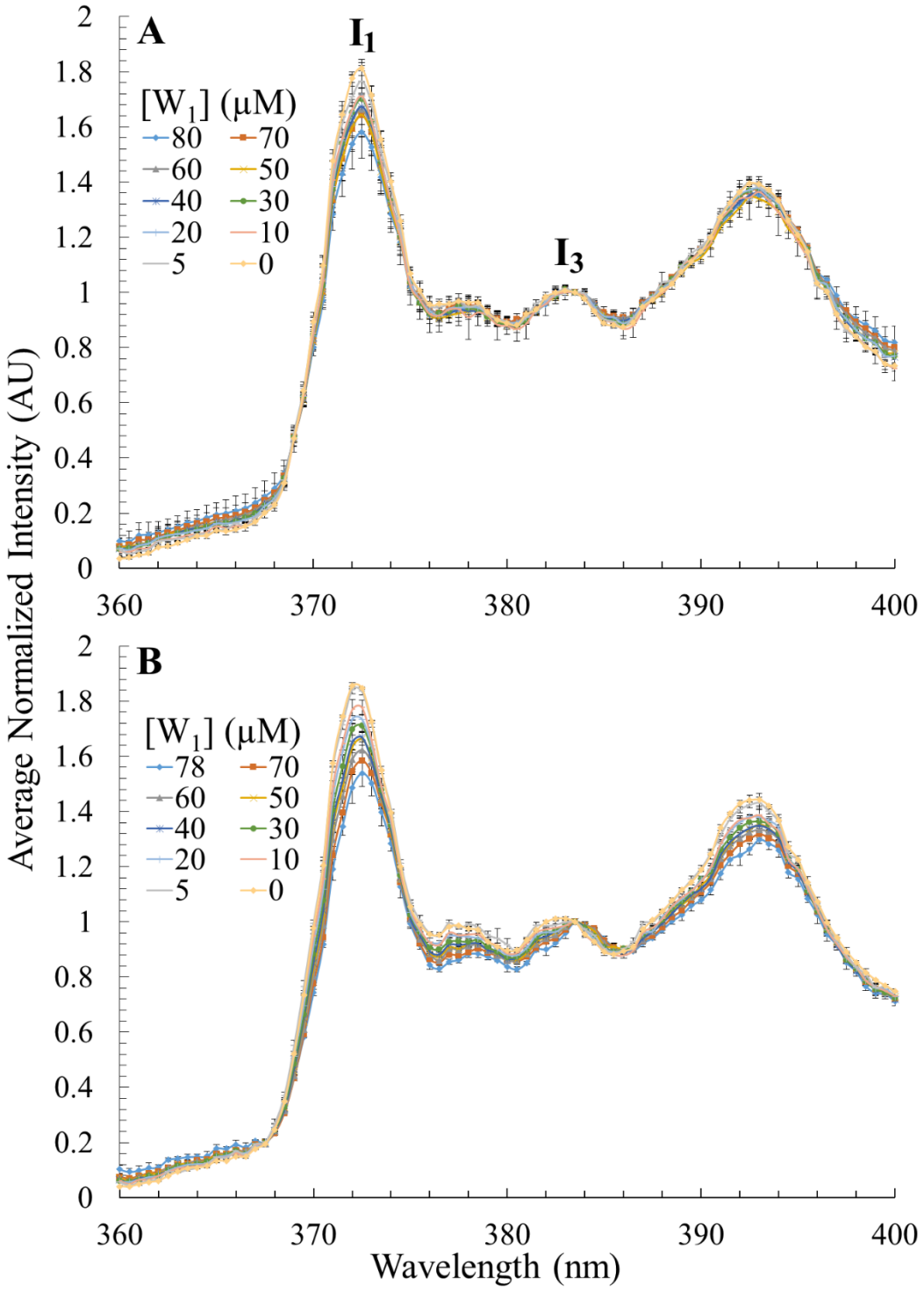

Figure 13: Pyrene emission in the presence of wt (A) and R36W (B) W_1 variants after serial dilution to the indicated protein concentration. I_1 and I_3 vibronic peaks labelled. Intensities are given in arbitrary units (AU) and normalized by the I_3 peak intensity

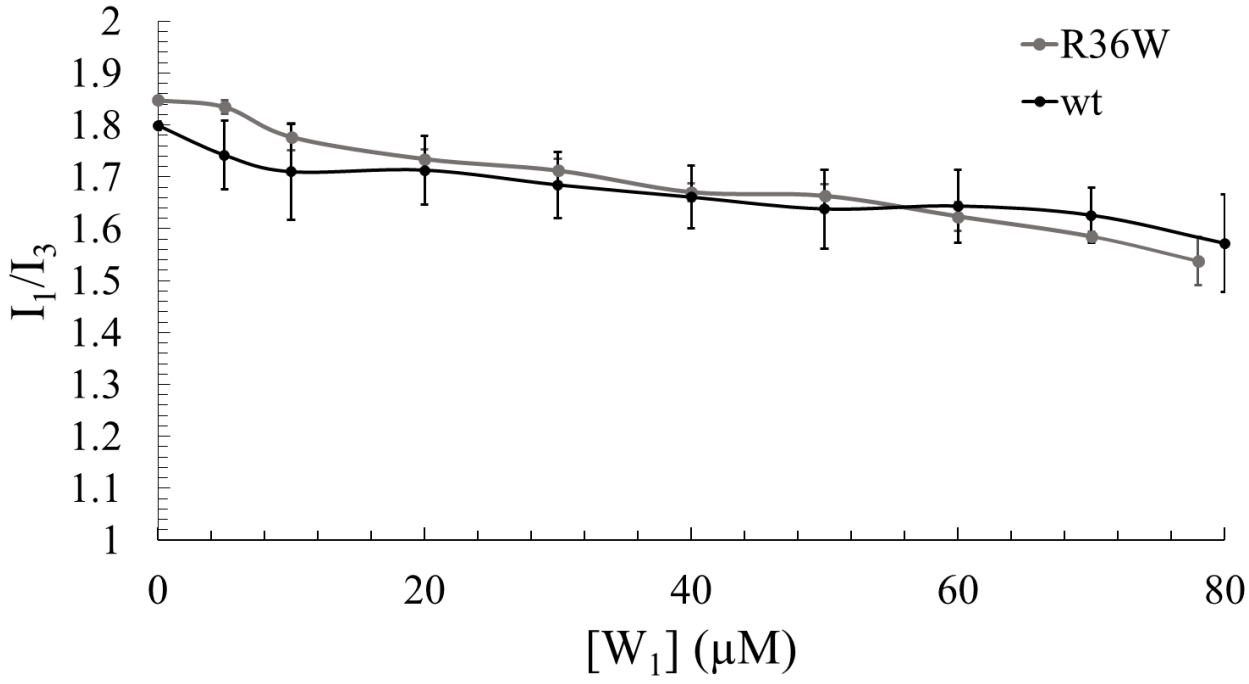

Figure 14: Ratio of pyrene (0.1 μM) fluorescence emission intensities at I_1 (372.5 nm) and I_3 (383.5 nm) after incubation with and serial dilution of R36W or wild-type W_1 in 50 mM potassium phosphate buffer (pH 7.5). λ_{ex} = 332 nm

The possibility of FRET taking place between the R36W residue (as the donor) and pyrene (as the acceptor) was examined by testing for tryptophan quenching. Using 80 μM of protein and 10 μM of pyrene, the intensity of tryptophan fluorescence was reduced from 16.0 ± 0.5 to 14.3 ± 0.5 AU, giving an ~11% decrease (Figure 15). The decrease is roughly equal to a loss of 1/8th of the original intensity, which matches the ratio of pyrene to protein. This is consistent with a 1:1 binding of pyrene to W_1 resulting in a stable non-fluorescent complex.

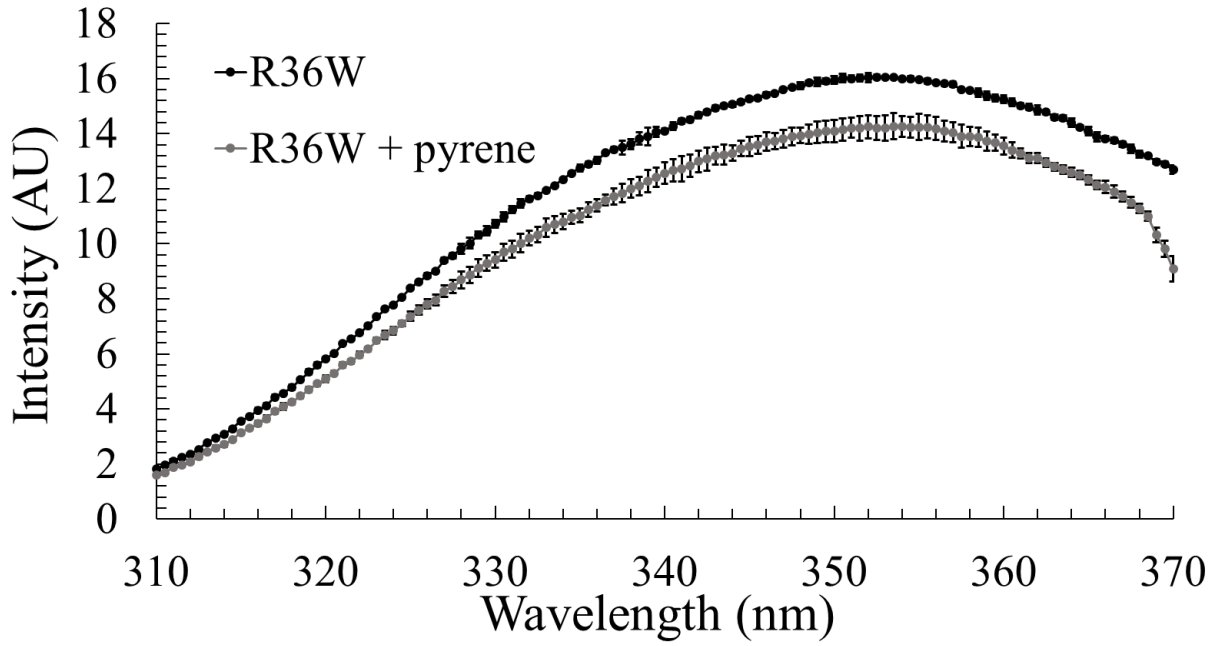

Figure 15: Intrinsic tryptophan fluorescence (λ_{ex} = 298 nm) of W_1 variant R36W (80 μM) with or without pyrene (10 μM) in 50 mM potassium phosphate buffer (pH 7.5).

2.3.2 Size and Yield of W_1 Micelles

Three replicate experiments were performed using 50 μM wild-type W_1 (Figure 16), which were subjected to filtration at a cutoff of 0.02 μm and measured within minutes by DLS. Under these conditions, scattering consistent only with monomers was observed (Figure 16A), with a hydrodynamic diameter (4 to 6 nm) close to the previously determined 4.3 nm for W_1 [49]. This indicates that nanoparticle formation by W_1 under these conditions is a slow rather than rapid process, likely occurring on a scale of hours. For future elaboration of this process, time-dependent evaluation of nanoparticle formation should be investigated. The small amount of scattering arising from species that are consistent with ~10 nm particles in replicate 3 is likely a fitting error of the low signal-to-noise correlation function.

After incubation at 4 ºC for 24 h and 1 to 2 h at room temperature, the same samples were re-measured without filtration. In all replicates, micelle-like nanoparticle formation was detected and the sizes of populations were consistent between replicates; however, not all populations were present in every replicate (Figure 16B). In replicates 1 and 2, a population of particles ranging from 180 to 750 nm with a mean size of ~400 nm was detected. Replicate 3 did not show these larger nanoparticles, but did show particles of ~45 nm in size, while replicate 2 showed both the larger particles and a smaller population with ~60 nm size. In all cases, the monomer is the predominant scattering species by number or volume, with upwards of 99.9% contribution, and therefore the yield of W_1 nanoparticles is low. Though somewhat inconsistent, these results match previous observations of W_1 by DLS [91], which showed dual populations of ~50 nm and ~200 nm particles after filtration by a 0.45 μm syringe filter. The smaller size for the larger population that was previously observed [91] is presumably due to filtrations with a 0.45 μm cutoff, a step which is absent for this study. Therefore, these results show that micron-scale W_1 nanoparticles do not form after 24 h under the conditions of this experiment.

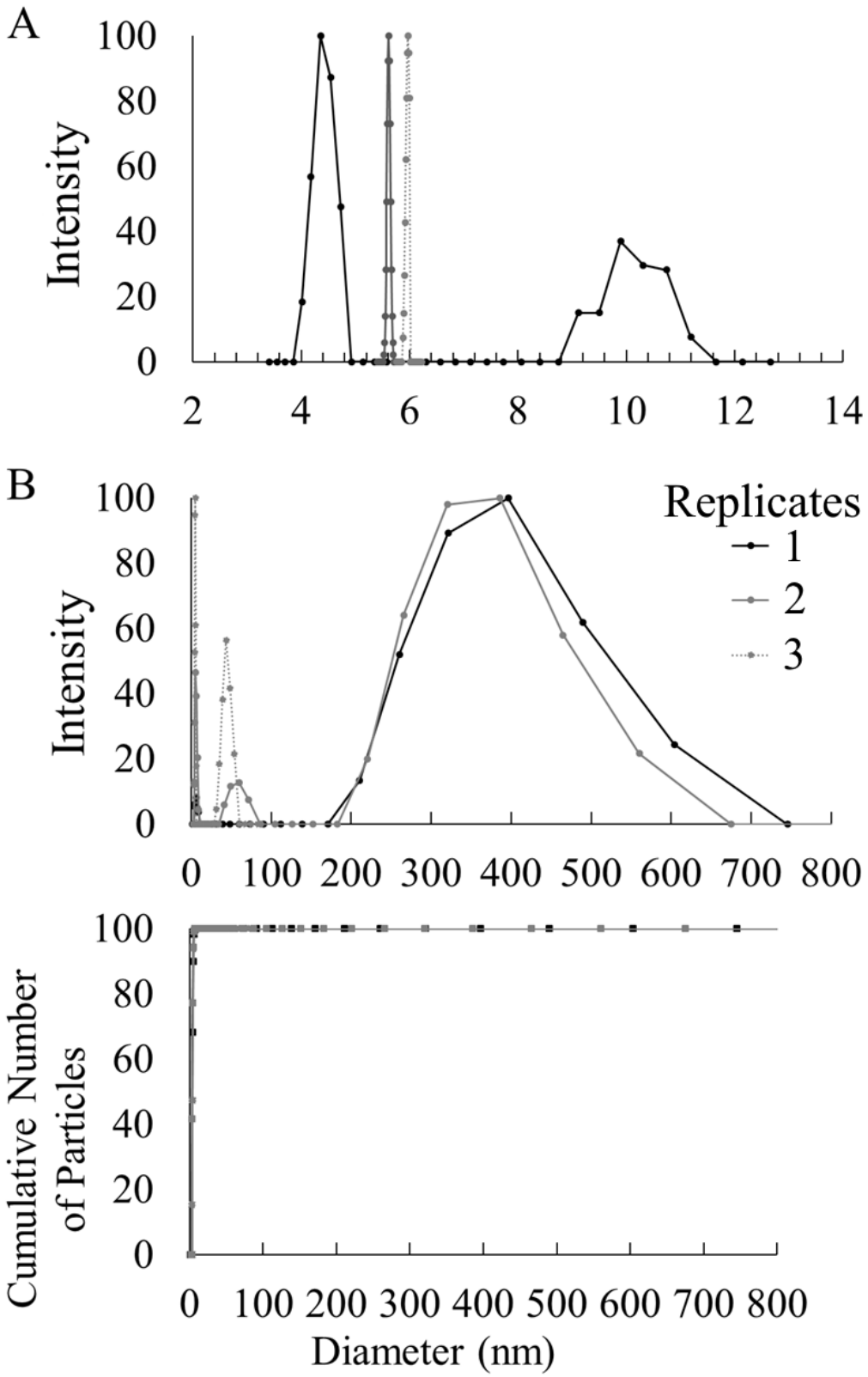

Figure 16: Dynamic light scattering of W_1 in 50 mM potassium phosphate buffer (pH 7.5) immediately after filtration by 0.02 µm (A) and after incubation for ~24 h (B)

2.4 Surface Assembly of Recombinant AcSp1

2.4.1 Kinetics of Surface Adsorption

Through surface pressure measurement of W_1 as a function of time, liquid-air interface adsorption appears to occur very rapidly at first, with a roughly logarithmic decay in adsorption rate as time increases (Figure 17). This was fit by a Langmuir isotherm (Eq. 37) with a k_a constant of 0.03 $s^{-1} \cdot \mu M^{-1}$ and a k_d constant of 0 under the assumption that the desorption rate is negligible. In comparison, surface layers formed by W_2 had more integrity in that they held the Wilhelmy plate in a fixed position on the surface of the layer as the dish was moved laterally, while W_1 surface layers did not, allowing the plate to remain vertical (i.e., changing position relative to the surface layer itself). When a liquid drop of W_2 solution on the end of a pipette tip was slowly lowered towards the surface of the W_2 solution, the two liquids fused quickly by a two-ended funnel shaped connection, which produced a short fibre. This suggests that the alignment and possible conformational change of proteins at the liquid-air interface may be relatable to those which occur in the spinning duct prior to fibre formation.

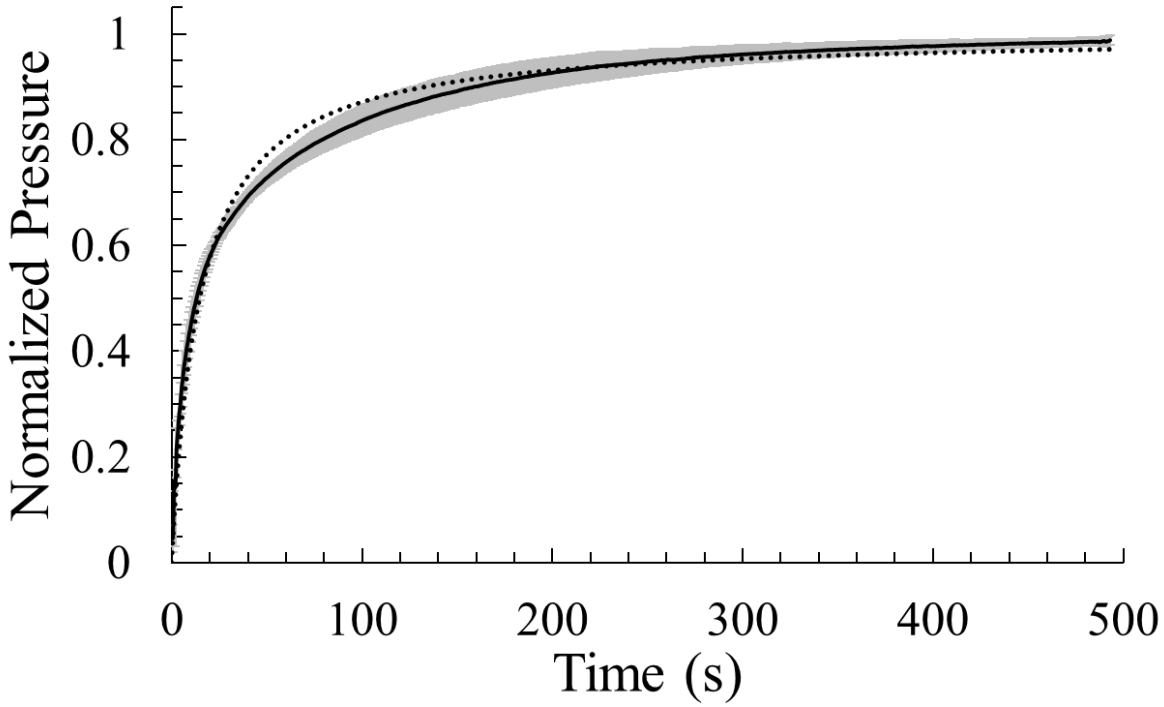

Figure 17: Change in surface pressure due to surface adsorption and assembly of 2.25 µM W_1 in 50 mM potassium phosphate buffer (pH 7.5). Experimental data (solid line), Langmuir isotherm (Eq. 37) (dotted line), shaded area (standard deviation)

2.5 Summary of Solution-State Assembly Results

The W_1 protein was observed to form micelle-like nanoparticles; however the micelle population relative to the monomeric form was very low and formed slowly (Figure 16). Two separate populations of micelle-like nanoparticles were observed: one of ~40 to 100 nm, and one of ~180 to 750 nm in diameter. This is consistent with previous results [91], however the lack of filtration prior to measurement in this study allows for observation of particles larger than the physical cutoff of 450 nm in diameter employed in the previous study.

As a result of the low micelle population, the solvent exposure of the tryptophan residues of the W_1 variants in the micellar state could not be observed by their intrinsic fluorescence (Figure 9). However, the solvent exposure of the R36W residue was surprisingly high, as inferred from its emission maximum relative the heptapeptide control and the other W_1 variants. The Y169W and F146W variants were expected to have a high solvent exposure due to their locations in the protein, and their *in silico* structures [89]. However, R36W was predicted to be well buried based on the *in silico* structure [89], which implies that this structure is not completely accurate. The thermal precipitation of the R36W variant at 65 °C (Figure 12), which does not occur for the other variants or wild-type, coincides with the early stages of W_1 unfolding [91], which initiates by disruption to helix-5 [89]. The R36W variant also appears to be sensitized to shear forces in the presence of pyrene, based on the observed precipitation when vortexed.

Pyrene fluorescence showed an approximately linear increase in I_1/I_3 ratio as the protein was diluted for the R36W and wild-type variants, after a 30 min incubation (Figure 14). This contrasts with a previous experiment which showed sigmoidal behaviour of the I_1/I_3 ratio after a 24 h incubation, from which the CMC of ~20 μM was estimated. Sigmoidal behaviour is an indicator of micelle dissolution [101] upon dilution of the protein solution, and the linear decrease likely reflects surface binding of pyrene to the protein surface. The apparent FRET between pyrene and the R36W residue (Figure 15) suggests that pyrene molecules bind to the surface nearby R36W, which is located beneath helix 5 [49].

The W_1 protein shows adsorption to the liquid-air interface, which closely matches a Langmuir isotherm (Figure 17). This suggests that W_1 adsorption is primarily a diffusion-controlled process with little rearrangement at the surface. W_2 surface layers qualitatively showed a greater integrity than W_1 surface layers, which suggests that W_2 participates greater

arrangement at the surface. The fusion of a droplet containing W_2 solution with the surface layer of W_2 results in fibre formation, and the alignment of W_2 at the surface may similar to the alignment in the spinning duct.

Chapter 3: Nanoparticle Production by Recombinant AcSp1

As discussed in Section 1.5.2, dragline silk and silkworm fibroins form nanoparticles capable of *in vitro* drug delivery. Silk nanoparticles can have different properties and drug compatibilities based on mutations to the protein sequence, as discussed in Section 1.5.5. Therefore, expanding the variety of silk protein nanoparticles that can be robustly produced would allow for the selection of properties and compatibilities that are desirable for a given application.

Recombinant AcSp1 has been shown to form nanoparticles, as detailed in Section 1.3.4, but the properties of these particles have not yet been extensively investigated. Furthermore, methods to favourably produce these particles have not been developed. Given differences between aciniform and other silks (Sections 1.1.1 to 1.1.3), these nanoparticles may have desirable drug compatibilities and drug release profiles that are distinct from other silks.

The objective detailed in this Chapter was to develop a protocol to produce nanoparticles from recombinant AcSp1 which are stable in solution, and to characterise their size, morphology, and the conformation of the constituent AcSp1 proteins in the nanoparticle state. Specifically, DLS was used to measure the size and dispersity of nanoparticles in parallel with SEM determination of both particle size and morphology. The secondary structure of the AcSp1 protein in the nanoparticle state was characterized using CD spectroscopy, while the orientation and packing of proteins within the nanoparticles was measured using tryptophan fluorescence to track the relative solvent exposure of the tryptophan residues of W_1 variants. Using this set of experimental protocols, the effectiveness and robustness of a variety of nanoparticle production and stabilization protocols were compared. Ultimately, W_1 is able to form nanoparticles of a defined and desirable size, however they are not stable under aqueous conditions.

3.1 Materials and Methods

3.1.1 Nanoparticle Production

For nanoparticle production, all solutions used were filtered through 0.2-µm filters and all containers for sample and filtered solutions were pre-washed with double distilled H_2O (ddH_2O) filtered through 0.2-µm filters to prevent incorporation of dust into samples.

Nanoparticles formed by desolvation were produced by mixing solutions of W_1 in 20 mM sodium acetate (pH 5.0) with a solution of alcohol to a particular final concentration of alcohol. Alcohol solutions were prepared by dilution with ddH_2O and were then mixed with W_1 solutions at a 10:1 volume ratio to ensure a uniform mixing rate between samples. To mix samples, the larger volume of alcohol was quickly pipetted into the protein solution and immediately vortexed to help ensure a consistent mixing rate. Nanoparticles formed by salt precipitation were produced using the same methodology, however protein solutions were mixed with 1.5 M potassium phosphate (pH 7.5).

Lyophilization was applied to nanoparticles prepared using the desolvation protocol described above. Nanoparticle solutions were quickly diluted by a solution of glucose as a cryoprotectant, and sodium azide as a biocide, to final concentrations of 1% and 1 mM respectively, and then lyophilized. This lyophilization process allows for the removal of ethanol and resuspension in water without the irreversible compaction that occurred due to centrifugation, and the glucose protects the nanoparticles from aggregation by hydrogen bonding to the protein surface [214]. Diluted samples were lyophilized and resuspended in 0.1-µm filtered ddH_2O.

3.1.2 Dynamic Light Scattering

DLS measurements were carried out using a BI-200SM instrument and analysed using BI-ISTW software (Brookhaven Instruments, NY, USA), at 25 °C and an angle of 120° in a quartz cell (1 cm, Hellma Analytics, Markham, ON, CA) with a wavelength of 637 nm. Viscosities were measured with a µVISC viscometer (RheoSense, Inc., San Ramon, CA, US) and refractive indexes with a Refracto 30GS refractometer (METTLER TOLEDO, Columbus, OH, US)

Resuspended lyophilized nanoparticles were produced using an initial concentration of ~141 µM prior to mixing with ethanol to final concentration of by the method described in Section 3.1.1, and measured with an angle of 120º at 23 ºC with a measured viscosity of 1.000 ± 0.001 cP and measured refractive index of 1.3336 ± 0.0001 as the average of three samples.

The stability and behaviour of un-lyophilized W_1 nanoparticles in ethanol as a function of time was measured using samples prepared using an initial W_1 concentration of 20 µM and a final ethanol concentration of ~91%, by the method described in Section 3.1.1. W_1

concentrations were measured by absorbance at 210 nm with an estimated [83] extinction coefficient of 270858 $M^{-1} \cdot cm^{-1}$. Nanoparticle suspensions were then measured at different time points with a measurement time of less than 25 s. Samples were measured with an angle of 120º at 23 ºC with measured viscosities of 1.636 ± 0.008, 1.623 ± 0.004, and 1.66 ± 0.04 cP for three replicates and refractive indices of 1.3638 ± 0.0002 for all three replicates.

3.1.3 Fluorescence

All emission spectroscopy measurements were performed in triplicate, with each replicate being the average of 3 scans. Experiments were carried out using a Cary Eclipse spectrofluorometer (Varian, Palo Alto, CA, US) using a 1-cm quartz cuvette (Varian, Palo Alto, CA, US).

Tryptophan fluorescence emission of un-lyophilized W_1 nanoparticles in ethanol and methanol was measured over 310 to 370 nm (slit width: 5 nm) with excitation at 298 nm (slit width: 5 nm), averaging time of 0.5 s and 1-nm intervals at 20 °C. Samples were prepared as described in Section 3.1.1, except that 100% ethanol was added at a 5:1 volume ratio to a final concentration of ~83% alcohol. Initial W_1 concentrations were 142 µM for R36W, 70 µM for F146W, 185 µM for Y169W and 142 µM for the heptapeptide (PGPWQGG) control. W_1 concentrations were measured by absorbance at 210 nm with an estimated [83] extinction coefficient of 270858 $M^{-1} \cdot cm^{-1}$. The concentration of the heptapeptide was determined by mass of the dried peptide powder. Another sample of Y169W was prepared by diluting 600 µL of a 20 µM protein solution with 6 mL of alcohol followed by air drying to ~600 uL, the emission slit width for this sample was 10 nm. The heptapeptide concentration was 23.7 µM.

3.1.4 Circular Dichroism Spectroscopy

CD spectra of un-lyophilized W_1 nanoparticles in ethanol and methanol were measured over 250 to 190 nm with 1-nm increments, and using averaging time as a function of the detector high volts, which compensates for differences in the lamp intensity at each measured wavelength, at 20 ºC in a 2-mm quartz cell (Starna Cells, Inc, Atascadero, CA, USA). Samples were prepared as described in Section 3.1.1, except that 100% ethanol was added at a 5:1 volume ratio to a final concentration of ~83% alcohol. Initial W_1 concentrations were 49 µM for R36W, 70 µM for F146W, 73 µM for Y169W and 64 µM for wild-type. W_1 concentrations were

measured by absorbance at 210 nm with an estimated [83] extinction coefficient of 270858 $M^{-1} \cdot cm^{-1}$. Spectra were measured in triplicate using a DSM20 spectrometer and Globalworks software (Olis, Bogart, GA, USA) and were converted to mean residue ellipticity using equation 23.

3.1.5 Scanning Electron Microscopy

SEM samples of un-lyophilized W_1 nanoparticles in alcohol were produced by diluting a solution of 50 μM W_1 in 20 mM sodium acetate (pH 5.0) with 100% ethanol or methanol to a final concentration of ~91% alcohol by pipetting and vortexing quickly. A 10-μL aliquot of nanoparticle solution was then deposited on mica and air dried. Samples were sputter coated with gold-palladium using an EM ACE200 (Leica, Wetzlar, Germany) at the Scientific Imaging Suite (Dalhousie University) with a diffuse coating method for 100 s, and measured with a S-4700 Cold Field Emission microscope (Hitachi, Tokyo, Japan) at the Facilities for Materials Characterization (Dalhousie University).

3.2 Nanoparticle Production Schemes

3.2.1 Desolvation

Wild-type W_1 forms nanoparticles less than 100 nm in diameter by desolvation in either ~91% (v/v) ethanol or ~91% (v/v) methanol (Figure 18) as observed by SEM. Particles that were produced in ethanol had a defined spheroid shape; however, aggregation and conjoined particles were prevalent. Particles that were produced in methanol were smaller, but less spherical in nature and heavily aggregated compared to the ethanol-induced particles. The apparently aggregated state of the particles is likely due to the dehydration of particles solutions during sample preparation, which results in an increased concentration of particles.

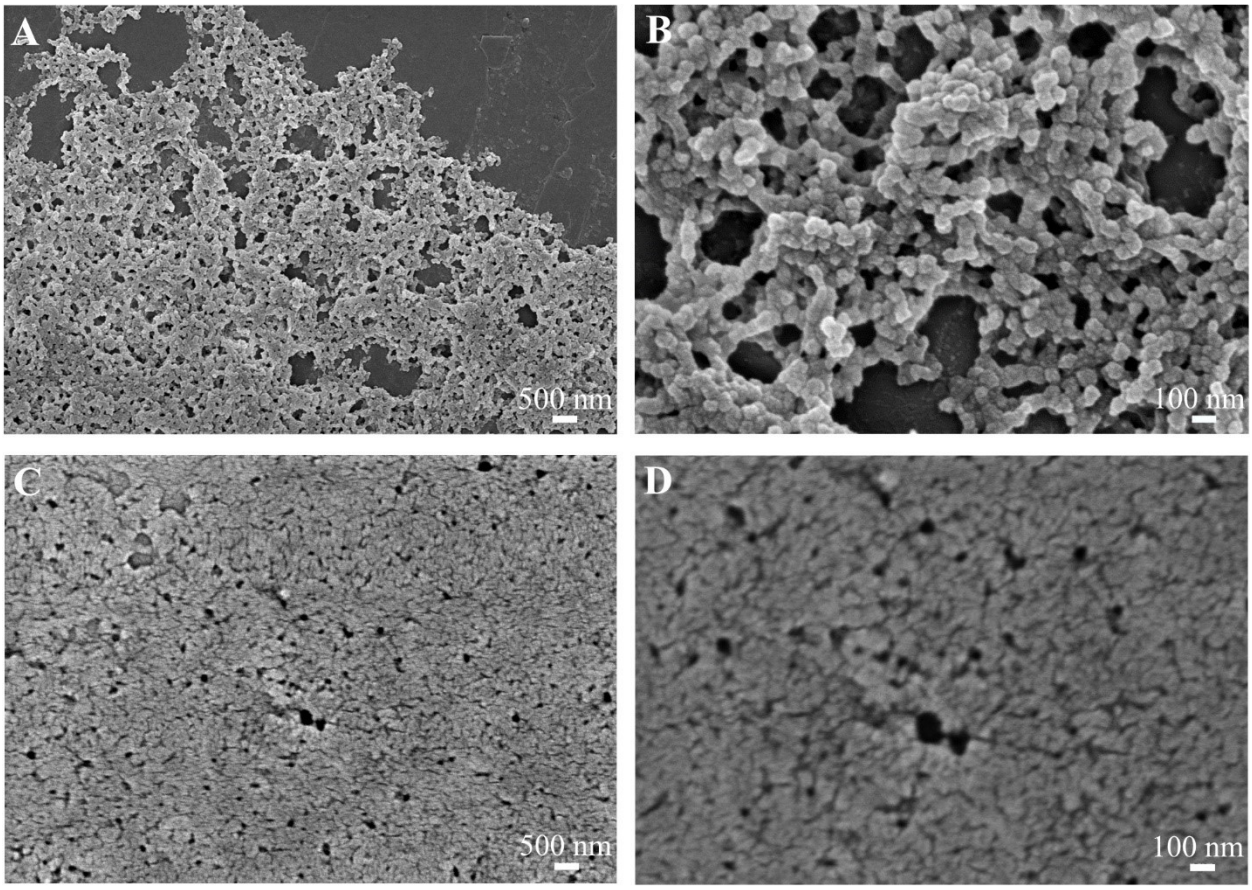

Figure 18: SEM of W_1 nanoparticles formed in ~91% (v/v) ethanol (A,B) and methanol (C,D) following deposition from alcohol solution onto mica.

3.2.2 Stability in Storage Solution

Dialysis of nanoparticles formed in ~91% (v/v) ethanol into distilled H_2O, 20 mM sodium acetate (pH 5.0), or 50 mM potassium phosphate (pH 7.5) overnight resulted in macroscopic aggregation. Nanoparticles formed in ethanol and stored in ethanol overnight settled out of solution, but could be resuspended by vortexing without any visible aggregation. W_1 nanoparticle populations in ethanol were assessed by DLS at different time points after formation without disturbing the solutions in-between measurements. After ~10 min, the mean particle size became increasingly inconsistent, with micron-sized particles more prevalent overall (Figure 19). At the first time point, two replicates converge on a size of ~100 nm in diameter, and sizes between 80 and 120 nm in diameter occur at later time points. This size range is similar to that which was observed by SEM (Figure 18).

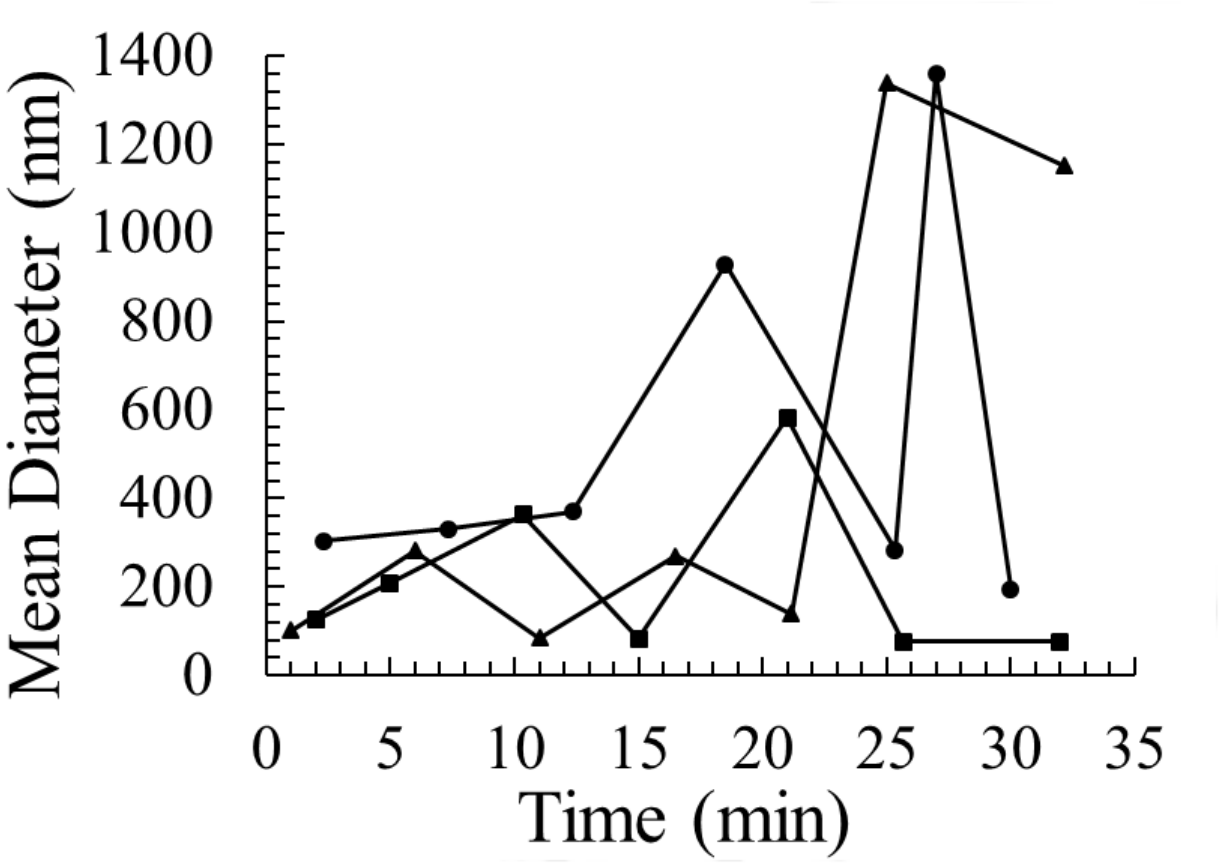

Figure 19: W_1 nanoparticles in ~91% (v/v) ethanol measured at the indicated times after initial formation without mixing, three replicates are shown

3.2.3 Salt Precipitation

Nanoparticle formation by W_1 could also be induced by mixing W_1 in 50 mM potassium phosphate (pH 7.5) with a solution of 1.5 M potassium phosphate buffer (pH 7.5). Nanoparticle formation was screened for by the observation of formation of a hazy solution which indicated that a suspension of particles was formed. Centrifugation of the particle solutions at 20,000 rcf resulted in pellet formation, which confirmed that suspended particles were present. Sizes of particles formed by this method have not been investigated due to rapid aggregation. Research was focused instead on desolvation methods as they appeared to form stable nanoparticle suspensions.

3.3 Size and Morphology of Nanoparticles

3.3.1 Solvent Concentration

The un-lyophilized particles (Figure 18) were smaller than what is observed by DLS for the lyophilized nanoparticles (Figure 20) for ~91% (v/v) ethanol. This is possibly due to swelling and hydration of the nanoparticles in water which is not present for the dehydrated nanoparticles measured by SEM. The aggregated state observed by SEM (Figure 18) for the un-lyophilized particles was not observed for the resuspended lyophilized particles (Figure 20), which suggests that the aggregation was due to dehydration during SEM sample preparation.

Desolvation by ethanol followed by lyophilization with glucose as a cryoprotectant predominantly produced nanoparticles less than 200 nm in diameter, with almost all particles being less than 400 nm in diameter, as seen by the cumulative number of particles by diameter (Figure 20). Samples produced in ~91% (v/v) ethanol appear larger than at other concentrations as well as having a greater percentage of particles larger than 200 nm in diameter. Nanoparticles formed at lower concentrations of ethanol show more uniform size distributions overall and are smaller in size than nanoparticles formed in 91% (v/v) ethanol. Variability between replicates of the same ethanol concentration is apparent and there does not appear to be a correlation between ethanol concentration and nanoparticle size at concentrations below 73% (v/v).

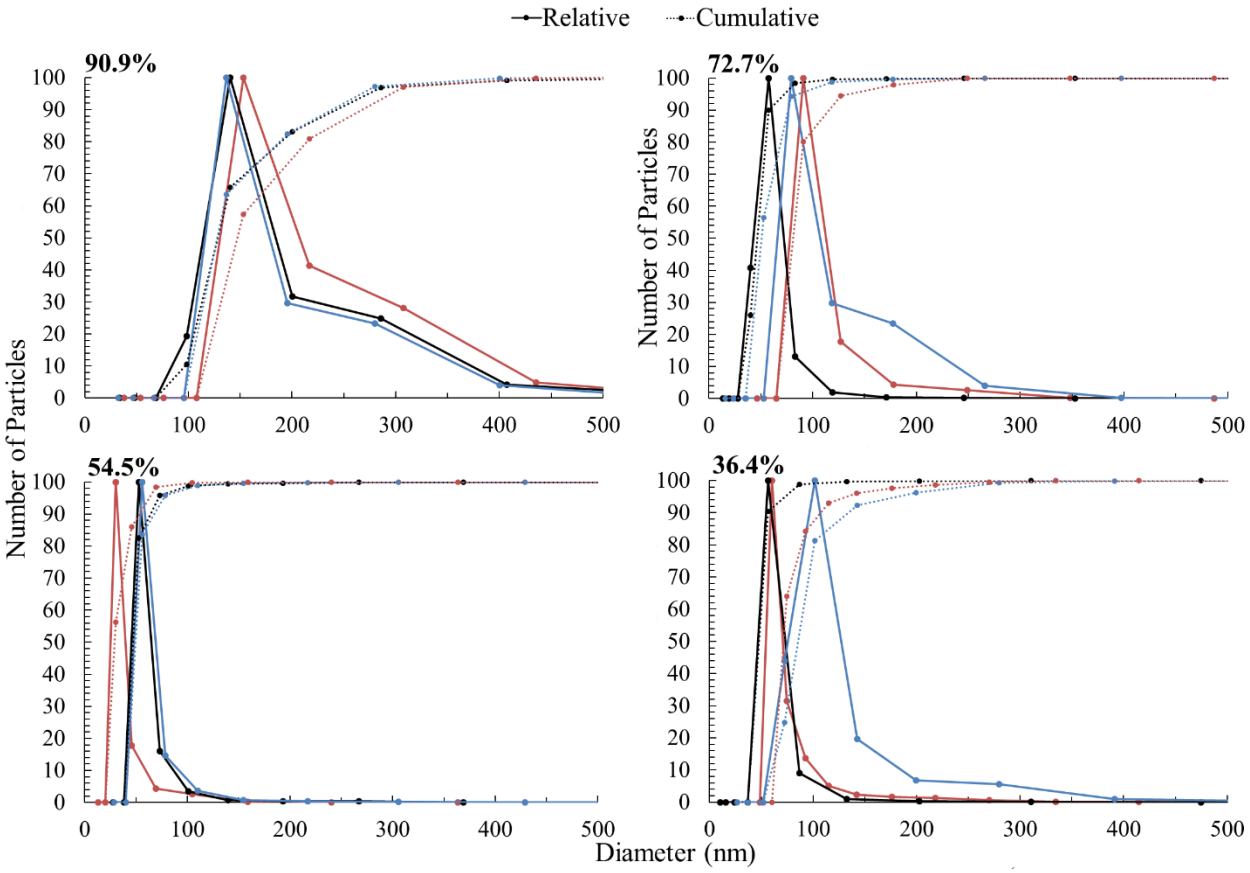

Figure 20: DLS of wild-type W_1 nanoparticles formed by desolvation in the indicated concentration of ethanol (%) after lyophilization with 1% glucose and redispersion in H_2O. Relative and cumulative give the size distribution and percent of total number of particles respectively. Three replicates are shown on each graph

3.4 Protein Conformation in the Nanoparticle State

3.4.1 Secondary Structure

The secondary structure of a variety of un-lyophilized nanoparticle types in alcohol was probed by far-UV circular dichroism (CD) spectroscopy. For all tryptophan variants and wild-type W_1, the same spectral shape was observed in ethanol and methanol solutions (Figure 21). Namely, a positive band was observed at ~198 nm and a single negative band between ~220 and ~225 nm, with slight variations in the position of the negative band between variants and between ethanol and methanol (Figure 21). The difference in the position of the negative bands is similar for all of the W_1 variants, with methanol at ~220 nm and ethanol at ~225 nm, although

the band for wild-type W_1 is closer to ~223 nm in ethanol. For all of the W_1 variants, the intensity of the positive band is lower in methanol.

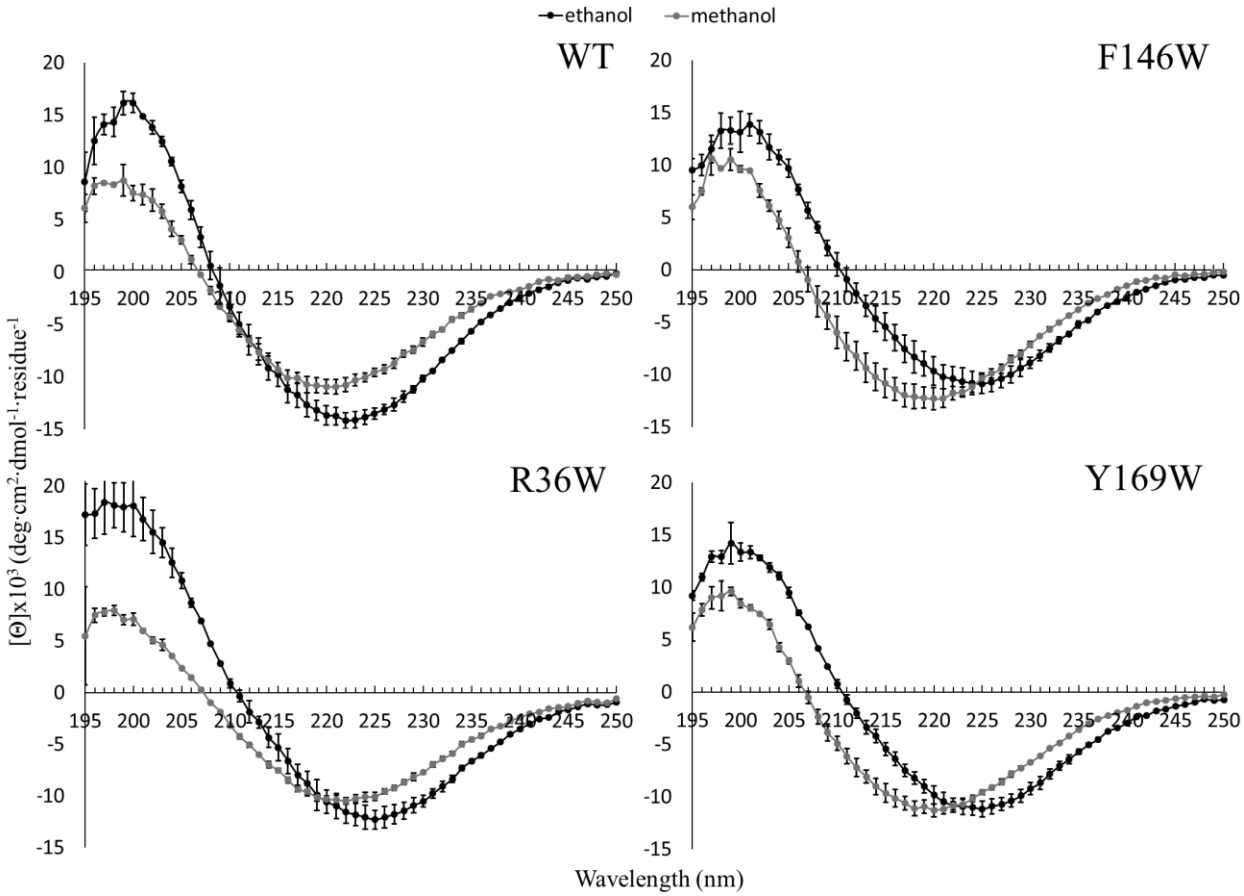

Figure 21: CD-spectra of wild-type W_1 and its variants in ~83% (v/v) solution of the specified alcohol after mixing protein in 20 mM acetate buffer (pH 5.0) with 100% alcohol

A single negative band at 220 to 225 nm with a positive band at 195 to 200 nm is consistent with a β-sheet-rich protein [188] (Figure 7). This implies a transition from α-helix-rich (Section 1.3.1) to β-sheet-rich conformational state. Interestingly, such a transition is associated with fibre formation by AcSp1 [82], as discussed in Section 1.3.3.

3.4.2 Solvent Exposure of Tryptophan Substitutions

Intrinsic tryptophan fluorescence of each substituted W_1 variant was used to test for the degree of solvent exposure in the nanoparticle state at a given tryptophan site. Namely, this would be sensitive to region of the W_1 protein being exposed to the solvent or to the solvent-excluded interior of the nanoparticle. A small blue-shift is observed for each variant in alcohol compared to H_2O (Table 3 and Figure 22), as expected due to the lower solvent polarity in each of the ~91% alcohol conditions relative to H_2O.

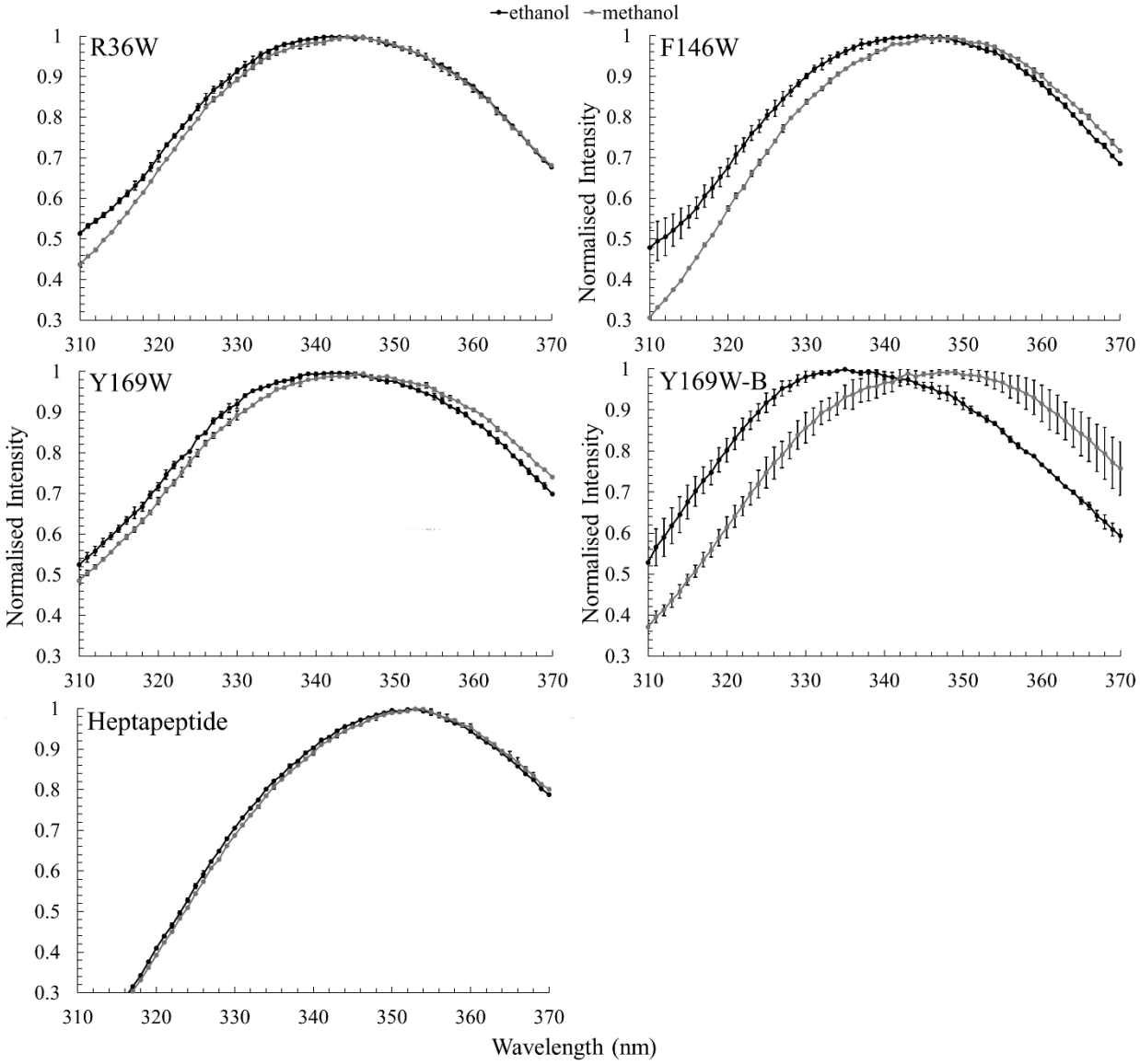

Figure 22: Intrinsic tryptophan fluorescence of wild-type W_1 and its variants in ~83% solution of the specified alcohol after mixing the protein in 20 mM acetate buffer (pH 5.0) with 100% alcohol. Y169W-B was concentrated by air drying

The wavelengths of the emission maxima of W_1 variants are relatively close to that of the heptapeptide control, as were the maxima under aqueous conditions (Table 2, Section 2.3.1). This indicates the tryptophan residues of the W_1 variants are still well exposed to solvent in the nanoparticle state.

The sample of Y169W-B in ethanol (Figure 22) was at a slightly higher concentration than the Y169W sample after an air-drying process. A more significant blue-shift was observed for Y169W-B in ethanol than for Y169W, which suggests that above a certain concentration the nanoparticles begin to aggregate. Presumably the molecules of ethanol are able to shield hydrophobic protein surfaces at lower concentrations, or the aggregation occurs at a slower time scale than the measurement. However these aggregates were not visible, and the Y169W-B samples showed the same haziness as the other samples. Therefore, this is not likely to be an irreversible aggregation process.

Table 3: Intrinsic tryptophan fluorescence (λ_{ex} = 298 nm) of W_1 variants and the heptapeptide control in ~83% solution of specified alcohol after mixing protein in 20 mM acetate buffer (pH 5.0) with 100% alcohol

	Emission Maxima (nm)				
Solvent	**R36W**	**F146W**	**Y169W**	**Y169W-B**	**Heptapeptide (PGPWQGG)**
ethanol	343.3 ± 0.3	344.0 ± 0.2	342.6 ± 0.4	337 ± 1	352.5 ± 0.1
methanol	343.7 ± 0.3	346.7 ± 0.1	345.0 ± 0.3	347 ± 4	353.3 ± 0.2
***H_2O**	353.6 ± 0.2	354.4 ± 0.1	356.2 ± 0.4	N/A	358.7 ± 0.2

*H_2O values taken from Table 2 for pH 7.5; N/A: not available

3.5 Capture and Storage of Nanoparticles

3.5.1 Concentration and Resuspension

Nanoparticle recovery by centrifugation and resuspension was attempted. Regardless of the W_1 nanoparticle production method, pelleted nanoparticle suspensions were not amenable to resuspension, as observed by persistence of the pellet in either aqueous or alcohol solutions. Sonication had marginal effects on resuspension. Desolvation-induced nanoparticles that were air-dried and those lyophilized without cryoprotectant were similarly not amenable to resuspension.

3.6 Summary of Nanoparticle Results

Nanoparticles were formed by desolvation and salt precipitation of W_1 solutions. Nanoparticles formed by salting out with potassium phosphate were unstable and visibly aggregated in solution. Nanoparticles formed by desolvation with ethanol and methanol did not show visible aggregation and were characterised further; however, DLS of nanoparticles in ethanol at increasing time intervals suggested reversible coagulation (Figure 19). Nanoparticles formed by mixing protein with ethanol without further treatment showed a defined spheroid shape and were less than ~100 nm in diameter when observed by SEM, while those formed using methanol were smaller with a less defined shape (Figure 18). The minimum mean diameter of nanoparticles in ethanol measured by DLS was in the range of 80 to 120 nm (Figure 19), which roughly matches the size observed by SEM, although the time-dependent aggregation makes precise measurement by DLS difficult. The aggregation of the nanoparticles observed by SEM is likely due to dehydration and resulting increase in particle concentration that occurs during SEM sample preparation. This explanation is supported by the apparent decrease in solvent exposure of the Y169W residue in ethanol (i.e., the blue shift observed, Table 3) when the nanoparticle solution was concentrated by air drying.

Lyophilization with glucose as a cryoprotectant was used in order to make W_1 nanoparticles more amenable to resuspension in aqueous solutions. Resuspended nanoparticles were analysed by DLS and showed diameters of ~150 nm for samples formed using ~91 % ethanol, with some larger species of up to 500 nm in diameter (Figure 20). The larger size of the lyophilized and resuspended nanoparticles measured by DLS compared to the un-lyophilized

nanoparticles observed by SEM may be due to swelling and the presence of a hydration shell under aqueous conditions. Lyophilized nanoparticles formed using lower concentrations of ethanol were smaller in diameter, overall, with fewer aggregates (Figure 20).

Un-lyophilized nanoparticles formed in ethanol or methanol were measured using CD, and showed β-sheet-like spectra (Figure 21). The negative band occurred at a slightly shorter wavelength for the particles formed using methanol than for those formed using ethanol. This may be related to the morphological differences between the particles formed in ethanol and methanol solutions that were observed using SEM (Figure 18). No clear difference in the CD spectral band structure was observed between the wild-type and tryptophan-substituted W_1 variants. Therefore, the secondary structure of W_1 in the nanoparticle state is not noticeably affected by the tryptophan substitutions.

Tryptophan residues of the nanoparticles formed using the W_1 variants showed a high level of solvent exposure, regardless of the solvent condition in which the particles were suspended, with exposure comparable to the fully exposed heptapeptide control (Table 3). This was inferred from the emission maxima measured using tryptophan fluorescence. The high level of solvent exposure observed in all instances indicates that these tryptophan residues are either not buried in the nanoparticle interior or that the nanoparticles are sufficiently loosely packed to allow for solvent penetration.

Chapter 4: Discussion

4.1 Solution-State Assembly of Recombinant AcSp1

Micellization, as a protein association event, may involve some degree of conformational change to the protein. Based on the potential CMC of ~20 μM observed previously by pyrene fluorescence [91], it would be expected that at 40 μM roughly half of the protein would be involved in a micellar state. However, at a concentration of up to 50 μM, no change in tryptophan emission maxima was observed for any of the W_1 variants tested (Figure 9). This indicates that either these residues are not buried within any micelle-like structures that are formed or that no such structures are formed in significant quantity. Consistent with these fluorescence spectroscopy results, DLS of filtered W_1 shows that W_1 nanoparticle formation is both slow and very low in yield under these conditions (Figure 16).

Though somewhat inconsistent, the size distributions of W_1 nanoparticles formed after filtration through a 0.02 μm filter match previous observations of W_1 [91], which showed dual populations of ~50 nm and ~200 nm after filtration through a 0.45 μm filter. The particles observed in Figure 16B are larger likely due to the lack of filtration prior to measurement. The roughly linear relationship between the I_1/I_3 ratio of pyrene and W_1 concentration (Figure 14) with 30 min incubation would be consistent with binding of pyrene to the protein surface rather than incorporation into micelles. This contrasts with the previous study, which showed micelle-like behaviour [91] after ~24 h incubation. The shorter, 30 min incubation was chosen due to the observation of significant visible precipitation of the R36W variant after incubation with pyrene overnight. The I_1/I_3 values cannot be directly compared between the two experiments due to a significant difference in the emission spectra. The spectra for the 24-h incubated samples show two maxima at 372 and 389 nm, which were chosen as I_1 and I_3 respectively [91]. In contrast, the spectra obtained in the course of the present study exhibit the 5 expected [98] emission bands, with 372.5 and 383.5 nm selected as I_1 and I_3, respectively, following literature precedent [98]. The source of this discrepancy between the two experiments is not clear. The difference in incubation time between the present (30 min) and the prior (24 h) studies is presumably the source of the difference and, based on the observation of surface binding and propensity of R36W to precipitate in the presence of pyrene with shear force, it is possible that some amount of protein aggregation or assembly is induced by the pyrene molecule. This could be mediated

by pyrene molecule binding to and exposing or increasing the hydrophobicity of a particular protein surface.

It is important to note that the W_1 protein does not include the C-terminal and N-terminal non-repetitive domains of the native spidroin which are generally believed to contribute to the oligomerization of silk proteins [23, 38, 47]. Furthermore, the native-state chemical composition in the aciniform gland has not been characterised. Additionally, a single repeat unit cannot form the interlocking arrangements required for biomaterial formation. However, the W_1 protein does contain the same potential binding surfaces as a W_2 protein and so if micellization of W_2 occurs then some interaction between W_1 proteins such as dimerization should be expected, regardless of the ability of W_1 proteins to interlock. In the context of these limitations, the lack of significant micellization of W_1 does not indicate that micelle-like particles do not form *in vivo* for the native aciniform protein. These results show that weak interactions between the AcSp1 repeats can occur and that, under certain solution conditions the native or other recombinant AcSp1 may assemble into micellar structures.

All W_1 variants studied show a relatively high solvent exposure at the tryptophan substitution site, based on tryptophan emission maxima (Figure 9) as compared to the fully exposed heptapeptide control (Table 1). The R36W residue, though blue-shifted slightly compared to the F146W and Y169W variants, shows a much higher solvent exposure than the previous structural modelling-based prediction of only 4% solvent accessible surface area [89]. By comparison, the F146W and Y169W residues were predicted to have 71% and 93% solvent accessibility, respectively [89]. This implies that the *in silico* structure of the R36W variant [89] is somewhat inaccurate, at least regarding the regions nearby residue 36, and that in the R36W variant the tryptophan residue is exposed to the solvent in this region.

A significant disruption in the region around the residue R36W that makes contact with helix-5 [89] and the exposed tryptophan residue are likely responsible for the precipitation of the R36W mutant at 65 ºC, as this temperature coincides with the first stages of thermal denaturation of W_1 [91], and denaturation begins with disruption to helix-5 [89]. This would fit with the model that disruption to helix-5 and loosening of the protein surface beneath it [49, 89] initiates the conformational transition in the W-unit during fibre formation. This idea is also supported by the binding of pyrene to this region as observed by tryptophan quenching (Figure 15) and the observation that shear force induces precipitation of R36W in the presence of pyrene or ANS,

but not without. Interestingly, binding of the detergent dodecylphosphocholine (DPC) prevents W_2 from forming fibres despite minimal effects on the protein secondary structure [49]. This would also support the mechanism introduced above if DPC binds at the same location as pyrene. The loss of ~11% of tryptophan emission intensity is close to the ratio of pyrene to protein (0.13), which suggests the formation of a stable complex between pyrene and W_1, resulting in static quenching of tryptophan fluorescence. No blue-shift of the R36W emission maximum was observed, indicating that interaction with pyrene does not affect the solvent exposure of the residue. This is also consistent with a static quenching mechanism, where the ground state is rendered non-fluorescent, instead of a change to the excited state. Pyrene thus appears to bind preferentially to the surface below helix-5, near the R36W residue.

An alternative explanation for this observation is that pyrene binding to other, or to multiple, surfaces of the protein results in conformational changes that alter the chemical environment of the tryptophan residue. This would result in a decreased quantum yield and therefore a decrease emission intensity. It is important to note that the solubility of pyrene in water is <1 μM [215], and so this experiment does not reflect an equilibrium between soluble and protein-bound pyrene that would allow for calculation of a binding constant. Instead the protein may pick-up undissolved pyrene from the surface of the cuvette. No change in emission maxima were observed at pH 5.0 compared to pH 7.5, which is consistent with previous CD results showing no change in secondary structure of W_1 due to change in pH over this range [91].

A complication of these pyrene experiments is that dilution of the protein solution with buffer containing the same concentration of pyrene results in the continual addition of new, pyrene molecules. If hours of incubation of pyrene with the protein is necessary for diffusion into the micellar interior, the continual addition of new pyrene molecules to the system may bias the I_1/I_3 ratio in favour of free or surface bound pyrene. Additionally, the formation of micro-precipitates due to the long incubation is possible, and dilution of pyrene-containing precipitates could mimic micelle dissolution.

The observed surface tension decrease over time by W_1 surface adsorption roughly fits a Langmuir isotherm (Eq. 10), and multiple stages of assembly that would indicate a rearrangement at the surface are not apparent (Figure 17). More specifically, the Langmuir isotherm model closely fits the first half of adsorption, but then the data deviate from the theoretical prediction which would lead to an expectation of a slightly faster rate of adsorption

than the experimental data. The Langmuir isotherm assumes that no intermolecular interactions occur between surfactants and that there are no barriers to adsorption such as steric hindrance. It is also important to note that the Langmuir isotherm relates to surface concentration (Eq. 10), while the data collected are surface pressures, and so there is an inherent assumption made that surface pressure is directly proportional to surface concentration.

Based on these observations, W_1 surface adsorption appears to be dominated by the rate of diffusion to the surface, and decreasing availability of free space as the protein accumulates, with only minor contributions from interactions between proteins at the surface and steric hindrance. Though surface denaturation is likely, it may occur simultaneously with adsorption rather than being a slow process. Although a value for the adsorption constant was estimated, this is not meaningful because of the normalization of the data, but was given for reproducibility of the curve. This model is consistent with the inability of W_1 monomers to interlock with one another to form fibres and the observation that W_1 surface layers do not have the same viscoelastic behaviour as those formed by W_2. Formation of a viscoelastic surface layer by W_2, but not W_1 implies that this property results from an interlocking network of W_2 proteins across the surface. W_1 proteins may interact, but are free to diffuse across the surface, and so the surface layer is not rigid.

Assembly of silk proteins at the air-water interface may be a model for understanding protein assembly during fibre formation as dragline [118] and silkworm fibroin [119] silk proteins adsorbed to the air water interface form β-sheet conformations. For hand-drawn $W_{2\text{-}4}$ fibres, more fibres can be pulled from solution after longer incubation time with a protein concentration of ~20 μM [82], which is roughly 10x the concentration used to track W_1 interfacial assembly in this study. Since surface pressure reached ~75% of the maximum within 1 min of incubation at 2.25 μM, it is unlikely that the affect of incubation time on yield of hand-drawn fibres is due to saturation of the surface. It may instead be due to maturation and alignment of proteins at the surface layer or the formation of sub-layers, which would increase the number of proteins arranged in a pre-fibrillar state which can be converted to fibre by the shear force induced by pulling. Additionally, the formation of fibres by drawing from the solution surface forms a funnel like shape with the silk proteins presumably aligned parallel to the outer surface, which may mimic the narrowing of the spinning duct.

4.2 Nanoparticle Formation by Recombinant AcSp1

Nanoparticles were formed by both salting-out and desolvation. However, nanoparticles rapidly aggregated at high concentrations of potassium phosphate and under aqueous conditions in general. For these reasons, only the desolvation method was pursued for further study because the particles could be formed and stored in the alcohol solutions with greater stability. Nanoparticles were formed by desolvation using ethanol, which resulted in diameters of less than 200 nm as observed by SEM (Figure 18) and DLS (Figure 20). The morphology of these particles by SEM (Figure 18) was a defined spherical shape, with apparent aggregation and fusion. This morphology is consistent with that of other silk nanoparticles observed by SEM [156, 163, 167, 172], particularly with the caveat that some aggregation is expected due to the drying process.

Interestingly, the W_1 particles produced in ethanol are much better defined than those produced in methanol, which are more congealed. Ethanol and methanol are chemically similar, so it appears that the length of the alkyl chain of the alcohol is modulating particle morphology, possibly by stabilizing hydrophobic surfaces of the nanoparticles with increased chain length. This would also explain the apparent stability and lack of macroscopic aggregation of W_1 nanoparticles in ethanol solutions compared to bulk aggregation in aqueous solutions. However, the W_1 particles do appear to coagulate in ethanol over time based the appearance of larger aggregates after several minutes (Figure 19). This may be due to the particles beginning to settle towards the bottom of the cuvette, as particles fully settle-out to form a white layer after several hours, and can be resuspended by vortexing without any visible aggregation.

In considering the effect of ethanol concentration upon W_1 particle properties, the size distributions observed by DLS demonstrate a shoulder of larger particles formed in ~91% ethanol compared to those at lower concentrations, but no notable difference between the distributions formed at the lower ethanol concentrations (Figure 20). This may suggest that a minimum amount of hydration is needed to control aggregation. The larger size of particles formed in ~91% ethanol observed by DLS (Figure 20) compared to SEM (Figure 18) may be due to swelling of the particles while in solution.

W_1 nanoparticles exhibit a characteristic [188] β-sheet appearance by far-UV CD spectroscopy, with a single negative band at ~220 to 225 nm and positive band at ~198 nm (Figure 21). There is a slight tendency for the negative band to occur at a shorter wavelength in

methanol than in ethanol, and with a lower overall intensity (Figure 21). This suggests that β-sheet content is lower overall in methanol compared to ethanol, which is consistent with the hypothesis that ethanol better stabilizes the hydrophobic surfaces of the nanoparticles. Considering tryptophan fluorescence, the tryptophan residues of the W_1 variants are still well exposed to solvent in the nanoparticle state, as evidenced by emission maxima in a narrow range between 343 to 347 nm (Table 2). One explanation for this behaviour is that these residues are at the particle surface. However, the maxima of the W_1 variants are broad compared to the heptapeptide control, which is consistent with a situation where some proteins area on the interior of the particle and others on the surface. It is also possible that nanoparticles are packed loosely enough to be penetrated by solvent molecules to some depth. In a sample of Y169W nanoparticles which was prepared in ethanol and concentrated by air drying, the maximum is slightly blue shifted which suggests that aggregation occurred during the drying process due to concentration of the particles.

4.3 Future Directions

The surface assembly of $W_{2\text{-}4}$ should be investigated to determine the visco-elastic properties of the surface layer and the conformation of the protein at the surface. Secondary structure of the protein at the liquid-air interface could be differentiated from that in bulk solution by external reflection Fourier transform infrared spectroscopy [216]. Micellar assembly by $W_{1\text{-}4}$ containing the C and N terminal domains should also be probed to determine if the terminal domains are required for more consistent and reproducible micelle-like behaviour. The effect of higher concentrations of potassium phosphate on micellization should also be investigated, as this can induce micelle formation for some silk proteins [74].

The stability of nanoparticles in solutions of osmolytes such as glucose used as cryoprotectants after resuspension and in ethanol should be determined. Nanoparticles formed by $W_{2\text{-}4}$ should be studied and compared with W_1 nanoparticles, as the potential for interlocking of W-units in larger constructs upon self-assembly may improve particle properties and stability. Factors affecting aciniform spidroin nanoparticle production that have yet been investigated include mixing rate, protein concentration and effects of other solvents such as acetone or DMSO. For the mixing method, solvent may be added slowly to a protein solution until the concentration is enough to precipitate nanoparticles, or protein solution can be added dropwise

with stirring to a solution of solvent at some concentration. Other methodologies to form aciniform nanoparticles, such as those discussed in section 1.5.3, could also be investigated. In short, W_1 nanoparticles have drug-loading potential [91], but drug uptake and release by W_1 nanoparticles has not yet been investigated and neither has the cellular uptake and biocompatibility of these particles.

4.4 Conclusions

The repeat unit of aciniform silk (W_1) was investigated with respect to its self-assembly into micelle-like aggregates and adsorption at the liquid-air interface. It was determined that while W_1 forms micelle-like nanoparticles, these are low in number. It is not clear how this relates to the native AcSp1 protein, as the non-repetitive terminal domains are absent from W_1, and these domains are generally responsible for dimerization or oligomerization of silk proteins [23, 38, 47]. However, the formation of particles shows that some weak interaction occurs between W_1 monomers, and these may play a larger role in the native protein in which at least 14 repeats are present. Therefore, other recombinant AcSp1 constructs warrant investigation. The thermal precipitation of the R36W variant that coincides with the denaturation of helix-5, and the binding of pyrene to the surface below helix-5 support the hypothesis that hydrophobic interactions with the surface below helix-5 could be involved in conformational changes of W_1 relevant to fibre formation. Specifically, The W_1 protein assembles at the liquid-air interface and this may result in a change in the conformation of the protein that could be reflective of early conformational changes in the fibrillogenic pathway. The greater viscoelastic properties of W_2 at the liquid-air interface suggest that a parallel alignment of the protein monomers occurs, which may be similar to that which occurs in the spinning gland [66, 67].

Nanoparticles of W_1 were formed best by desolvation which resulted in particles of <200 nm in diameter with a β-sheet-like conformation, representing a novel biomaterial form for aciniform-based proteins. The β-sheet content is seemingly solvent dependent, with nanoparticles in ethanol and methanol showing different band wavelengths with lower intensity overall for methanol samples. Nanoparticles were most stable in the alcohol solutions in which they were produced, while highly unstable in aqueous solutions. They were difficult to resuspend and required lyophilization with cryoprotectant rather than the centrifugation methods

commonly used. Nanoparticles of W_1 and other aciniform silk constructs warrant further investigation and optimization.

Bibliography

1. Sutherland, T.D., et al., *Insect silk: one name, many materials.* Annu Rev Entomol, 2010. **55**: p. 171-88.

2. Zhou, C.Z., et al., *Silk fibroin: structural implications of a remarkable amino acid sequence.* Proteins, 2001. **44**(2): p. 119-22.

3. Inoue, S., et al., *Silk fibroin of Bombyx mori is secreted, assembling a high molecular mass elementary unit consisting of H-chain, L-chain, and P25, with a 6:6:1 molar ratio.* J Biol Chem, 2000. **275**(51): p. 40517-28.

4. Mondal, M., K. Trivedy, and S.N. Kumar, *The silk proteins, sericin and fibroin in silkworm, Bombyx mori Linn., - a review.* Caspian J. Env. Sci., 2007. **5**(2): p. 63-76.

5. Eisoldt, L., A. Smith, and T. Scheibel, *Decoding the secrets of spider silk.* Materials Today, 2011. **14**(3): p. 80-86.

6. Blamires, S.J., T.A. Blackledge, and I.M. Tso, *Physicochemical Property Variation in Spider Silk: Ecology, Evolution, and Synthetic Production.* Annu Rev Entomol, 2017. **62**: p. 443-460.

7. Coddington, J.A. and H.W. Levi, *Systematics and Evolution of Spiders (Araneae).* Annual Review of Ecology and Systematics, 1991. **22**(1): p. 565-592.

8. Xu, M. and R.V. Lewis, *Structure of a protein superfiber: spider dragline silk.* Proc Natl Acad Sci U S A, 1990. **87**(18): p. 7120-4.

9. Hinman, M.B. and R.V. Lewis, *Isolation of a clone encoding a second dragline silk fibroin. Nephila clavipes dragline silk is a two-protein fiber.* J. Biol. Chem., 1992. **267**(27): p. 19320-19324.

10. Huemmerich, D., et al., *Novel assembly properties of recombinant spider dragline silk proteins.* Curr Biol, 2004. **14**(22): p. 2070-4.

11. Blasingame, E., et al., *Pyriform spidroin 1, a novel member of the silk gene family that anchors dragline silk fibers in attachment discs of the black widow spider, Latrodectus hesperus.* J Biol Chem, 2009. **284**(42): p. 29097-108.

12. Geurts, P., et al., *Synthetic spider silk fibers spun from Pyriform Spidroin 2, a glue silk protein discovered in orb-weaving spider attachment discs.* Biomacromolecules, 2010. **11**(12): p. 3495-503.

13. Collin, M.A., et al., *Evidence from Multiple Species that Spider Silk Glue Component ASG2 is a Spidroin.* Sci Rep, 2016. **6**: p. 21589.

14. Hayashi, C.Y., T.A. Blackledge, and R.V. Lewis, *Molecular and mechanical characterization of aciniform silk: uniformity of iterated sequence modules in a novel member of the spider silk fibroin gene family.* Mol Biol Evol, 2004. **21**(10): p. 1950-9.

15. Tian, M. and R.V. Lewis, *Molecular characterization and evolutionary study of spider tubuliform (eggcase) silk protein.* Biochemistry, 2005. **44**(22): p. 8006-12.

16. Zhao, A.C., et al., *Novel molecular and mechanical properties of egg case silk from wasp spider, Argiope bruennichi.* Biochemistry, 2006. **45**(10): p. 3348-56.

17. Wang, S.P., et al., *Structural analysis of fibroin heavy chain signal peptide of silkworm Bombyx mori.* Acta Biochim Biophys Sin (Shanghai), 2006. **38**(7): p. 507-13.

18. Tanaka, K., et al., *Determination of the site of disulfide linkage between heavy and light chains of silk fibroin produced by Bombyx mori.* Biochimica et Biophysica Acta (BBA) - Protein Structure and Molecular Enzymology, 1999. **1432**(1): p. 92-103.

19. Yamaguchi, K., et al., *Primary structure of the silk fibroin light chain determined by cDNA sequencing and peptide analysis.* Journal of Molecular Biology, 1989. **210**(1): p. 127-139.

20. Garb, J.E., N.A. Ayoub, and C.Y. Hayashi, *Untangling spider silk evolution with spidroin terminal domains.* BMC Evol Biol, 2010. **10**: p. 243.

21. Lin, Z., et al., *Solution structure of eggcase silk protein and its implications for silk fiber formation.* Proc Natl Acad Sci U S A, 2009. **106**(22): p. 8906-11.

22. Rising, A., et al., *N-terminal nonrepetitive domain common to dragline, flagelliform, and cylindriform spider silk proteins.* Biomacromolecules, 2006. **7**(11): p. 3120-4.

23. Hagn, F., et al., *pH-dependent dimerization and salt-dependent stabilization of the N-terminal domain of spider dragline silk--implications for fiber formation.* Angew Chem Int Ed Engl, 2011. **50**(1): p. 310-3.

24. Ayoub, N.A., et al., *Blueprint for a high-performance biomaterial: full-length spider dragline silk genes.* PLoS One, 2007. **2**(6): p. e514.

25. Zhang, Y., et al., *The molecular structures of major ampullate silk proteins of the wasp spider, Argiope bruennichi: a second blueprint for synthesizing de novo silk.* Comp Biochem Physiol B Biochem Mol Biol, 2013. **164**(3): p. 151-8.

26. Chen, G., et al., *Full-length minor ampullate spidroin gene sequence.* PLoS One, 2012. **7**(12): p. e52293.

27. Hayashi, C.Y. and R.V. Lewis, *Spider flagelliform silk: lessons in protein design, gene structure, and molecular evolution.* Bioessays, 2001. **23**(8): p. 750-6.

28. Chaw, R.C., C.A. Saski, and C.Y. Hayashi, *Complete gene sequence of spider attachment silk protein (PySp1) reveals novel linker regions and extreme repeat homogenization.* Insect Biochem Mol Biol, 2017. **81**: p. 80-90.

29. Nova, A., et al., *Molecular and nanostructural mechanisms of deformation, strength and toughness of spider silk fibrils.* Nano Lett, 2010. **10**(7): p. 2626-34.

30. Monti, P., et al., *Raman spectroscopic characterization ofBombyx mori silk fibroin: Raman spectrum of Silk I.* Journal of Raman Spectroscopy, 2001. **32**(2): p. 103-107.

31. Asakura, T., K. Okushita, and M.P. Williamson, *Analysis of the structure of bombyx mori silk fibroin by NMR.* Macromolecules, 2015. **48**(8): p. 2345-2357.

32. Simmons, A.H., C.A. Michal, and L.W. Jelinski, *Molecular orientation and two-component nature of the crystalline fraction of spider dragline silk.* Science, 1996. **271**(5245): p. 84-7.

33. Romer, L. and T. Scheibel, *The elaborate structure of spider silk: structure and function of a natural high performance fiber.* Prion, 2008. **2**(4): p. 154-61.

34. Rousseau, M.E., T. Lefevre, and M. Pezolet, *Conformation and orientation of proteins in various types of silk fibers produced by Nephila clavipes spiders.* Biomacromolecules, 2009. **10**(10): p. 2945-53.

35. Creager, M.S., et al., *Solid-state NMR comparison of various spiders' dragline silk fiber.* Biomacromolecules, 2010. **11**(8): p. 2039-43.

36. Blackledge, T.A., et al., *How super is supercontraction? Persistent versus cyclic responses to humidity in spider dragline silk.* J Exp Biol, 2009. **212**(Pt 13): p. 1981-9.

37. Lefevre, T., et al., *Conformational and orientational transformation of silk proteins in the major ampullate gland of Nephila clavipes spiders.* Biomacromolecules, 2008. **9**(9): p. 2399-407.

38. He, Y.X., et al., *N-Terminal domain of Bombyx mori fibroin mediates the assembly of silk in response to pH decrease.* J Mol Biol, 2012. **418**(3-4): p. 197-207.

39. Dicko, C., F. Vollrath, and J.M. Kenney, *Spider silk protein refolding is controlled by changing pH.* Biomacromolecules, 2004. **5**(3): p. 704-10.

40. Oster, C., et al., *Characterization and assembly of a GFP-tagged cylindriform silk into hexameric complexes.* Biopolymers, 2014. **101**(4): p. 378-90.

41. Lefevre, T., et al., *In situ conformation of spider silk proteins in the intact major ampullate gland and in solution.* Biomacromolecules, 2007. **8**(8): p. 2342-4.

42. Adzhubei, A.A., M.J. Sternberg, and A.A. Makarov, *Polyproline-II helix in proteins: structure and function.* J Mol Biol, 2013. **425**(12): p. 2100-32.

43. Lefevre, T., et al., *Diversity of molecular transformations involved in the formation of spider silks.* J Mol Biol, 2011. **405**(1): p. 238-53.

44. Hayashi, C.Y., N.H. Shipley, and R.V. Lewis, *Hypotheses that correlate the sequence, structure, and mechanical properties of spider silk proteins.* International Journal of Biological Macromolecules, 1999. **24**(2-3): p. 271-275.

45. Pal, L., G. Basu, and P. Chakrabarti, *Variants of 3(10)-helices in proteins.* Proteins, 2002. **48**(3): p. 571-9.

46. Hagn, F., et al., *A conserved spider silk domain acts as a molecular switch that controls fibre assembly.* Nature, 2010. **465**(7295): p. 239-42.

47. Wang, S., W. Huang, and D. Yang, *Structure and function of C-terminal domain of aciniform spidroin.* Biomacromolecules, 2014. **15**(2): p. 468-77.

48. Wang, S., W. Huang, and D. Yang, *NMR structure note: repetitive domain of aciniform spidroin 1 from Nephila antipodiana.* J Biomol NMR, 2012. **54**(4): p. 415-20.

49. Tremblay, M.L., et al., *Spider wrapping silk fibre architecture arising from its modular soluble protein precursor.* Sci Rep, 2015. **5**: p. 11502.

50. Simmons, J.R., L. Xu, and J.K. Rainey, *Recombinant Pyriform Silk Fiber Mechanics Are Modulated by Wet-Spinning Conditions.* ACS Biomaterials Science & Engineering, 2019. **5**(10): p. 4985-4993.

51. Blackledge, T.A. and C.Y. Hayashi, *Silken toolkits: biomechanics of silk fibers spun by the orb web spider Argiope argentata (Fabricius 1775).* J Exp Biol, 2006. **209**(Pt 13): p. 2452-61.

52. Hinman, M.B., J.A. Jones, and R.V. Lewis, *Synthetic spider silk: a modular fiber.* Trends in Biotechnology, 2000. **18**(9): p. 374-379.

53. Meinel, L., et al., *The inflammatory responses to silk films in vitro and in vivo.* Biomaterials, 2005. **26**(2): p. 147-55.

54. Kim, J.H., et al., *Preparation and in vivo degradation of controlled biodegradability of electrospun silk fibroin nanofiber mats.* J Biomed Mater Res A, 2012. **100**(12): p. 3287-95.

55. Maitz, M.F., et al., *Biocompatibility assessment of silk nanoparticles: hemocompatibility and internalization by human blood cells.* Nanomedicine, 2017. **13**(8): p. 2633-2642.

56. Koh, L.-D., et al., *Structures, mechanical properties and applications of silk fibroin materials.* Progress in Polymer Science, 2015. **46**: p. 86-110.

57. Spiess, K., A. Lammel, and T. Scheibel, *Recombinant spider silk proteins for applications in biomaterials.* Macromol Biosci, 2010. **10**(9): p. 998-1007.

58. Jewell, M., et al., *The development of SERI(R) Surgical Scaffold, an engineered biological scaffold.* Ann N Y Acad Sci, 2015. **1358**: p. 44-55.

59. Hardy, J.G., L.M. Römer, and T.R. Scheibel, *Polymeric materials based on silk proteins.* Polymer, 2008. **49**(20): p. 4309-4327.

60. Tao, H., D.L. Kaplan, and F.G. Omenetto, *Silk materials--a road to sustainable high technology.* Adv Mater, 2012. **24**(21): p. 2824-37.

61. Zhou, Z., et al., *The Use of Functionalized Silk Fibroin Films as a Platform for Optical Diffraction-Based Sensing Applications.* Adv Mater, 2017. **29**(15).

62. Wang, C., et al., *Silk nanofibers as high efficient and lightweight air filter.* Nano Research, 2016. **9**(9): p. 2590-2597.

63. Aigner, T. and T. Scheibel, *Self-Rolling Refillable Tubular Enzyme Containers Made of Recombinant Spider Silk and Chitosan.* ACS Appl Mater Interfaces, 2019. **11**(17): p. 15290-15297.

64. Vollrath, F. and D.P. Knight, *Liquid crystalline spinning of spider silk.* Nature, 2001. **410**(6828): p. 541-8.

65. Andersson, M., J. Johansson, and A. Rising, *Silk Spinning in Silkworms and Spiders.* Int J Mol Sci, 2016. **17**(8).

66. Knight, D.P. and F. Vollrath, *Liquid crystals and flow elongation in a spider's silk production line.* Proceedings of the Royal Society of London. Series B: Biological Sciences, 1999. **266**(1418): p. 519-523.

67. Asakura, T., et al., *Some observations on the structure and function of the spinning apparatus in the silkworm Bombyx mori.* Biomacromolecules, 2007. **8**(1): p. 175-81.

68. Evans, D.F., *Self-organization of amphiphiles.* Langmuir, 1988. **4**(1): p. 3-12.

69. Jin, H.J. and D.L. Kaplan, *Mechanism of silk processing in insects and spiders.* Nature, 2003. **424**(6952): p. 1057-61.

70. Parent, L.R., et al., *Hierarchical spidroin micellar nanoparticles as the fundamental precursors of spider silks.* Proc Natl Acad Sci U S A, 2018. **115**(45): p. 11507-11512.

71. Domigan, L.J., et al., *Carbonic anhydrase generates a pH gradient in Bombyx mori silk glands.* Insect Biochem Mol Biol, 2015. **65**: p. 100-6.

72. Andersson, M., et al., *Carbonic anhydrase generates CO2 and H+ that drive spider silk formation via opposite effects on the terminal domains.* PLoS Biol, 2014. **12**(8): p. e1001921.

73. Heim, M., D. Keerl, and T. Scheibel, *Spider silk: from soluble protein to extraordinary fiber.* Angew Chem Int Ed Engl, 2009. **48**(20): p. 3584-96.

74. Slotta, U.K., et al., *An engineered spider silk protein forms microspheres.* Angew Chem Int Ed Engl, 2008. **47**(24): p. 4592-4.

75. Rammensee, S., et al., *Assembly mechanism of recombinant spider silk proteins.* Proc Natl Acad Sci U S A, 2008. **105**(18): p. 6590-5.

76. Breslauer, D.N., L.P. Lee, and S.J. Muller, *Simulation of flow in the silk gland.* Biomacromolecules, 2009. **10**(1): p. 49-57.

77. Frounfelker, B.D., et al., *Persistence of birefringence in sheared solutions of wormlike micelles.* Langmuir, 2009. **25**(1): p. 167-72.

78. Shimada, T., et al., *Wormlike micelle formation in peptide-lipid conjugates driven by secondary structure transformation of the headgroups.* J Phys Chem B, 2009. **113**(42): p. 13711-4.

79. Shimada, T., et al., *Self-assembly process of peptide amphiphile worm-like micelles.* J Phys Chem B, 2012. **116**(1): p. 240-3.

80. Lu, Q., et al., *Silk self-assembly mechanisms and control from thermodynamics to kinetics.* Biomacromolecules, 2012. **13**(3): p. 826-32.

81. Rousseau, M.E., et al., *Characterization by Raman microspectroscopy of the strain-induced conformational transition in fibroin fibers from the silkworm Samia cynthia ricini.* Biomacromolecules, 2006. **7**(9): p. 2512-21.

82. Xu, L., et al., *Recombinant minimalist spider wrapping silk proteins capable of native-like fiber formation.* PLoS One, 2012. **7**(11): p. e50227.

83. Xu, L., et al., *1H, 13C and 15N NMR assignments of the aciniform spidroin (AcSp1) repetitive domain of Argiope trifasciata wrapping silk.* Biomol NMR Assign, 2012. **6**(2): p. 147-51.

84. Tremblay, M.L., et al., *Characterizing Aciniform Silk Repetitive Domain Backbone Dynamics and Hydrodynamic Modularity.* Int J Mol Sci, 2016. **17**(8).

85. Bodenhausen, G. and D.J. Ruben, *Natural abundance nitrogen-15 NMR by enhanced heteronuclear spectroscopy.* Chem. Phys. Lett, 1980. **69**(1): p. 185-189.

86. KEEPERS, J.W. and T.L. JAMES, *A theoretical study of distance determinations from NMR. two-dimensional nuclear overhauser effect spectra.* J. Magn. Reson, 1984. **57**: p. 404-426.

87. Kay, L.E., D.A. Torchia, and A. Bax, *Backbone dynamics of proteins as studied by 15N inverse detected heteronuclear NMR spectroscopy: application to staphylococcal nuclease.* Biochemistry, 1989. **28**(23): p. 8972-9.

88. Peng, J.W. and G. Wagner, *Investigation of protein motions via relaxation measurements.* Methods Enzymol, 1994. **239**: p. 563-596.

89. Sarker, M., et al., *Tracking Transitions in Spider Wrapping Silk Conformation and Dynamics by (19)F Nuclear Magnetic Resonance Spectroscopy.* Biochemistry, 2016. **55**(21): p. 3048-59.

90. Dyson, H.J., P.E. Wright, and H.A. Scheraga, *The role of hydrophobic interactions in initiation and propagation of protein folding.* PNAS, 2006. **103**(35): p. 13057-13061.

91. Xu, L., et al., *Nanoparticle self-assembly by a highly stable recombinant spider wrapping silk protein subunit.* FEBS Lett, 2013. **587**(19): p. 3273-80.

92. Royer, C.A., *Probing protein folding and conformational transitions with fluorescence.* Chem. Rev. , 2006. **106**: p. 1769-1784.

93. Dahanayake, J.N., et al., *Progress in Our Understanding of 19F Chemical Shifts*. 2018. p. 281-365.

94. Palmer, A.G., C.D. Kroenke, and J.P. Loria, *Nuclear magnetic resonance methods for quantifying microsecond-to-millisecond motions in biological macromolecules.* Methods in enzymology, 2001. **339**: p. 204-238.

95. Weatherbee-Martin, N., et al., *Identification of Wet-Spinning and Post-Spin Stretching Methods Amenable to Recombinant Spider Aciniform Silk.* Biomacromolecules, 2016. **17**(8): p. 2737-46.

96. Xu, L., et al., *Recombinant silk fiber properties correlate to prefibrillar self-assembly.* Small, 2019. **15**(12): p. e1805294.

97. Hawe, A., M. Sutter, and W. Jiskoot, *Extrinsic fluorescent dyes as tools for protein characterization.* Pharm Res, 2008. **25**(7): p. 1487-99.

98. Basu Ray, G., I. Chakraborty, and S.P. Moulik, *Pyrene absorption can be a convenient method for probing critical micellar concentration (cmc) and indexing micellar polarity.* J Colloid Interface Sci, 2006. **294**(1): p. 248-54.

99. Kalyanasundaram, K. and J.K. Thomas, *Environmental effects on vibronic band intensities in pyrene monomer fluorescence and their application in studies of micellar systems.* Journal of the American Chemical Society, 1977. **99**(7): p. 2039-2044.

100. Ruckenstein, E. and R. Nagarajan, *Critical micelle concentration. Transition point for micellar size distribution.* J. Phys. Chem., 1975. **79**(24): p. 2622-2626.

101. Ananthapadmanabhan, K.P., et al., *Fluorescence probes for critical micelle concentration.* Langmuir, 1985. **1**: p. 352-355.

102. Vincent, B., *McBain and the centenary of the micelle.* Adv Colloid Interface Sci, 2014. **203**: p. 51-4.

103. Danov, K.D., et al., *Growth of wormlike micelles in nonionic surfactant solutions: Quantitative theory vs. experiment.* Adv Colloid Interface Sci, 2018. **256**: p. 1-22.

104. Tanford, C., *Theory of micelle formation in aqueous solution.* J. Phys. Chem., 1974. **78**(24): p. 2469-2479.

105. Hamann, S.D., *The dependence of the free energy of micelle formation on aggregation number and critical micelle concentration.* Aust. J. Chem., 1978. **31**: p. 919-921.

106. Phillips, J.N., *The energetics of micelle formation.* Transactions of the Faraday Society, 1955. **51**.

107. Sarac, B., M. Bester-Rogac, and J. Lah, *Thermodynamics of micellization from heat-capacity measurements.* Chemphyschem, 2014. **15**(9): p. 1827-33.

108. Rosenholm, J.B., T.E. Burchfield, and L.G. Hepler, *Thermodynamics of micelle formation: Standard states, temperature dependence of the critical micelle concentration, and thermal expansion of the solvent.* Journal of Colloid and Interface Science, 1980. **78**(1): p. 191-194.

109. Eastoe, J. and J.S. Dalton, *Dynamic surface tension and adsorption mechanisms of surfactants at the air–water interface.* Advances in Colloid and Interface Science, 2000. **85**(2-3): p. 103-144.

110. Ayawei, N., A.N. Ebelegi, and D. Wankasi, *Modelling and Interpretation of Adsorption Isotherms.* Journal of Chemistry, 2017. **2017**: p. 1-11.

111. Benjamins, J. and J.A. De Feijter, *Dynamic and static properties of proteins adsorbed at the air water interface.* Faraday Discuss Chem Soc, 1975. **59**: p. 218-29.

112. Qian, J., et al., *Nanofiber micelles from the self-assembly of block copolymers.* Trends Biotechnol, 2010. **28**(2): p. 84-92.

113. Latour, R.A., *The Langmuir isotherm: a commonly applied but misleading approach for the analysis of protein adsorption behavior.* J Biomed Mater Res A, 2015. **103**(3): p. 949-58.

114. Malmsten, M., *Formation of Adsorbed Protein Layers.* J Colloid Interface Sci, 1998. **207**(2): p. 186-199.

115. Fainerman, V.B., E.H. Lucassen-Reynders, and R. Miller, *Description of the adsorption behaviour of proteins at water/fluid interfaces in the framework of a two-dimensional solution model.* Advances in Colloid and Interface Science, 2003. **106**(1-3): p. 237-259.

116. Razumovsky, L. and S. Damodaran, *Surface Activity−Compressibility Relationship of Proteins at the Air−Water Interface.* Langmuir, 1999. **15**(4): p. 1392-1399.

117. Leiske, D.L., I.C. Shieh, and M.L. Tse, *A Method To Measure Protein Unfolding at an Air-Liquid Interface.* Langmuir, 2016. **32**(39): p. 9930-9937.

118. Renault, A., et al., *Surface properties and conformation of Nephila clavipes spider recombinant silk proteins at the air-water interface.* Langmuir, 2009. **25**(14): p. 8170-80.

119. Yang, Y., et al., *Behavior of silk protein at the air–water interface.* Soft Matter, 2012. **8**(37).

120. Wang, L., et al., *Interfacial rheology of natural silk fibroin at air/water and oil/water interfaces.* Langmuir, 2012. **28**(1): p. 459-67.

121. Liao, Z., et al., *Protein assembly at the air-water interface studied by fluorescence microscopy.* Langmuir, 2011. **27**(21): p. 12775-81.

122. Shi, J., et al., *Cancer nanomedicine: progress, challenges and opportunities.* Nat Rev Cancer, 2017. **17**(1): p. 20-37.

123. Zhu, Y. and L. Liao, *Applications of Nanoparticles for Anticancer Drug Delivery: A Review.* Journal of Nanoscience and Nanotechnology, 2015. **15**(7): p. 4753-4773.

124. Wu, Y., et al., *Gold nanoparticles in biological optical imaging.* Nano Today, 2019. **24**: p. 120-140.

125. Bobo, D., et al., *Nanoparticle-Based Medicines: A Review of FDA-Approved Materials and Clinical Trials to Date.* Pharm Res, 2016. **33**(10): p. 2373-87.

126. Blanco, E., H. Shen, and M. Ferrari, *Principles of nanoparticle design for overcoming biological barriers to drug delivery.* Nat Biotechnol, 2015. **33**(9): p. 941-51.

127. Bertrand, N., et al., *Cancer nanotechnology: the impact of passive and active targeting in the era of modern cancer biology.* Adv Drug Deliv Rev, 2014. **66**: p. 2-25.

128. Matsumura, Y. and H. Maeda, *A New Concept for Macromolecular Therapeutics in Cancer Chemotherapy: Mechanism of Tumoritropic Accumulation of Proteins and the Antitumor Agent Smancs.* Cancer Res. , 1986. **46**(12): p. 6387-6392.

129. HOBBS, S.K., et al., *Regulation of transport pathways in tumor vessels: Role of tumor type and microenvironment.* Proc. Natl. Acad. Sci. USA, 1998. **95**: p. 4607–4612.

130. Leu, A.J., et al., *Absence of functional lymphatics within a murine sarcoma: a molecular and functional evaluation.* Cancer Res, 2000. **60**: p. 4324-27.

131. Moghimi, S.M. and H.M. Patel, *Serum-mediated recognition of liposomes by phagocytic cells of the reticuloendothelial system – the concept of tissue specificity.* Adv Drug Deliv Rev, 1998. **32**: p. 45-60.

132. Tenzer, S., et al., *Rapid formation of plasma protein corona critically affects nanoparticle pathophysiology.* Nat Nanotechnol, 2013. **8**(10): p. 772-81.

133. Suk, J.S., et al., *PEGylation as a strategy for improving nanoparticle-based drug and gene delivery.* Adv Drug Deliv Rev, 2016. **99**(Pt A): p. 28-51.

134. Kim, S.Y., et al., *Formulation of Biologically-Inspired Silk-Based Drug Carriers for Pulmonary Delivery Targeted for Lung Cancer.* Sci Rep, 2015. **5**: p. 11878.

135. Takeuchi, I., et al., *Transdermal delivery of 40-nm silk fibroin nanoparticles.* Colloids Surf B Biointerfaces, 2019. **175**: p. 564-568.

136. Wu, J., et al., *Oral Delivery of Curcumin Using Silk Nano- and Microparticles.* ACS Biomaterials Science & Engineering, 2018. **4**(11): p. 3885-3894.

137. Hrkach, J., et al., *Preclinical development and clinical translation of a PSMA-targeted docetaxel nanoparticle with a differentiated pharmacological profile.* Sci Transl Med, 2012. **4**(128): p. 128ra39.

138. Sahay, G., D.Y. Alakhova, and A.V. Kabanov, *Endocytosis of nanomedicines.* J Control Release, 2010. **145**(3): p. 182-95.

139. Du, J.Z., et al., *Tailor-made dual pH-sensitive polymer-doxorubicin nanoparticles for efficient anticancer drug delivery.* J Am Chem Soc, 2011. **133**(44): p. 17560-3.

140. Su, J., et al., *Catechol polymers for pH-responsive, targeted drug delivery to cancer cells.* J Am Chem Soc, 2011. **133**(31): p. 11850-3.

141. K, C.R., B. Thapa, and P. Xu, *pH and redox dual responsive nanoparticle for nuclear targeted drug delivery.* Mol Pharm, 2012. **9**(9): p. 2719-29.

142. Sonavane, G., K. Tomoda, and K. Makino, *Biodistribution of colloidal gold nanoparticles after intravenous administration: effect of particle size.* Colloids Surf B Biointerfaces, 2008. **66**(2): p. 274-80.

143. Decuzzi, P., et al., *Intravascular delivery of particulate systems: does geometry really matter?* Pharm Res, 2009. **26**(1): p. 235-43.

144. Arvizo, R.R., et al., *Modulating pharmacokinetics, tumor uptake and biodistribution by engineered nanoparticles.* PLoS One, 2011. **6**(9): p. e24374.

145. Hansen, A.E., et al., *Positron Emission Tomography Based Elucidation of the Enhanced Permeability and Retention Effect in Dogs with Cancer Using Copper-64 Liposomes.* ACS Nano, 2015. **9**(7): p. 6985-95.

146. Kucharczyk, K., et al., *Bioengineering the spider silk sequence to modify its affinity for drugs.* Int J Nanomedicine, 2018. **13**: p. 4247-4261.

147. Philipp Seib, F., *Silk nanoparticles—an emerging anticancer nanomedicine.* AIMS Bioengineering, 2017. **4**(2): p. 239-258.

148. Mottaghitalab, F., et al., *Silk fibroin nanoparticle as a novel drug delivery system.* J Control Release, 2015. **206**: p. 161-76.

149. Numata, K. and D.L. Kaplan, *Silk-based delivery systems of bioactive molecules.* Adv Drug Deliv Rev, 2010. **62**(15): p. 1497-508.

150. Lohcharoenkal, W., et al., *Protein nanoparticles as drug delivery carriers for cancer therapy.* Biomed Res Int, 2014. **2014**: p. 180549.

151. Sun, N., et al., *Fabricated porous silk fibroin particles for pH-responsive drug delivery and targeting of tumor cells.* Journal of Materials Science, 2018. **54**(4): p. 3319-3330.

152. Seib, F.P., et al., *pH-dependent anticancer drug release from silk nanoparticles.* Adv Healthc Mater, 2013. **2**(12): p. 1606-11.

153. Wongpinyochit, T., et al., *PEGylated Silk Nanoparticles for Anticancer Drug Delivery.* Biomacromolecules, 2015. **16**(11): p. 3712-22.

154. Vishal Gupta, A.A., Carmen N. Ríos, Bharat B. Aggarwal, Anshu B. Mathur, *Fabrication and characterization of silk fibroin-derived curcumin nanoparticles for cancer therapy.* International Journal of Nanomedicine, 2009. **4**: p. 115-122.

155. Kundu, J., et al., *Silk fibroin nanoparticles for cellular uptake and control release.* Int J Pharm, 2010. **388**(1-2): p. 242-50.

156. Wongpinyochit, T., et al., *Microfluidic-assisted silk nanoparticle tuning.* Nanoscale Advances, 2019. **1**(2): p. 873-883.

157. Gobin, A.S., et al., *Silk-fibroin-coated liposomes for long-term and targeted drug delivery.* Int J Nanomedicine, 2006. **1**(1): p. 81-87.

158. Chen, A.Z., et al., *Study of magnetic silk fibroin nanoparticles for massage-like transdermal drug delivery.* Int J Nanomedicine, 2015. **10**: p. 4639-51.

159. Huemmerich, D., U. Slotta, and T. Scheibel, *Processing and modification of films made from recombinant spider silk proteins.* Applied Physics A, 2005. **82**(2): p. 219-222.

160. Hofer, M., G. Winter, and J. Myschik, *Recombinant spider silk particles for controlled delivery of protein drugs.* Biomaterials, 2012. **33**(5): p. 1554-62.

161. Elsner, M.B., et al., *Enhanced cellular uptake of engineered spider silk particles.* Biomater Sci, 2015. **3**(3): p. 543-51.

162. Doblhofer, E. and T. Scheibel, *Engineering of recombinant spider silk proteins allows defined uptake and release of substances.* J Pharm Sci, 2015. **104**(3): p. 988-94.

163. Florczak, A., A. Mackiewicz, and H. Dams-Kozlowska, *Functionalized spider silk spheres as drug carriers for targeted cancer therapy.* Biomacromolecules, 2014. **15**(8): p. 2971-81.

164. Numata, K., et al., *Silk-based nanocomplexes with tumor-homing peptides for tumor-specific gene delivery.* Macromol Biosci, 2012. **12**(1): p. 75-82.

165. Lammel, A.S., et al., *Controlling silk fibroin particle features for drug delivery.* Biomaterials, 2010. **31**(16): p. 4583-91.

166. Lammel, A., et al., *Recombinant spider silk particles as drug delivery vehicles.* Biomaterials, 2011. **32**(8): p. 2233-40.

167. Jastrzebska, K., et al., *Delivery of chemotherapeutics using spheres made of bioengineered spider silks derived from MaSp1 and MaSp2 proteins.* Nanomedicine (Lond.), 2018. **13**(4): p. 439–454.

168. Qu, J., et al., *Silk fibroin nanoparticles prepared by electrospray as controlled release carriers of cisplatin.* Mater Sci Eng C Mater Biol Appl, 2014. **44**: p. 166-74.

169. Wang, X., et al., *Silk nanospheres and microspheres from silk/pva blend films for drug delivery.* Biomaterials, 2010. **31**(6): p. 1025-35.

170. Rodionov, I., N. Abdullah, and D.L. Kaplan, *Microporous Drug-Eluting Large Silk Particles Through Cryo-Granulation.* Advanced Engineering Materials, 2019.

171. Cao, Y., et al., *Drug release from core-shell PVA/silk fibroin nanoparticles fabricated by one-step electrospraying.* Sci Rep, 2017. **7**(1): p. 11913.

172. Florczak, A., et al., *Blending two bioengineered spider silks to develop cancer targeting spheres.* Journal of Materials Chemistry B, 2017. **5**(16): p. 3000-3011.

173. Jastrzebska, K., et al., *The method of purifying bioengineered spider silk determines the silk sphere properties.* Sci Rep, 2016. **6**: p. 28106.

174. Shi, P. and J.C.H. Goh, *Self-assembled silk fibroin particles: Tunable size and appearance.* Powder Technology, 2012. **215-216**: p. 85-90.

175. Arya, N., et al., *Electrospraying: a facile technique for synthesis of chitosan-based micro/nanospheres for drug delivery applications.* J Biomed Mater Res B Appl Biomater, 2009. **88**(1): p. 17-31.

176. Jablonski, A., *Efficiency of anti-stokes fluorescence in dyes.* Nature, 1933. **131**(3319): p. 839-840.

177. So, P.T. and C.Y. Dong, *Fluorescence spectrophotometry*, in *eLS*. 2001.

178. Albani, J.R., *New insights in the interpretation of tryptophan fluorescence : origin of the fluorescence lifetime and characterization of a new fluorescence parameter in proteins: the emission to excitation ratio.* J Fluoresc, 2007. **17**(4): p. 406-17.

179. Sun, F., et al., *Micro-environmental influences on the fluorescence of tryptophan.* Spectrochim Acta A Mol Biomol Spectrosc, 2010. **76**(2): p. 142-5.

180. Wetlaufer, D.B., *Ultraviolet spectra of proteins and amino acids.* Adv. Protein Chem., 1963. **17**: p. 303-390.

181. Pierce, D.W. and S.G. Boxer, *Stark effect spectroscopy of tryptophan.* Biophysical Journal, 1995. **68**(4): p. 1583-1591.

182. Coolidge, A.S., H.M. James, and R.D. Present, *A study of the Franck-Condon principle.* The Journal of Chemical Physics, 1936. **4**(3): p. 193-211.

183. Lakowicz, J.R., *Protein Fluorescence*, in *Principles of Fluorescence Spectroscopy*. 1983, Springer US: Boston, MA. p. 341-381.

184. Főrster, T., *10th Spiers Memorial Lecture. Transfer mechanisms of electronic excitation.* Discuss. Faraday Soc., 1959. **27**(0): p. 7-17.

185. Ghisaidoobe, A.B. and S.J. Chung, *Intrinsic tryptophan fluorescence in the detection and analysis of proteins: a focus on Forster resonance energy transfer techniques.* Int J Mol Sci, 2014. **15**(12): p. 22518-38.

186. Woody, R.W., *Circular dichroism*. Methods Enzymol, 1995. **246**: p. 34-71.

187. Johnson, W.C., Jr., *Secondary structure of proteins through circular dichroism spectroscopy.* Annu Rev Biophys Biophys Chem, 1988. **17**: p. 145-66.

188. Kelly, S.M., T.J. Jess, and N.C. Price, *How to study proteins by circular dichroism.* Biochim Biophys Acta, 2005. **1751**(2): p. 119-39.

189. Tyndall, J., *IV. On the blue colour of the sky, the polarization of skylight, and on the polarization of light by cloudy matter generally.* Proceedings of the Royal Society of London, 1869. **17**: p. 223-233.

190. Strutt, J.W., *XXXVI. On the light from the sky, its polarization and colour.* The London, Edinburgh, and Dublin Philosophical Magazine and Journal of Science, 1871. **41**(273): p. 274-279.

191. Strutt, J.W., *LVIII. On the scattering of light by small particles.* The London, Edinburgh, and Dublin Philosophical Magazine and Journal of Science, 1871. **41**(275): p. 447-454.

192. Mie, G., *Beiträge zur Optik trüber Medien, speziell kolloidaler Metallösungen.* Annalen der Physik, 1908. **330**(3): p. 377-445.

193. B.1. Berne, R.P., *Laser light scattering from liquids.* Annual Review of Physical Chemistry, 1974. **25**: p. 233-253.

194. Uhlenbeck, G.E. and L.S. Ornstein, *On the Theory of the Brownian Motion.* Physical Review, 1930. **36**(5): p. 823-841.

195. Einstein, A., *On the motion of small particles suspended in liquids at rest required by the molecular-kinetic theory of heat.* Annalen der Physik, 1905. **17**: p. 549-560.

196. Stetefeld, J., S.A. McKenna, and T.R. Patel, *Dynamic light scattering: a practical guide and applications in biomedical sciences.* Biophys Rev, 2016. **8**(4): p. 409-427.

197. Young, M.E., P.A. Carroad, and R.L. Bell, *Estimation of diffusion coefficients of proteins.* Biotechnology and Bioengineering, 1980. **22**(5): p. 947-955.

198. Phelps, C.F., *Dynamic light scattering, with application to chemistry, biology and physics.* Biochemical Education, 1977. **5**(1).

199. Harding, S.E. and K. Jumel, *Light scattering.* Curr Protoc Protein Sci, 2001. **Chapter 7**: p. Unit 7 8.

200. Siegert, A., *On the fluctuations in signals returned by many independently moving scatterers*. 1943: Radiation Laboratory, Massachusetts Institute of Technology.

201. Koppel, D.E., *Analysis of macromolecular polydispersity in intensity correlation spectroscopy: the method of cumulants.* The Journal of Chemical Physics, 1972. **57**(11): p. 4814-4820.

202. Morrison, I.D., E.F. Grabowski, and C.A. Herb, *Improved techniques for particle size determination by quasi-elastic light scattering.* Langmuir, 1985. **1**(4): p. 496-501.

203. Provencher, S.W., *A constrained regularization method for inverting data represented by linear algebraic or integral equations.* Computer Physics Communications, 1982. **27**(3): p. 213-227.

204. Scotti, A., et al., *The CONTIN algorithm and its application to determine the size distribution of microgel suspensions.* J Chem Phys, 2015. **142**(23): p. 234905.

205. Wilhelmy, L., *Ueber die abhängigkeit der capillaritäts-constanten des alkohols von substanz und gestalt des benetzten festen körpers.* Annalen der Physik und Chemie, 1863. **195**(6): p. 177-217.

206. Franses, E.I., O.A. Basaran, and C.-H. Chang, *Techniques to measure dynamic surface tension.* Current Opinion in Colloid & Interface Science, 1996. **1**(2): p. 296-303.

207. Smith, K.C.A. and C.W. Oatley, *The scanning electron microscope and its fields of application.* British Journal of Applied Physics, 1955. **6**(11): p. 391-399.

208. McMullan, D., *Scanning electron microscopy 1928-1965.* Scanning, 2006. **17**(3): p. 175-185.

209. Michael A., M.A., J.-J. Orteu, and H.W. Schreier, *Digital Image Correlation (DIC)*, in *Image Correlation for Shape, Motion and Deformation Measurements: Basic Concepts,Theory and Applications*. 2009, Springer US: Boston, MA. p. 1-37.

210. Clay, C.S. and G.W. Peace, *Ion beam sputtering: an improved method of metal coating SEM samples and shadowing CTEM samples.* Journal of Microscopy, 1981. **123**(1): p. 25-34.

211. Shin, K., et al., *Preferential apelin-13 production by the proprotein convertase PCSK3 is implicated in obesity.* FEBS Open Bio, 2013. **3**: p. 328-33.

212. Gururaja, T.L., et al., *A Homogeneous FRET Assay System for Multiubiquitin Chain Assembly and Disassembly.* Methods Enzymol, 2005. **399**: p. 663-682.

213. Chandler, D., *Interfaces and the driving force of hydrophobic assembly.* Nature, 2005. **437**(7059): p. 640-7.

214. Arakawa, T., et al., *Factors affecting short-term and long-term stabilities of proteins.* Advanced Drug Delivery Reviews, 1993. **10**(1): p. 1-28.

215. Pearlman, R.S., S.H. Yalkowsky, and S. Banerjee, *Water Solubilities of Polynuclear Aromatic and Heteroaromatic Compounds.* Journal of Physical and Chemical Reference Data, 1984. **13**(2): p. 555-562.

216. Lad, M.D., et al., *The adsorbed conformation of globular proteins at the air/water interface.* Phys Chem Chem Phys, 2006. **8**(18): p. 2179-86.